Photodissociation Dynamics of Ultracold Strontium Dimers

Master's Thesis

Florian Apfelbeck

München 2015

Photodissociation Dynamics of Ultracold Strontium Dimers

Photodissoziations-Dynamiken von ultrakalten Strontium Dimeren

Master's Thesis
at the Faculty of Physics
of the Ludwig–Maximilians–University
Munich

submitted by
Florian Apfelbeck
Munich, August 05, 2015

COLUMBIA UNIVERSITY
IN THE CITY OF NEW YORK

Primary Advisor:
Prof. Dr. Tanya Zelevinsky
Columbia University in the City of New York

Secondary Advisor:
Prof. Dr. Theodor W. Hänsch
Ludwig-Maximilians-Universität München

Abstract

While photodissociation (PD) is a common technique in AMO and chemical physics used to study the structure of atoms and molecules and their interactions, it is quite novel in ultracold systems. This thesis discusses the PD dynamics of the dimer $^{88}Sr_2$, starting from an ultracold sample of molecules trapped in an optical lattice. We show that PD of ultracold molecules works well and that applying PD in combination with a lattice is possible. Employing these tools results in high control over the quantum states involved and provides high resolution at lower dissociation energies than achievable in conventional PD experiments. We perform 1- and 2-photon PD in the Lamb-Dicke and resolved sideband regime, which enable Doppler- and recoil free measurements. First, we describe a way to determine the lattice trap depth. Furthermore, we prove that we are able to probe the potential barrier of the $(1)1_u$ potential of the $^1S_0$-$^3P_1$ manifold and similar barrier height physics. We then also conduct M1 and E2 1-photon PD transitions without the usually dominating E1 transitions in a controlled way and examine the dynamics of the dissociation products. It is demonstrated, that investigations of the unbound energy states of the higher excited $^3P_1$-$^3P_1$ manifold with 2-photon PD are possible, but very complicated. Additionally, we provide a proof-of-concept of 2-photon PD to this manifold, where we control the initial magnetic sublevel populations. In the course of this work, the existing experimental system was enhanced with a second camera setup. Besides imaging perpendicular to the lattice axis, this enables a new perspective on-axis with the lattice. Thus, the photodissociation fragments and their dynamics can be studied in a similar manner as in other PD experiments. For reconstruction of the initial 3-dimensional angular distribution of the dissociation products from the 2-dimensional camera images, an algorithm called pBasex is used, which is based on Abel-transformation. Data processing and improvement of the signal is achieved through averaging and background subtraction. We perform this off-line, employing several Matlab progamms developed for this work. This thesis is supposed to be a basis for further experiments on PD dynamics of ultracold diatomic molecules in general and PD using an optical lattice in particular.

Contents

Chapter 1

Introduction

1.1 Introduction

Atomic-, molecular- and optical or AMO physics is the research on the structure of atoms and molecules and their interaction with other atoms, molecules or electromagnetic radiation, usually in the form of light. Since its beginnings in the early 20th century[1], it has played an important role in physics and almost inseparably linked to quantum mechanics. Starting as fundamental research with only limited practical applications, many important modern technologies like spectroscopy and lasers have emerged from AMO physics over the years. AMO physics also offers the possibility to experimentally encourage or verify theoretical work in quantum mechanics. AMO physics' main focus continues to be fundamental science with the goal to increase our knowledge. Nevertheless, it additionally has the potential to introduce very important future applications and technologies or to inspire new research, as the past has shown. Current fields of development include quantum communication and computing as the next step in information technology, determination of fundamental constants and the precise measurement of time.

A commonly applied technique in AMO physics is laser cooling, which is used to cool down atoms or molecules to cold and ultracold temperatures. This enables precision experiments and quantum mechanical properties become measurable. Now the question is, why do the particles have to be cold? And what do "cold" and "ultracold" actually mean here? The term "temperature" is closely related to the motion of atoms and molecules, which comprise matter. These particles move about in a random pattern. The more they move, the higher the temperature of the matter and vice versa. We are aiming to cool down atoms and molecules, because strong movement makes precision

[1] Note that optics in general is much older and that modern AMO physics is a relatively new field

measurements very hard or impossible. Here is why: Measurements are performed through interaction of the atoms and molecules with light, which can here be imagined as an electromagnetic wave of a certain frequency. The atoms and molecules react to the light at particular frequencies, depending on their structure, called resonant frequencies. The more precise we can measure this resonant frequency, the more precise we can determine the structure. As the particles move, they also become resonant at lower and higher frequencies and the resonant frequency blurs out. This happens due to the so called "Doppler effect", which is the same effect that causes an ambulance siren to pitch higher when traveling toward you and lower when traveling away. Here, the particles absorb light at lower frequencies when moving toward the light and higher frequencies when moving in the light's direction. Once we cool down the particles to very low temperatures, their motion is strongly reduced. This minimizes the blurring of the resonant frequency and high precision measurements become possible. The temperatures we can reach in our experiment are about 2μK, which is 150 million times colder than room temperature. We achieve that by first using a combination of light and magnetic fields to trap the particles (in a so-called magneto-optical trap) and then hold the molecules in an 1-dimensional optical lattice, another trap constructed with light. The molecules interact with the electric field of the lattice's light such that their movement is confined in one direction. They become trapped in the potential of the field. This makes measurements without the limitations of the Doppler effect possible.

Ultracold atoms and molecules provide access to a broad field of research (an overview can be found, for example, in [1]), one of which the precise measurement of time. One of the main goals of our experimental setup is to built a very precise molecular clock using $^{88}Sr_2$. Today, atomic clocks make technologies like the Global Positioning System (GPS) and the synchronization of cell phone and internet connections possible. The ability to measure the frequencies of atomic and molecular resonances has become so precise that the international definition of the second is now given by the time it takes for a 133-cesium atom to oscillate exactly 9,192,631,770 times between two hyperfine ground states. A molecular clock based on Sr offers an even higher precision to measure time and makes the strontium lattice clock the most precise clock in existence today. It maintains a relative precision of one second over age of the universe (i.e. about 15 billion years).

The primary goals of this thesis are to examine the photodissociation (PD) dynamics of $^{88}Sr_2$ molecules and a general investigation of the possibilities of PD using an optical lattice. PD is the process, by which a molecule is broken up into its constituents by a laser pulse. The dynamics of the fragments flying apart tell us about the structure of the molecule. Investigating the dynamics of PD is a well established method in AMO

physics research [2], for example in velocity map imaging (VMI) [3–5] and photodissociation spectroscopy [6–9]. These techniques are often used for investigation of gas-phase processes in molecular beams. With these experimental systems, however, the initial molecular state can not be controlled and the molecules are not cold. Having an ultracold sample of a bound molecular state and using an optical lattice offers the ability to control all quantum mechanical degrees of freedom of the initial state and, furthermore, results in high precision with an enhanced resolution especially at low frequencies just a few MHz above the binding threshold of the molecules. Such low frequencies are difficult to approach in conventional PD experiments. Additionally, we are able to see and examine different potentials of excited state manifolds. PD in combination with traps and even with optical lattice traps have been part of other experiments before [10, 11], however, PD was only used to enable detection of the molecules in these cases.

In this thesis, experiments on the dynamics of PD will be discussed, some of which exploit the advantages of this technique. These experiments can be considered as a proof-of-concept of PD using an optical lattice and as a first step towards precise investigations of the continuum above the threshold of excited molecular states. Furthermore, future possibilities of PD with this experimental setup and of PD using a lattice in general will be sketched.

1.2 Overview

In Chap. 2, a background on $^{88}Sr_2$ and the structure of its constituent ^{88}Sr is provided. An overview of the most important processes and tools the experiments in this thesis are based on, like Zeeman cooling, a magneto-optical trap (MOT), an optical lattice and the enhancement of the setup with a second camera in order to investigate the angular distribution is given in Chap. 3. Chaps. 4, 5 and 6 represent the main part of this thesis, containing the results. In Chap. 4, a discussion about the dynamics of PD when a lattice is present will be initiated, since using a lattice is a relatively new way to photodissociate and there has not been much investigation on it yet. We conducted two 1-photon and two 2-photon dissociation experiments which are described in Chap. 5 and Chap. 6. Each of the two chapters will first provide an overview of theory, followed up by a presentation and discussion of the results. In Chap. 7, the data processing to improve the signal-to-noise ratio and the suppression of diffraction patterns in the images taken is elaborated. Besides the installation of the additional beam setup and the second camera, the establishment of the data processing was a major part of this thesis's work. App. A contains the code of the four Matlab programs used for analysis.

Chapter 2

Background on ^{88}Sr & $^{88}Sr_2$

This chapter provides a basic understanding of the ^{88}Sr atom and the $^{88}Sr_2$ molecule, which helps to comprehend the descriptions of the experiments and the results presented. First, the atomic structure of ^{88}Sr is introduced, followed by the description of the structure of the $^{88}Sr_2$ molecule, both with focus on the relevant features for this work. After PD, the atoms can be described as a molecule with very large internuclear distance. In this case, the atoms are in a state in the continuum above the dissociation threshold, in the following also called asymptote, of the excited molecular state. The notation used throughout this thesis is elaborated in Sec. 2.3. Additionally, we motivate the measurement of the potential barrier height of the so called $(1)1_u$ potential described in Chap. 5 with a calculation of the expected value of this barrier height. Eventually, the selection rules necessary to explain the processes in the experiments are presented.

2.1 Atomic Structure of ^{88}Sr

The experimental system takes advantage of the atomic structure of ^{88}Sr to slow down the atoms via Zeeman slowing, trapping them into two consecutively applied magneto-optical traps (MOT) and eventually photoassociate (PA) them into $^{88}Sr_2$. ^{88}Sr is an alkaline earth metal and thus has two valence electrons. Only the low lying S, P and D orbitals of the atom are relevant for this experiment. They are illustrated in Fig. 2.1 together with the important transitions. The energy levels are noted for the common term notation of atoms $^{2S+1}L_J$, where S is the spin quantum number, L is the orbital quantum number and J is the total angular momentum quantum number [12].

The atom can either be in a singlet or triplet state which means that the spin is $S = 0$ or $S = 1$, respectively. Generally, dipole transitions must be between $\Delta S = 0$ pair

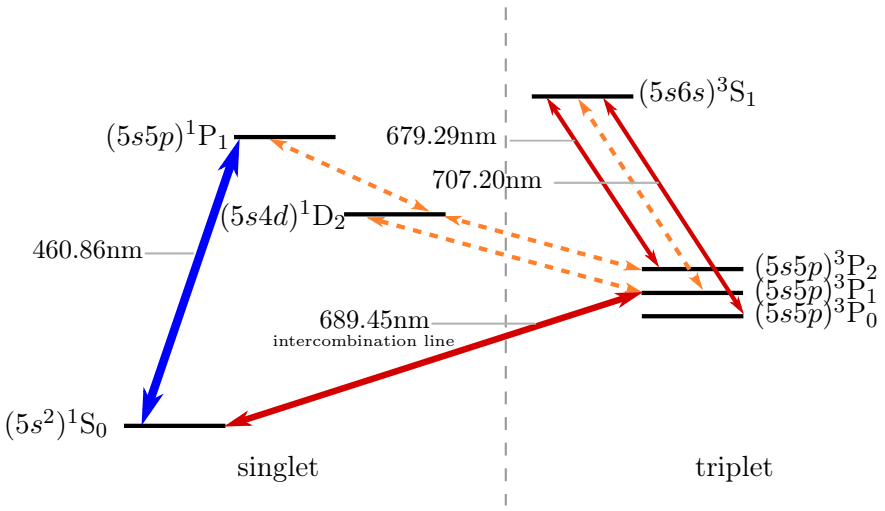

Figure 2.1: The important transitions for cooling and trapping ^{88}Sr atoms. The blue transition with a wavelength of 460.86 nm (nat. linewidth $\Gamma/(2\pi) = 32$ kHz is used for slowing, imaging and for the first magneto-optical trap (MOT). The red intercombination line with a wavelength of 689.45 nm (nat. linewidth $\Gamma/(2\pi) = 7.5$ kHz) is used for the second MOT, PA and probing. The re-pump scheme with the two red lasers allows a longer lifetime of the first MOT. The yellow dotted lines represent decay.

of states. The spin symmetry breaks when the spin couples to the orbital angular momentum L (LS-coupling) and so called intercombination transitions between singlet and triplet states become weakly allowed. This enables a narrow transition $^1S_0 \leftrightarrow {}^3P_1$ (natural linewidth $\Gamma/(2\pi) = 7.5$ kHz) which is used for the second (red) MOT and PA (large red arrow).

The strong dipole transition $^1S_0 \leftrightarrow {}^1P_1$ with a linewidth of $\Gamma/(2\pi) = 32$ MHz is used for the initial Zeeman slowing of the atoms, the first (blue) MOT and the imaging of the atoms (blue arrow). From the $^1P_1$ state, the atoms mostly decay back to the$^1S_0$ state which enables a cycling transition for slowing and cooling. A small fraction with a branching ratio of about 10^{-5} decays to the $^1D_2$ state. From there, the dipole transition to the $^1S_0$ ground state is not allowed by the selection rule $\Delta L = 0, \pm 1$ and the atoms decay to the $^3P_1$ and $^3P_2$ triplet states. here, it is not immediately accessible for the initial cooling transition anymore. This limits the effectiveness and lifetime of the blue MOT and a re-pump into the cycle is desirable. In order to keep the population of the $^3P_2$ state in the circle, it is possible to pump the atoms back to the $^3S_1$ from where they decay to the $^3P_1$ state. Then, using a transition close to the intercombination line, the atoms can be brought back into the circle. The $^3S_1$ state also decays to $^3P_0$ with a large branching ratio, hence additional pumping back into the $^3S_1$ state using a wavelength of 679.29 nm is necessary. Using this re-pumping scheme, the cycle is practically closed and large blue MOT life times can be expected [13]. The terms Zeeman slowing, blue and red MOT, PA and imaging are further explained in Chap. 3.

2.2 Molecular Structure of $^{88}Sr_2$

The basic structure of molecules can be explained with three different degrees of freedom; the electronic, rotational and vibrational ones. First, we introduce an overview of the important quantum numbers and their correlation for understanding the structure of diatomic molecules:

Electronic spin:	$\mathbf{S}$
Orbital angular momentum of the electrons:	$\mathbf{L}$
Total atomic angular momentum:	$\mathbf{J}_a$=$\mathbf{S}$+$\mathbf{L}$
Total angular momentum:	$\mathbf{J}$
Projection of total angular momentum on z-axis:	m
Vibrational index:	v
Rotational momentum of the nuclear structure:	$\mathbf{R}$=$\mathbf{N}$−$\mathbf{L}$
Total angular momentum without electronic spin:	$\mathbf{N}$=$\mathbf{J}$−$\mathbf{S}$

Electronic Levels

The notation of the electronic states of molecules is based on Hund's cases. This is a framework named after the spectroscopist F. Hund (1896-1997), describing molecules using five different coupling cases of rotational to electronic motion, alphabetically indicated from (a) to (e). The cases never represent a perfect accounting of the molecular structure, but depending on the molecule, some provide a good approximation. In particular, $^{88}Sr_2$ molecules are best described by the cases (a) and (c). This is because the coupling between S and L depends on the bond length R as a potential (given in [14]). In case we are talking about very weakly bound dimers with states only little below the dissociation threshold, we will mostly use case (c). This is what one would expect since analogous free atoms have strong L and S coupling. Further information about the notation of molecules can be found in [12, 15, 16]. Please also notice that ^{88}Sr has no nuclear spin.

Hund's case (a) The dependencies of Hund's case (a) are shown in the schematic in Fig. 2.2. It is used when the electronic orbital momentum $\mathbf{L}$ and the spin $\mathbf{S}$ are both strongly coupled to the internuclear axis and it is $\Omega = \Lambda + \Sigma$. $\mathbf{R}$, the rotational momentum of the nuclear frame, couples with Ω to the total angular momentum $\mathbf{J}$. For this case the good quantum numbers, i.e. the quantum numbers that are well defined and describe eigenstates, are Λ, Σ, Ω, $\mathbf{S}$ and $\mathbf{J}$. Additionally, a prefix is used to indicate the electronic energy level. The ground state is indicated with X, whereas for higher states upper case letters A, B, C, D, ... and lower case letters a, b, c, d, ... are used,

depending whether the excited state has the same or different multiplicity than the ground state. In order to illustrate the complexity of $^{88}Sr_2$ and to give examples of the notation, the potentials with Hund's case (a) and (c) are shown in Fig. 2.3.

The notation in Hund's case (a) has similarities with the notation for atoms. Whereas for atoms the term symbol $^{2S+1}L_J$ is applied, the most commonly used molecular term symbol, following [17], is

$$^{2S+1}|\Lambda|^{\pm}_{\Omega,(g/u)}. \tag{2.1}$$

Here S is the electronic spin, $2S+1$ the multiplicity of the state, Λ is the projection on the internuclear axis of the total electronic angular momentum $\mathbf{L}$ and Ω the projection of the total angular momentum $\mathbf{J}$. Since $\mathbf{S}$ and $\mathbf{L}$ have two possible directions of precession about the internuclear axis, their projections are $\pm\Lambda$ and $\pm\Sigma$. Hence, Ω has two magnitudes, which are represented in the term symbol as $+$ or $-$.

The subscript g/u is only used for homonuclear dimers like Sr_2 and indicates the symmetry notation, i.e., whether the molecule is symmetrical about the inversion center and the wave function does not change sign (g for even) or change sign (u for odd). To preserve the parallels to notation of the atomic structure, it is $\Lambda = \Sigma, \Pi, \Delta, \Phi, ...$, while for atoms it was $L = S, P, D, F, ...$

Hund's case (c) Hund's case (c), illustrates in Fig. 2.4, is applied when the spin $\mathbf{S}$ and the orbital angular momentum of the electrons $\mathbf{L}$ are strongly coupled and no coupling to the internuclear axis exists. $\mathbf{S}$ and $\mathbf{L}$ add vectorially to $\mathbf{J}_a$. Ω, the projection of $\mathbf{J}_a$, then couples with the rotational momentum of the nuclear structure to form $\mathbf{J}$. Hence, Ω, $\mathbf{J}$ and $\mathbf{J}_a$ are conserved and called good quantum numbers. A different notation than for Hund's case (a) is used here:

$$(n)|\Omega|^{\pm}_{(g/u)} \tag{2.2}$$

$\pm$ and g/u indicate the two magnitudes of Ω and the symmetry notation as described before, whereas (n) indicates the energy ordering with increasing numbers to differentiate states which have the same term symbol. In other words, (n) here plays the role of A, B, C, D, ... for case (a).

Since the ground state of ^{88}Sr has no electronic spin, cases (a) and (c) are equivalent. Because it is more common, we choose the notation $X\Sigma$ as in Hund's case (a). Examples for Hund's case (c) are presented on the right side of Fig. 2.3. One can see the difference between the two cases. Both describe the potentials, but sometimes one or the other

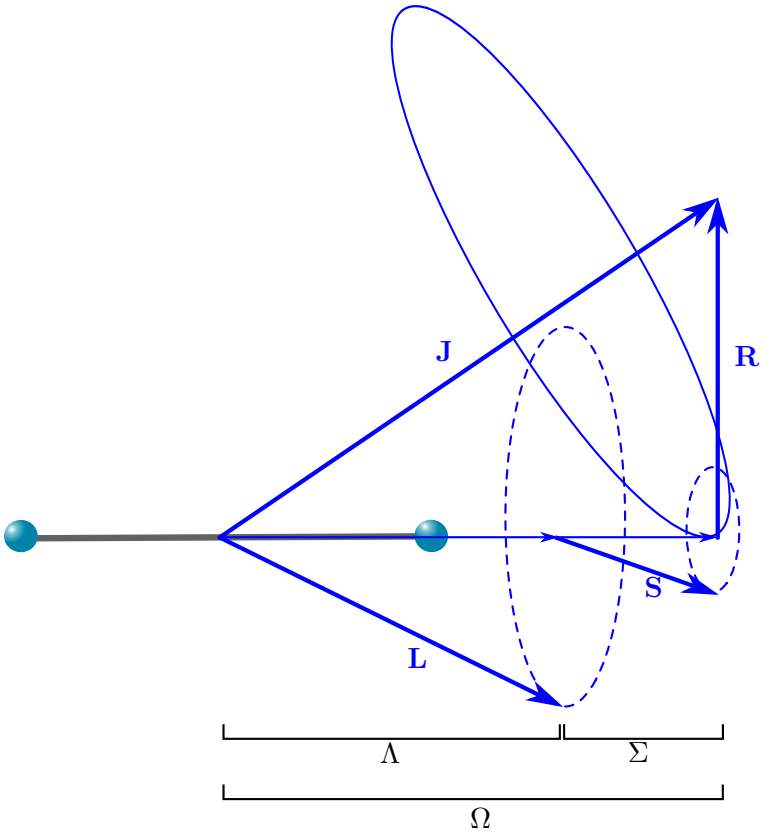

Figure 2.2: Hund's case (a). The orbital angular momentum of the electrons **L** and their spin **S** couple both strongly to the internuclear axis. Their projections on the internuclear axis Λ and Σ yield Ω, which couples with the rotational momentum of the nuclear frame **R** to the total angular momentum **J**.

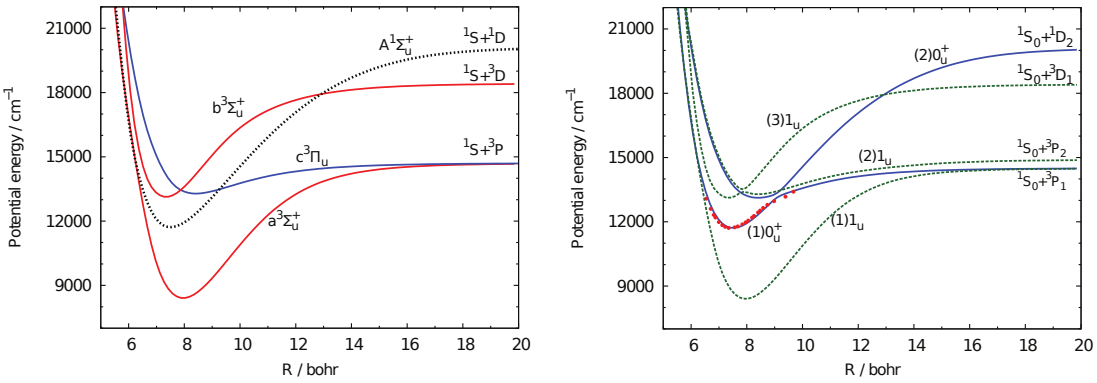

Figure 2.3: Left side: Potentials of $^{88}Sr_2$ applying Hund's case (a). Right side: Potentials applying Hund's case (c) [18].

works better for a certain purpose because the degree of mixing of **L** and **S** varies between different rovibrational states. In this thesis usually Hund's case (c) is the better fitting description.

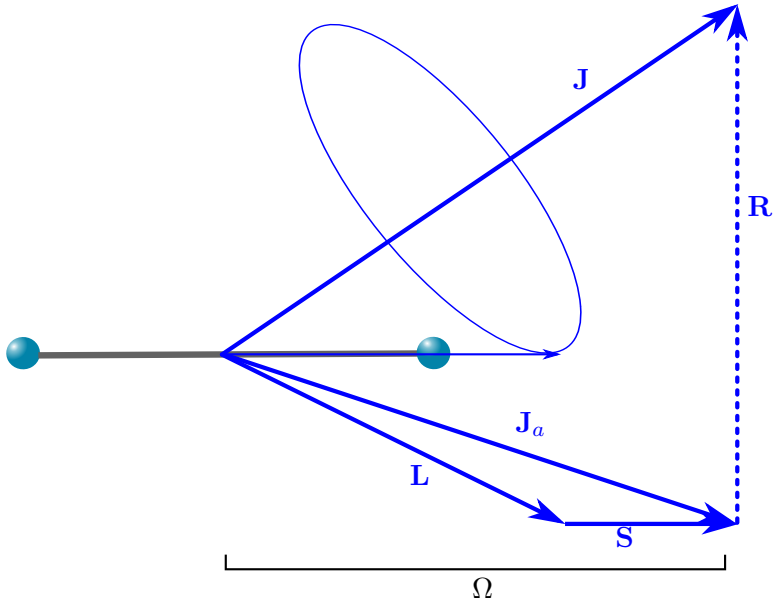

Figure 2.4: Hund's case (c). **L** and **S** couple strongly and yield the total atomic angular momentum $\mathbf{J}_a$. The projection of $\mathbf{J}_a$, namely Ω, couples with the rotational momentum of the nuclear structure **R** to the total angular momentum **J**.

Vibrational & Rotational Levels

Another important quantum number defining a state of a molecule is the vibrational state v. It describes the motion of the nuclei along the axis of the molecule, thus the vibration in this axis. Every potential described above using Hund's cases has various quantized vibrational states, starting with $v = 0$ as the most deeply bound state and counting up. When working with weakly bound states close to being unbound it is convenient to count v down from the least bound state, i.e. $v = -1, -2, -3, ...$ The state of a molecule also has the total angular momentum **J** as a rotational quantum number. When we count down, we assign v for a particular J, so that v is the same for states with the same vibrational wavefunction. For example, v of one state with J=3 is $v = -2$ and is the least bound state, since its J=1 version has one bound v state above that. To fully specify a molecule it is necessary to provide more information than the Hund's term notation but also include these quantum numbers. We choose to do so by adding them in parenthesis after the term notation, thus $(v = ..., J = ...)$ for a ground state, $(v' = ..., J' = ...)$ for the first excited state and so on. To keep it simple, "$v =$" and "$J =$" are not noted, so for the ground state with $J = 2$ we write $X(-1, 2)$ instead

of $X(v = -1, J = 2)$, or for the first excited state with $v' = -1$ and $J' = 1$ we write $(1)1_u(-1, 1)$ instead of $(1)1_u(v' = -1, J' = 1)$.

Additionally, it is sometimes necessary to state the different magnetic sublevels coming from the projection of the angular momentum on the z-axis. This becomes important, when a magnetic field is applied and Zeeman splitting occurs. Hence, m is added to the notation, so it is $(v = ..., J = ..., m = ...)$ as for example $X(-1, 2, 0)$, $X(-1, 2, -1)$ or $(1)1_u(-1, 1, 1)$

2.3 Notation of Continuum States

In most of the experiments described in this thesis, $^{88}Sr_2$ molecules were dissociated with photons to ^{88}Sr atoms, called photodissociation (PD). A laser breaks the internuclear bond between the two atoms of the molecule when exciting them from one to another potential and when the energy of the laser is as high or higher than the binding energy. The additional energy causes the atoms to fly apart. One can imagine this also as an exploding molecule. The dissociated, unbound atoms can be treated as a molecule with a large internuclear distance as it is shown in Fig. 2.5. The frequency of the dissociating laser is directly related to the energy via Plank's constant with $E = hf$. Hence, by tuning the laser to higher frequencies, the additional energy not needed to excite the atoms from one to the other potential and to break the bond receive the atoms as kinetic energy. The potentials of the molecule converge against an asymptote for large internuclear distances and if the potentials are in the same manifold they have the same asymptote. This is depicted in Fig. 2.6, which illustrates the potentials important for this thesis.

The manifold of the $^1S_0$-$^3P_1$ asymptote is split up in two in this scheme for better illustration of the difference between the u and g potentials. After PD, when the atoms are not bound anymore they are in a state in the continuum above that asymptote. The continuum states are labeled based on the common atomic notation. Every manifold and the corresponding asymptote is named after the state of the atoms. For example, the ground state asymptote is named $^1S_0$-$^1S_0$, as the equivalent at a large distance are two ground state atoms, whereas the asymptote for the first excited state is named $^1S_0$-$^3P_1$. Therefore, one of the atoms is in the ground state and one in the $^3P_1$ excited state. Additionally, some of the sates have potential barriers like the $(1)1_u$ potential of the $^1S_0$-$^3P_1$ manifold. In order to dissociate molecules to unbound states in this potential, the barrier has to be overcome. The barrier height is estimated in the following section and a way to measure it is presented in Chap. 5. In the course of this thesis the continuum of states above the asymptote will also sometimes be called "shelf". This

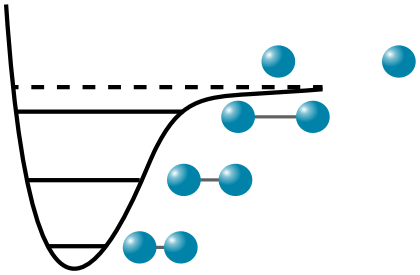

Figure 2.5: The deeper bound the molecules, the smaller is the distance between the nuclei. Two unbound atoms can be treated as two nuclei of a molecule with very large distance. This happens when an electric field excites the molecule to another energy level and further causes the nuclei to overcome the binding energy. When the field is applied using a laser, one speaks of photodissociation (PD).

is due to its shape when taking the trace with increasing the laser frequency. The line shape of this shelf will be further explained in Chap. 4.

2.4 Calculation of Barrier Height of $(1)1_u$ Potential of $^1S_0$-$^3P_1$ Manifold

It is possible to calculate the height of the potential barrier from the bound to the unbound states of the repulsive $(1)1_u$ potential. There are several ways to calculate this barrier height. We follow [19], where the two long range $(1)1_u$ and $(1)0_u^+$potentials are approximated as

$$V_{1_u} = -\frac{C_{6,1_u}}{R^6} + \frac{C_3}{R^3} + \frac{h^2 A_{1_u}}{8\pi^2 \mu R^2} \tag{2.3}$$

and

$$V_{0_u} = -\frac{C_{6,0_u}}{R^6} - 2\frac{C_3}{R^3} + \frac{h^2 A_{0_u}}{8\pi^2 \mu R^2}. \tag{2.4}$$

Here, R is the internuclear distance, the term containing C_6 describes a van-der Waals interaction, the one containing C_3 is a resonant dipole term and the one containing $A_{1_u} = J'(J'+1)$ or $A_{0_u} = J'(J'+1) + 2$ stands for the contribution of the rotation to the potential. For a first estimate, we drop the last term which has only a small contribution to the overall potential. After deriving and solving for R, it is

$$R_{1_u} = \sqrt[3]{\frac{2C_{6,1_u}}{C_3}} \tag{2.5}$$

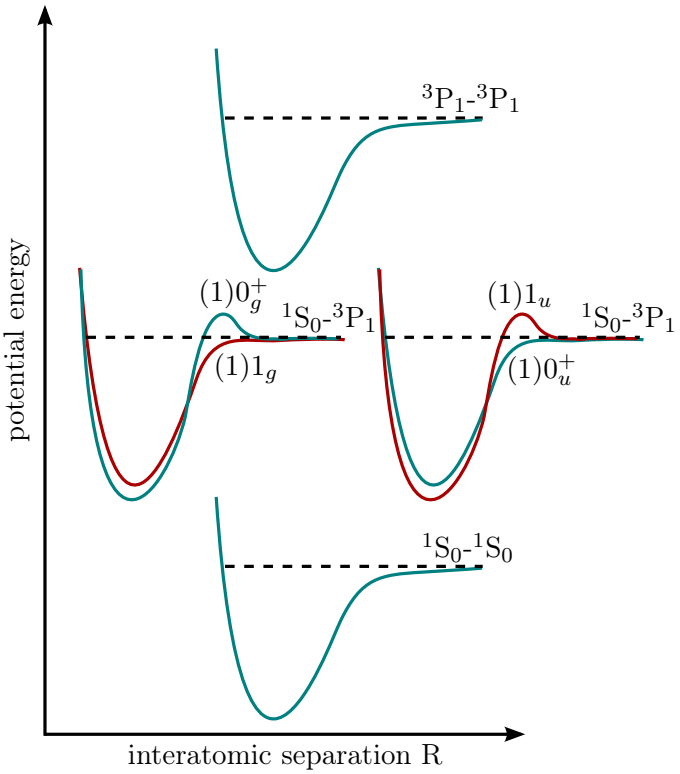

Figure 2.6: The $^{88}Sr_2$ potentials important for this thesis with their corresponding asymptotes. The potentials of the $^1S_0$-$^3P_1$ manifold exchange shape depending on u and g and are illustrated here separately for better understanding. Note that the doubly excited $^3P_1$-$^3P_1$ manifold has a lot of complexity and is illustrated simplified here and in the course of this thesis.

and

$$R_{0_u} = \sqrt[3]{-\frac{C_{6,0_u}}{C_3}} \tag{2.6}$$

Since the values for $C_{6,1_u} = 4085(50)\ E_h a_0^6$, $C_{6,0_u} = 3868(50)\ E_h a_0^6$ [20] and $C_3 = 0.0075(1)\ E_h a_0^3$ with $E_h = 4.36 \cdot 10^{-18}$J and $a_0 = 0.0529$ nm [19] are always positive, we only receive real values for R for the $(1)1_u$ potential. Hence, it is not possible to calculate a potential barrier of the 0_u^+ potential like this. When plugging in C_6 and C_3 into Eq. 2.5 we receive $R = 102.9(9)\ a_0$. With the first two terms of Eq. 2.3, this yields a $(1)1_u$ potential energy of $E_B = 3.4(5) \cdot 10^{-9} E_h = 1.51(22) \cdot 10^{-26}$J which means a barrier height of $\epsilon_B = 22.8(3.5)$ MHz. When calculating the potential height numerically with Mathematica, including all three terms of Eq. 2.3 and assuming J'= 1 we receive a radius of $R = 101.9(9)\ a_0$ and a potential height of $\epsilon_B = 22.6(3.4)$ MHz. In Chap. 5, a preliminary measurement of the barrier height of the $(1)1_u$ potential is presented. A disagreement of this calculated value and the experimentally obtained value is present and will be explained there.

2.5 Selection Rules

Selection rules define the possible transitions from initial state to final state. In Tab. 2.1 an overview of the important selection rules for this thesis is provided. One has to distinguish between electric dipole transitions (E1) which are first order transitions and higher order transitions. The most often occuring higher order transitions are the two second order magnetic dipole (M1) and electric quadrupole (E2) transitions. They are usually 10^5 times weaker than E1 transitions. Thus, it is normally difficult to obtain a signal from them. However, by choosing a measurement, where E1 transitions are forbidden by selection rules but M1 and E2 transitions can occur we can investigate them (we neglect higher order transitions here, since they are even much weaker). An example is a $g \to g$ transition. Such a measurement will be presented in Chap. 5. E1 and M1 transitions are well known and a detailed discussion can be found in various textbooks like [12, 15, 21], while E2 transitions are treated in [21].

An overview stating if π- and σ-transitions occur is given in Tab. 2.2. This table solely applies, when the quantization axis is defined by the applied magnetic field. This is, when there is a strong magnetic field which is usually the case in the experiments described here. Its direction was vertical here. The probe laser is linearly polarized and is propagating perpendicularly to the quantization axis and a traveling wave. When the polarization of the probe laser is parallel to the magnetic field, E1 π- and M1

σ-transitions are driven, when it is perpendicular E1 σ- and M1 π-transitions occur. Skewed angles result in a mixture of π and σ for the various transitions. The change of the magnetic sublevel due to π- and σ-transitions are $\Delta m = 0$ and $\Delta m = \pm 1$, respectively. For other settings, like little or no applied magnetic field, the lattice or probe beam polarization can dominate and define the quantization axis. Then the transitions between the magnetic sublevels differ. This is not the case for ground state molecules though, since they are not sensitive to the field. Further discussion about magnetically enabled transitions in $^{88}Sr_2$ can be found in [22]. π- and σ-transitions are not very well defined for E2. One just can say that it is $\Delta m = \pm 1$, if the polarization of the probe laser is parallel to the magnetic field and $\Delta m = \pm 2$, if it is perpendicular. $\Delta m = \pm 2$ occurs because the light propagation direction, laser polarization and the quantization axis are mutually orthogonal [21]. In this thesis, we normally applied a vertical magnetic field (of about 2 Gauss) when it was important to make sure that the transitions stated in Tab. 2.2 apply. For the measurements of the lattice trap depth in Chap. 4, the vertical magnetic field was zero to exclude quadratic Zeeman shifts.

Quantum number	Electric dipole (E1)	Magnetic dipole (M1)	Electric quadrupole (E2)
Parity	$g \rightarrow u$ $g \not\rightarrow g$	$g \rightarrow g$ $g \not\rightarrow u$	
Angular momentum	$\Delta J = 0, \pm 1$ $(0 \not\rightarrow 0)$		$\Delta J = 0, \pm 1, \pm 2$ $(0 \not\rightarrow 0, 1)$
Principal quantum number n	-	$\Delta n = 0$	-
Magnetic sublevel	$\Delta m = 0, \pm 1$		$\Delta m = 0, \pm 1, \pm 2$

Table 2.1: An overview of the important selection rules for this thesis [21].

Probe beam polarization vs. applied magnetic field	Electric dipole (E1)	Magnetic dipole (M1)
Parallel	π	σ
Perpendicular	σ	π

Table 2.2: This table is valid, when the applied magnetic field defines the quantization axis. Transitions with $\Delta m = 0$ are π-transitions, $\Delta m = \pm 1$ are σ-transitions. π- and σ-transitions are not very well defined for E2.

Chapter 3

Apparatus

The apparatus of the Sr_2 experiment is well described in Chris Osborn's thesis [23] and just a brief overview us provided here. Only the additional camera setup is described in more detail.

3.1 Overview of Experimental Setup

The construction of the experiment started in 2009 and the first creation of a magneto-optical trap (MOT) was realized in 2010. Since then, the setup has been continuously extended and improved. As part of this thesis, the latest enhancement, a second camera which allows an additional perspective on the molecules, was installed. This enables a new way to study PD with this experimental system.

Atom Source and Zeeman slower

A schematic side view of the experimental setup is shown in Fig. 3.1. First, a solid Sr sample is heated up inside an oven to about 600°C (1). Vapor pressure builds up and the Sr atoms is ejected using a nozzle with microtubes which collimate the beam. A beam shutter (2) enables control about the loading times of atoms into the experimental chamber (6). Since the thermal velocity of the atoms is about 450 m/s when ejected from the oven, the beam has to be slowed down in the ∼1 meter long tube (3) connecting the oven with the chamber. For this we use a permanent magnet Zeeman slower described in [24]. The Zeeman slower uses the $^1S_0 \leftrightarrow ^1P_1$ transition, accessed by a blue laser with a wavelength of about 461 nm. This wavelength is achieved with a setup containing a 922 nm extended cavity diode laser (ECDL) in the Littman configuration [25], an tapered amplifier [26] to receive higher laser power and

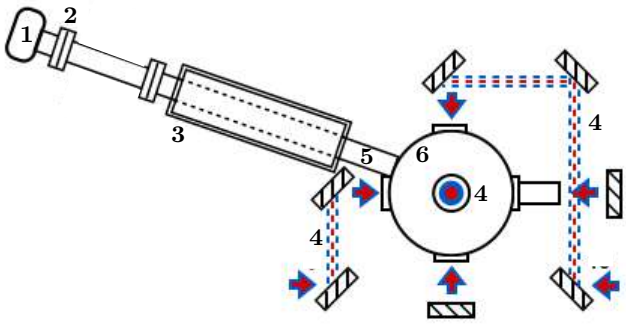

Figure 3.1: Schematic view of the experimental setup with (1) ^{88}Sr oven, (2) shutter to control loading into the chamber, (3) Zeeman slower, (4) blue and red MOT beams, (5) atomic beam tube towards (6) chamber. Scheme from [23] and edited.

a frequency doubling cavity which changes the wavelength from 922 nm to 461 nm. The cavity in the bow-tie setup is based on second harmonic generation in a non-linear crystal. Further information about the 461nm light source and bow-tie cavities can be found in [23, 27, 28]. The laser is locked to the $^1S_0 \leftrightarrow {}^1P_1$ transition by saturated absorption locking using a galvatron vapor gas cell (described in [29–31]) and a piezo at one of the cavity mirrors as feedback. For the experiments described here, we were able to send a 461 nm laser beam with powers between 130 mW− 170 mW towards the experiment. This beam is then divided among the blue MOT and imaging setups as well as the Zeeman-slower. Once the atoms are slowed down and reach the chamber, they are trapped in a MOT.

Magneto-Optical Traps

A magneto-optical trap (MOT) is a tool commonly used in AMO physics to cool and trap neutral atoms. In our experiment, two different stages of MOT cooling are applied. The first MOT operating on the 32 MHz $^1S_0 \leftrightarrow {}^1P_1$ line cools the atomic sample down to a few mK. The atoms subsequently are transferred to a red MOT operating on the 7.5 MHz $^1S_0 \leftrightarrow {}^3P_1$ line in order to decrease the temperature of the atomic sample down to $\approx 2\mu$K. In a MOT, three circularly polarized perpendicular beams intersect at one point inside the chamber. Each beam is reflected back by a mirror and the polarization direction of the reflection is reversed by a quarter waveplate. This results in a pair of counter polarized and propagating beams.

The working scheme of a MOT in one dimension is illustrated in Fig. 3.2. In addition to the three beams, a quadrupole magnetic field is applied. This leads to Zeeman splitting of the excited atomic energy level with J=1 in this example. The splitting increases with larger distance from the trap center and the restoring force is higher. The laser frequency is slightly detuned from the transition between the J=0 and J=1 state. Due

to the characteristics of the quadrupole magnetic field, the beams are resonant with a σ^+ transition at one side and with a σ^- transition at the other side. The resonant beams cause a restoring force in their propagation direction which is the center of the trap.

The Doppler cooling limit T_D estimates the temperature limit of the possible cooling. It depends on the natural linewidth Γ of the cooling transition and is described by

$$k_B T_D = \frac{1}{2}\hbar\Gamma \tag{3.1}$$

where k_B is the Boltzman constant and $\hbar$ the reduced Planck constant. The $^1S_0 \leftrightarrow {}^1P_1$ transition for the first MOT has a natural linewidth of $\Gamma = 2\pi \cdot 32$ MHz while the intercombination line $^1S_0 \leftrightarrow {}^3P_1$ transition used for the second MOT has a natural linewidth of $\Gamma = 2\pi \cdot 7.5$ KHz [32]. This results in Doppler-limits of about $T_{D,blue} = 770$ μK and $T_{D,red} = 180$ nK. With the current setup, we can reach temperatures in the red MOT of approximately 2 μK. We could achieve colder temperatures, if decreased the power of the lasers, but this would lead to fewer trapped atoms. There is another important temperature limit, the recoil limit T_r, where the thermal energy is equal to the energy induced by a single photon recoil. For the $^1S_0 \leftrightarrow {}^3P_1$ transition, these limits are almost exactly equal.

The 461 nm light for the blue MOT originates from the previously described frequency doubling setup. To improve the lifetime of this MOT, two repump ECDL lasers with wavelengths of 679 nm and 707 nm drive the $^3P_2 \leftrightarrow {}^3S_1$ and $^3P_0 \leftrightarrow {}^3S_1$ transitions, respectively. The 689 nm light for the red MOT is also generated in an ECDL and locked to a high-finesse Fabry-Perot cavity, applying the technique detailed in [33, 34].

Lattice

Even at the low temperatures of the red MOT, the experienced Doppler shift is larger than the linewidth of the intercombination line [23]. Additionally, when performing spectroscopy one has to deal with the recoil caused by the momentum of the absorbed photon. The first effect broadens the signal and limit the precision while the other causes a slight shift in the resonant frequency. By using a certain optical dipole trap, called lattice, it is possible to do Doppler-free and recoil-free spectroscopy. In our experiments we work with a one dimensional lattice. By reflecting a beam of light with a wavelength of about 914 nm back to its original path and focusing the initial and the reflected beams at the same place in the middle of the chamber, a standing wave is created by interference, whose potential traps the atoms (Fig. 3.4). The potentials

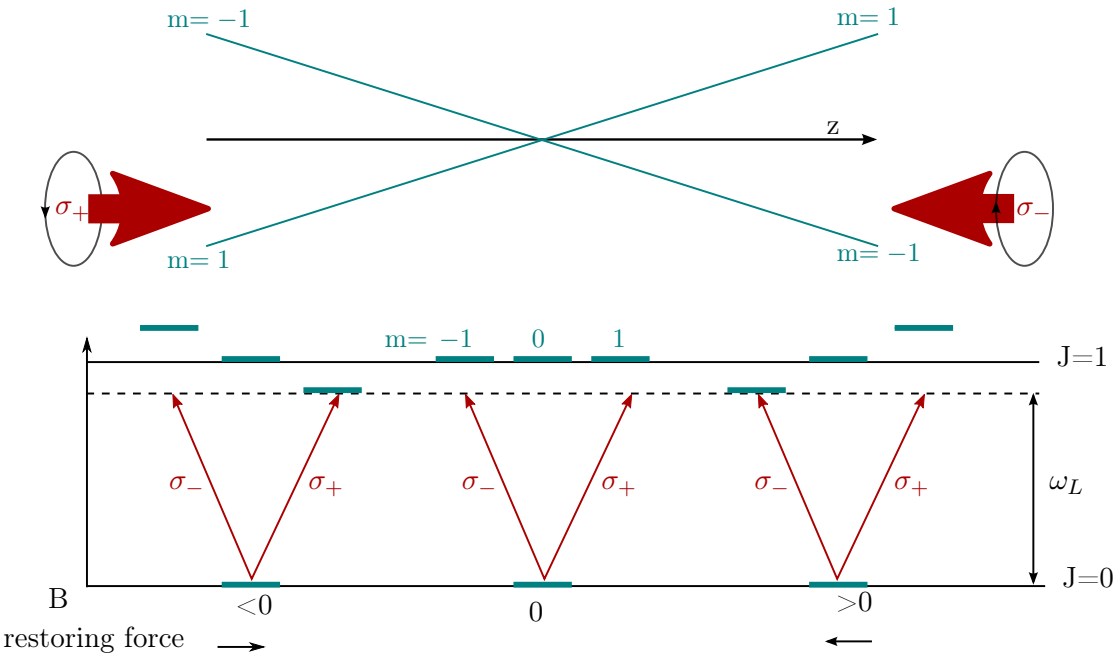

Figure 3.2: Applying a magnetic field in the chamber leads to Zeeman splitting. The magnetic sublevels then have slightly different energies. This effect is stronger with higher magnetic field, which increases with distance z from the trap center. By using two counter-propagating circularly polarized and slightly off resonance laser beams, it is possible to only address the magnetic sublevel causing a restoring force back to the trap center.

of the lattice look like pancakes whereas the whole cloud of trapped atoms cloud has the shape of a cigar. These shapes are illustrated in Fig. 3.3.

For the following, we define a coordinate system, with the x, y-axes perpendicular to the lattice and a z-axis pointing in the direction of the lattice. The time averaged electric field of the two counter-propagating beams on the z-axis can be approximated by

$$\langle |E| \rangle = |E_0|^2 \cos^2(kz) \tag{3.2}$$

where E_0 is the magnitude of the electric field and $k = 2\pi/\lambda$ is the wavenumber. The dipole potential of the standing wave can be written as

$$U = -U_0 \cos^2(kz) \tag{3.3}$$

where U_0 is the time averaged trapping potential. This yields to

$$U = -U_0 \cos^2(kz) \simeq -U_0(1 - (kz)^2) \tag{3.4}$$

after Taylor expansion of (kz) to the second oder. The Hamiltonian of a quantum harmonic oscillator is

$$H = T + U = \frac{p_2}{2m} + \left(U_{min} + \frac{m\omega_{trap}^2 z^2}{2} \right). \tag{3.5}$$

$-U_0$ is the amplitude of the potential of the standing wave, while U_{min} is a potential minimum. Thus, we can say $U_{min} = -U_0$. For the angular trap frequency and the trap frequency we then receive from Eq. 3.4 and Eq. 3.5:

$$\omega_{trap,z} = \sqrt{\frac{2U_0 k^2}{M}} = \sqrt{\frac{8\pi^2 U_0}{M\lambda^2}} \tag{3.6}$$

$$f_{trap,z} = \frac{1}{\lambda}\sqrt{\frac{2U_0}{M}}. \tag{3.7}$$

Note that this is the trap frequency along z, the lattice axis. As it is shown in Fig. 3.4, the difference in frequency between the main carrier and the red and blue detuned sidebands is the trap frequency. Since we are able to resolve the sidebands, it is possible to measure $f_{trap,z}$. This will be useful in Chap. 4 where we want to measure the lattice trap depth U_0.

The trapped atoms are in the so called Lamb-Dicke regime, when the Lamb-Dicke parameter is smaller than 1 ($\eta = \sqrt{\frac{\omega_r}{\omega_{trap,z}}} \ll 1$, where $\omega_r = \hbar k^2/2M$ is the recoil frequency [35]). This regime is reached, when the angular trap frequency is larger than the absorbed photon's recoil frequency $\omega_{trap,z} > \omega_r$ and it is possible to perform recoil-free spectroscopy. The recoil is then absorbed by the lattice photons. The further one is in the Lamb-Dicke regime (the smaller η is) the more recoil gets absorbed by the lattice potential. A more detailed description of the principles of a lattice and the Lamb-Dicke regime can be found in [35, 36].

Probe Beams

With experimental setup we usually apply three probe beams to create (PA), investigate and split (PD) $^{88}Sr_2$ molecules, but if necessary, more beams can be used. All three ECDL lasers are frequency locked to the 689 nm red MOT laser which is locked to a cavity as described above. They are located at a separate table and guided by fibers to the experiment. There, they are combined with the beam path of the lattice in oder to to assure their interaction with the molecules. Every measurement requires a certain

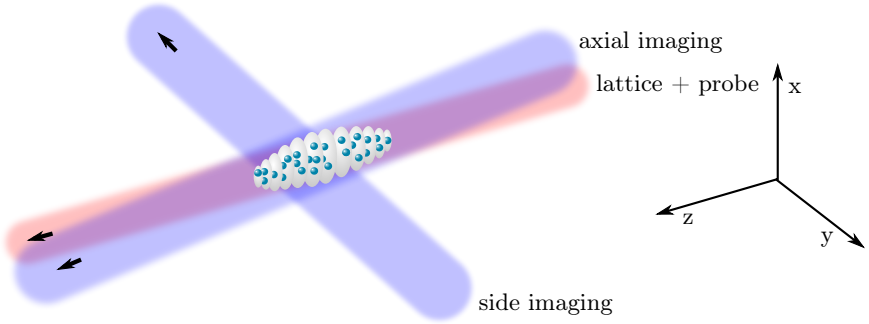

Figure 3.3: Lattice and probe beam have the same beam path, while the axial imaging beam is aligned in a slight angle with respect to the lattice axis. This is due to the chosen approach to guide this beam into the chamber via D-shaped mirrors, further detailed in the text. The side imaging is perpendicular to the lattice. The lattice has the form of a row of "pancakes", while the whole atom cloud has a cigar shape. In each "pancake", the atoms are confined in the z-dimension and have a Gaussian distribution in x and y.

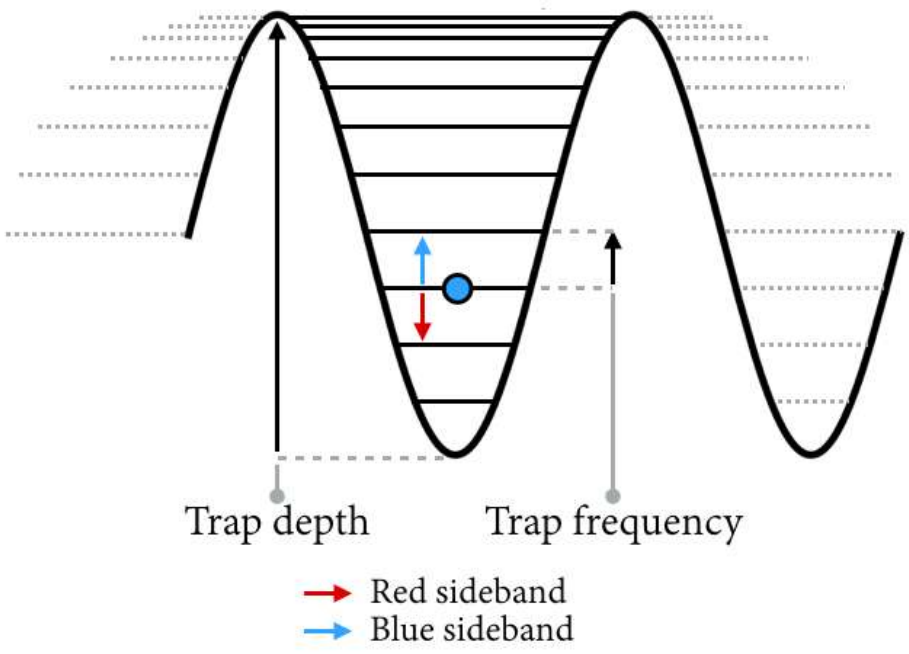

Figure 3.4: Illustration of a 1D optical lattice trap. An atom is confined in one dimension. The distance from the carrier band with the blue dot indicating a particle to the red and blue sidebands is the trap frequency $f_{trap,z}$, which we are able to measure. Scheme from [23].

sequence of these lasers which will be described in the corresponding sections in Chaps. 4, 5 and 6.

Imaging

Before imaging, the molecules are turned back into atoms by a laser pulse. This indirect detection method is chosen over direct imaging of the molecules, because it works with an almost closed cycling transition. This allows multiple absorption of photons and thus results in a much stronger signal. This is crucial for the chosen imaging technique, called absorption imaging [37]. The $^1S_0 \leftrightarrow {}^1P_1$ transition of the ^{88}Sr atoms is used for imaging.

Two images are taken shortly after each other. At the first, the atoms inside of the chamber are illuminated by the imaging laser and an image is taken with a CCD camera while at the second a few μs later, no atoms are present in the trap anymore as they are wiped away with an intense 461 nm light pulse. Hence, an image of only the imaging laser light is taken. During the first image the atoms absorbed photons which leaves a shadow at their position, whereas the second image shows the intensity of the light when there are no atoms. Applying the Beer-Lambert law

$$A = \ln \frac{I_0}{I}, \tag{3.8}$$

where I_0 the intensity of the second (background) image and I the intensity of the first (atom) image, the optical density A for each pixel in the image can be calculated. This density is directly proportional to the number of atoms imaged. The light used for imaging is extracted by a polarizing beam splitter cube (PBS) from the 461 nm light source and guided to the experiment.

Data Acquisition

To control the setup, an in-house written Windows program communicates with the experiment via a National Instruments Data Aquisition system (NIDAQ). Another program called LabExe is used for data taking. Both were developed by Gael Reinaudi, a former group member. After the CCD camera receives the trigger signals from the NIDAQ and takes the images, they are sent back to the computer via USB. This triggers LabExe. LabExe uses the two consecutively taken images and calculates the optical density live using the intensities of the pixels by applying the Beer-Lambert law. It displays the density and it enables the access to this information with LabExe's applications like a signal counter. Since the optical density is proportional to the

number of atoms, one can, for example, receive this number inside of a chosen area of interest (AOI) after calibration. The software can also control the acoustic-optical modulators (AOMs) which are used to change the frequency of the probe light. By sweeping the probe frequency, traces can be taken. For the investigation of the PD dynamics, the images received from the camera are saved on the hard-drive and post processed, so averaging over a larger number of images and background subtraction for a better result is possible (Chap.7).

3.2 Axial Imaging Setup

The initial perspective of choice to look at the cigar shaped atom cloud formed by the lattice was from the side (x-axis in Fig. 3.3). For a variety of measurements and especially for investigation of the PD dynamics of $^{88}Sr_2$, it is very useful to additionally look on-axis with the cigar shaped atoms cloud and the lattice (z-axis). In PD, the products fly apart from each other in a pattern cylindrically symmetric about the laser's polarization axis. When looking at the pattern on-axis, this becomes easily visible, since the origin of the PD looks like a point from this angle. The taken image is then a 2D projection of the Newton's sphere on the camera CCD. In contrast, when imaging from the side, the origins of the PD are in each pancake and hence distributed along the cigar. Instead of a ring, a mixture of a ring and a cigar shaped pattern gets projected on the CCD which makes it more difficult to interpret the result. To enable the on-axis perspective, the experiment was enhanced with an IDS-UI-2140SE-M-GL CCD camera from IDS Imaging [38], a Navitar Zoom 6000 objective with a 0.5x lens attachment and a 2.0x short adapter [39] and the optics to realize the second imaging beam path.

Fig. 3.5 presents a scheme of the two imaging setups. Blue imaging light from the 461 nm source, guided to the experiment by a fiber, is split into two imaging beams by a non-polarizing beam splitter (NPBS) cube with a 50:50 ratio. We chose a NPBS because drifts in the polarization of the light due to the fiber would lead to fluctuating light intensities after the beam splitter. These are highly undesirable for absorption imaging. While the original setup remains unaltered, the new optics guiding the axial beam to the chamber window and combining it with the lattice and probe beam paths is installed working around it. Fig. 3.6shows a picture of the optics right before the beams enter the chamber. Imaging path (A) represents the side imaging, path (B) the lattice and probe beams. Initially, a pellicle was planned to combine the axial imaging beam with the paths of the lattice and probe laser right before the 150 mm focusing lens. This turned out to be not feasible, since the lens' antireflection coating is not compatible with the wavelength of the imaging beam. Additionally, the alignment of

the beam focused by this lens would have been unnecessarily complicated and lead to a poor quality beam. Instead, a D-shaped mirror is placed between the chamber and the lens close to the entrance window. The mirror is installed, so that the imaging beam is nearly parallel to the lattice and probe beams, i.e. very close without clipping. After careful alignment, the beam now illuminates the atoms and is extracted from the path of lattice and probe by another D-shaped mirror at the other end of the chamber. This mirror is also placed between the window and the chamber and near the other beams. Unlike the lattice and probe beams, the imaging beams are not focused. For imaging, a focus beam is not desirable and instead a collimated beam is ideal. The beam collimated with the fiber stage right after the fiber satisfies this criterion well enough. The little divergence present leads to a wider waist of the beam for the axial camera due to the longer beam path. Higher light intensity for the axial in comparison to the side imaging is therefore necessary. To provide that, the overall intensity is increased and a ND filter is installed in the side imaging beam path.

When installing the optics for the axial imaging after the chamber it was important to take the 17.5 cm maximal focal length of the objective into account. The geometry of the chamber only allows about 5.5 cm of beam path after the window. To guide the beam into the objective with using as little space as possible, another D-shaped mirror right before the objective is found to be the best solution. The use of D-shaped mirrors to introduce and extract the imaging beam to be parallel with the lattice beam results in a slight incident angle towards the atom cloud. Since this angle is in the range of a few degree we expect no vital effect on the resulting image. Fig. 3.3 shows a schematic view of the two imaging beams and the atoms cloud.

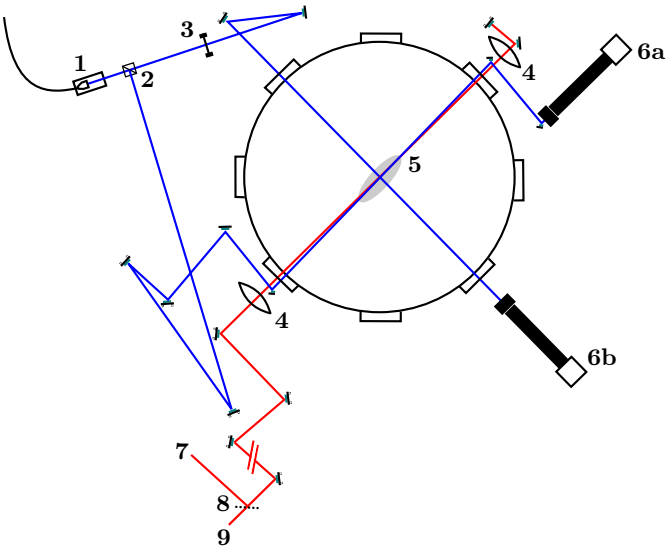

Figure 3.5: The imaging setup. Light with a wavelength of 460.86 nm is guided to the experiment by an optical fiber (1). A polarizing beam splitter, PBS (2), splits the beam in two paths. The side imaging beam passes an ND filter (3), while the axial imaging beam is guided via several mirrors behind the focusing lens of the lattice and probe beams (4). They illuminate the atom cloud (5) from the two perspectives. The axial (6a) and the side (6b) images are taken by two CCD cameras. The lattice (7) is combined using an pellicle (8) with the probe beam (9).

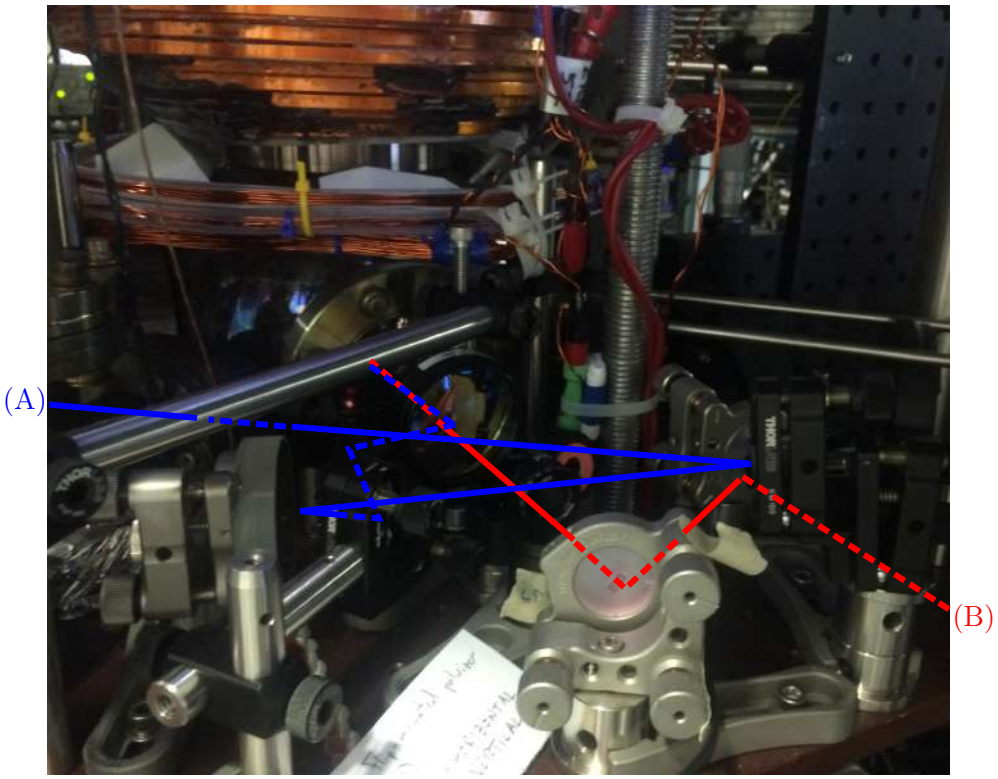

Figure 3.6: The path of the axial imaging beam (A) and the combined lattice and probe beams (B) before the vaccum chamber.

Chapter 4

Dynamics of Photodissociation in an Optical Lattice

Using an optical lattice with PD is a new technique which has interesting advantages over commonly used PD techniques. We are able to perform recoil- and doppler-free measurements by probing in the Lamb-Dicke and resolved sideband regimes. We also have exact control over the molecular quantum states we want to investigate on, since we operate in the ultracold regime. One application of this is to resolve absolute binding energies by relating the frequencies of the measured transitions to the frequency of an well known asymptote of an exited state manifold of the molecule of interest. This can be accomplished by taking traces of PD from ground states to the asymptote [19, 40–42]. Another application is the investigation of the angular distribution of the PD which can give us information about the initial, intermediate or the final unbound quantum state, depending on the experiment. Using the reference of a known asymptote to obtain the absolute frequencies applied is also possible for these measurements. The asymptotes we relate to in these experiments were of the $^1S_0$-$^3P_1$ or $^1S_0$-$^1S_0$ manifold for 1-photon PD and of the $^3P_1$-$^3P_1$ manifold for 2-photon PD. In the first part of this chapter, the process of the determination of the frequency of an asymptote, hence a shelf start, will be described. Additionally, limiting factors on the precision of using an optical lattice with PD like the effects of the dimensionality of the lattice, an offset on the resulting energies of the photofragments due to the lattice trap depth and other restrictions will be discussed.

In our experiment, it is possible to determine the radius of photodissociated fragments which have a square root dependence $R \propto \sqrt{E_{kin}}$ on their kinetic energies. By extrapolation of the kinetic energy to zero, it was feasible to obtain a value for the trap depth of the lattice. The goal of the measurement was to proof the principle. In order to

assess the lattice depth precisely, a more careful control of systematic errors would be needed. This will be described in the second part of this chapter.

4.1 Intercombination Line as Energy Reference

For each experiment in this thesis, we took a trace of a shelf start in order to relate each frequency detuning applied to a absolutely known energy. The traces were recorded by counting the signal strength, thus the live calculated optical density with LabExe. We employed on-axis imaging. An example of the line shape of the shelf start, in this case of the $X(-1,0) \rightarrow {}^1S_0\text{-}{}^3P_1$ transition, is given in Fig. 4.1 together with the line shape fit. The fit function can be derived by treating PD as a reverse photoassociation (PA) process [42]:

$$W_{2D,PD}(f) = W_0 + B\left\{\arctan\left[\frac{2(f-f_0)}{\gamma}\right] + \frac{\pi}{2}\right\}. \tag{4.1}$$

Here, W_0 is an experimental background offset, B is a parameter of the shelf amplitude, γ is the width of the PD transition, f is the frequency of the probe laser, and f_0 is the shelf start. When photodissociated, the fragments, here ^{88}Sr atoms, receive the excessive energy not needed to dissociate the molecule as kinetic energy. If this kinetic energy is lower than the lattice potential, the atoms remain in the trap. This is the case when measuring the shelf start, as frequencies only up to several hundred kHz above the shelf start are applied in order to take the trace. Having this in mind, and since the 'pancake' shaped lattice confines one degree of freedom of the atoms, the line shape could be derived assuming a quasi-2D environment. The same assumption was taken for the quasi-2D PA line shape the derivation of the PD line shape is based on, characterized by $W_{2D,PA}(f) \propto \int_0^\infty L(\delta,\epsilon)e^{-\epsilon/k_BT}d\epsilon/(k_BT)$ [19]. Here, ϵ is the thermal energy and T the temperature of the free atoms, k_B the Boltzmann factor and the Lorentzian is described by $L(\delta,\epsilon) \propto 1/[(\epsilon/h+\delta)^2 + (\gamma/4)^2]$ with γ being the FWHM. The PA line shape takes the Boltzmann distribution of the initial atom sample into account as it integrates over all possible relative energies of the two free atoms. For PD this factor can be dropped, since the relative energy of the final two atoms is fixed by the dissociation frequency. Therefore, the factor for the thermal energies ϵ is replaced by a fixed dissociation energy $h(f-f_0)$ which eventually after integration of $L(f-f_0,\epsilon)$ yields Eq. 4.1, where γ determines the rounding of the edges of the step function. It is important to mention, that this is only valid for weak laser intensities, so either minimal or no broadening of the line shape due to large powers occurs. The 3D line shape, derived based on the same approach would

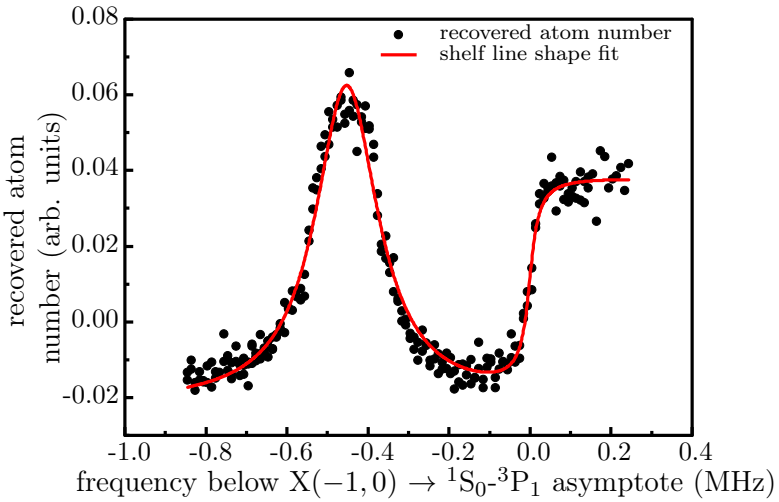

Figure 4.1: The shelf line shape of the ^{1}S$_0$-^{3}P$_1$ manifold with fit when photodissociating from the X$(-1,0)$ ground state. The abscissa was scaled so the shelf start is set at 0 MHz as reference. Details about the fit function of the shelf line shape can be found in the text. Additionally, the fit function seen here includes the peak on the left side of the shelf which is the signal of a bound-bound transition to the $(1)0_u^+(-1,1)$ state with a binding energy of about 452 kHz [19].

be $W_{3D,PD}(f) \propto \int_0^\infty L(f,\epsilon)\sqrt{\epsilon}\mathrm{d}\epsilon \propto [(f-f_0)+\sqrt{(f-f_0)^2+\gamma^2/4}]^{\frac{1}{2}}$. It turned out though, that the observed signal can be better explained with the 2D line shape due to the limiting lattice dimension.

4.2 Measurement of the Lattice Trap Depth

This measurement proofs that it is generally possible to obtain the lattice trap depth by measuring the kinetic energy of PD fragments, looking at their distance from the PD origin and comparing the extrapolated frequency of the laser for zero kinetic energy with the frequency of the laser at the shelf start. The difference between those two values is the lattice trap depth. The order of magnitude of calculated value of about 1 MHz lattice trap depth could be verified.

To obtain the depth, a 1-photon PD from X$(-1,0)$ → ^{1}S$_0$-^{3}P$_1$ asymptote was performed. The axial images were improved with in-house written Matlab programs and analyzed with pBasexL. These processes are described in detail in Chap. 7.

Description of Measurement

The relevant transitions for this measurement are shown in the scheme on the left side of Fig. 4.2. First, as in every experiment discussed here, molecules were created from a

ultracold atom cloud by PA [43–45]. A laser with a wavelength of about 689 nm used a transition near the $^1S_0 \leftrightarrow {}^3P_1$ intercombination line to prepare a molecule in the $(1)0_u^+(-4,1)$ state [45]. The binding energy of this state is about 1084 MHz [19]. From here, the molecules decay mainly to the $X(-1,0)$ and $X(-1,2)$ ground states which are the initial states for all of the experiments covered in this work. In the figure the PA transition is represented by the blue arrow and the two decays by the yellow wavy arrows.

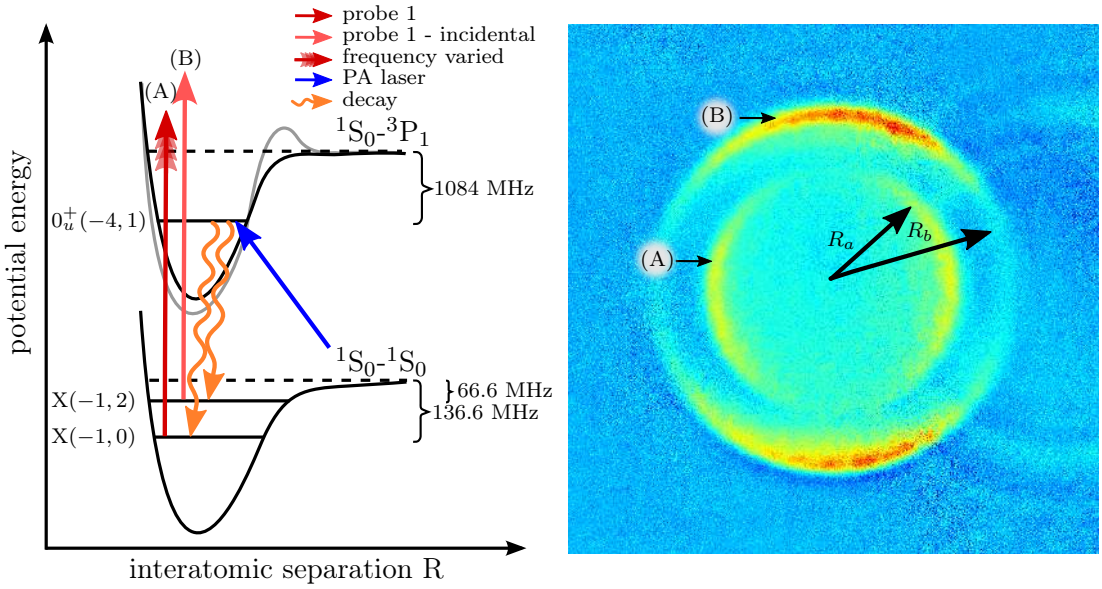

Figure 4.2: Signal (A) caused by PD from the $X(-1,0)$ ground state with a binding energy of 136.6 is the signal we are interested in. Another signal (B) occurs due to the incidental PD from the $X(-1,2)$ ground state with a binding energy of 66.6(2) MHz [46]. The PA from atoms to molecules is illustrated by the blue laser and the decay to the initial states of the experiment by the two yellow arrows. In the resulting processed image on the right, false colors are applied. Blue here stands for low and red for high signal. The two radii of the two signal rings are indicated.

From the $X(-1,0)$ state, the molecule was photodissociated to the $^1S_0$-$^3P_1$ shelf (dark red arrow) which led to the signal (A) in the axial image (right side Fig. 4.2). Since the $X(-1,2)$ state was also populated, an incidental transition, resulting in signal (B), occurred. For measuring the lattice trap depth, we observed the square root dependence of radius and kinetic energy. This can be conclusively illustrated by looking at the different radii R_a and R_b of the two signals in the image on the right side of Fig. 4.2. The binding energies of the $X(-1,0)$ and $X(-1,2)$ states are 136.64(1) MHz[1] and 66.6(2) MHz, respectively. Hence, the atoms of the $X(-1,2)$ ring had an excess of kinetic energy of 70.1(4) MHz [46]. Due to the difference in kinetic energy, a clear distinction between the two signals was possible when waiting for several hundred μs before taking the image, since one atom ring flew away faster. In order to obtain the

[1]Not yet published result from measurements of our group.

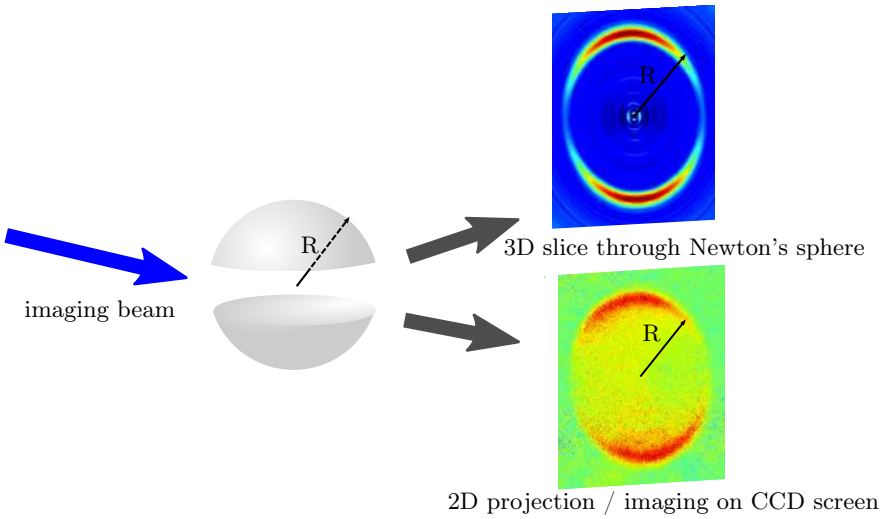

Figure 4.3: When photodissociating, the fragments fly spherically apart. This sphere is called a Newton's sphere. When imaging, the 2D projection of this sphere is captured. In order to receive information about the initial angular distribution of the fragments, one has to calculate the slice through the sphere. Here, this is done by using Abel transformation and in particular an algorithm called pBasex.

radii of the rings from this image it first had to be analyzed. The image represents the projection of the Newton's spheres the atoms occupy on the camera CCD. This becomes more clear when looking at Fig. 4.3. Thus, the rings one can see here do not represent the original 3D distribution of the atoms and the reconstruction of this distribution, which one can visualize as a slice through the sphere, was necessary to retrieve the correct radii of the rings. This is done by a program called pBasexL (for an exact description of the analysis see Chap. 7). The analysis with pBasexL provides the potential energy surface (PES) data of the image. The PES data contains information about the energy of the atoms, thus here the radial distribution of the signal rings in the image. It possible to assess the radius of the spheres of the fragments flying apart with this information. The term PES is used here in accordance to the naming conventions in pBasexL.

Result, Modeling & Discussion

A plot of the two radii vs. frequency detuning of the probe laser is given Fig. 4.4a. The kinetic energy of the imaged atoms relates to the frequency detuning above the shelf with $E_{kin} = hf_{det} - U_0$, where $h = 6.62606957 \cdot 10^{-34}$Js is the Plank-constant and U_0 is the lattice trap depth. The atoms first need to overcome the potential of the lattice before being able to fly apart. The shelf start at $f_{det} = 0$ MHz was determined like described in the section above. The correlation between the radius and the kinetic energy can be derived from conservation of energy. As the molecules

are held at nearly rest in the lattice, one can say that when a homonuclear diatomic molecule is dissociated, the resulting atoms must have the same momentum and, hence, same velocity in the laboratory frame. From energy conservation we obtain:

$$E_{kin} = \frac{1}{2} m_{88} \mathrm{v}_1^2 + \frac{1}{2} m_{88} \mathrm{v}_2^2 = m_{88} \mathrm{v}^2 \quad \text{with} \quad \mathrm{v} = \mathrm{v}_2 = \mathrm{v}_2 \tag{4.2}$$

where $m_{88} = 87.905612542\mathrm{u} = 1.45970691 \cdot 10^{-25}\mathrm{kg}$ [32] is the mass of one ^{88}Sr atom and $\mathrm{v} = \frac{R}{T}$ is the velocity of the atoms. Solving this equation for R yields the fit function:

$$R = T\sqrt{\frac{h}{m_{88}}}(f_{det} - \frac{U_0}{h})^{1/2} \tag{4.3}$$

The fits to the data of PD from $\mathrm{X}(-1,0)$ and $\mathrm{X}(-1,2)$ are plotted in graph (a) of Fig. 4.4. Graphs (b) and (c) show the residuals. The detuning of the laser above the shelf start f_{det} is what we have control of, so with Eq. 4.3 it is now possible to receive the lattice trap depth U_0. Plot (d) of Fig. 4.4 illustrates this clearly. On the left side, one can see the trace of the shelf with the shelf start at $f_{det} = 0$ MHz while the extrapolation of the energy is plotted in red on the right side. This analysis was performed on the $\mathrm{X}(-1,0)$ signal. A lattice depth of $U_0/h = 1.04(2)$ MHz was measured.

It is possible to calculate the lattice trap depth U_0, if the trap frequency $f_{trap,z}$ is known. This frequency can be determined by measuring the sideband spacing of the lattice [47]. The relation between this frequency and the lattice depth is:

$$\frac{U_0}{h} = \frac{M\lambda^2}{2h} \cdot f_{trap,z}^2, \tag{4.4}$$

where $M = 2m_{88} = 2.91941382 * 10^{-25}\mathrm{kg}$, $\lambda = 912.34 * 10^{-9}\mathrm{m}$ is the wavelength of the lattice laser, and $f_{trap} = 4.65 * 10^3 \mathrm{Hz}/\sqrt{\mathrm{mW}} \times \sqrt{P_{lat}}$ is the measured trap frequency which depends on the power of the lattice. P_{lat} was about 198(10) mW. One then receives a lattice trap depth of about $U_0/h = 0.78(5)$ MHz. The disagreement of this value to the measured value is about 0.26 MHz. Several reasons could cause this disagreement. An explanation could be found on the experimental side, for example due to drifts in the laser calibrations over the time between separate measurements and powers as well as probe light shifts which we have seen in our experiments. It is also possible that the kinetic energy of the atoms is altered by the photons emitted when they de-exite after the dissociation process. For that, also the location, i.e. if emitted inside or outside of the lattice, can play an important role for a possible change in kinetic energy. Finally, in this measurement we assumed that the lattice trap depth is the same

for the bound molecular ground state, the exited state we are dissociating to and the unbound state the atoms are in. This is just an approximation and different states see slightly distinct lattice potentials. We carefully zeroed the magnetic field before taking the measurement, hence we expect no quadratic Zeeman shifts [40].

In this experiment, we could show that measuring the lattice trap depth by investigating the radius of the fragments of PD is generally possible, which was what we aimed for. When intending to employ this technique to obtain the depth precisely, a thorough analysis of all the challenges mentioned would be necessary, which we expect to be feasible with some amount of effort.

It was mentioned earlier, that the relative frequency difference in the binding energies of the $X(-1, 0)$ and $X(-1, 2)$ can be seen in Fig. 4.2 and that it is 70.1(4) MHz derived using two-photon photoassociation spectra [46]. Since the two states saw the same lattice trap depth, we could measure a difference in binding energy of 69.3(7) MHz. The two measurements agree within the error.

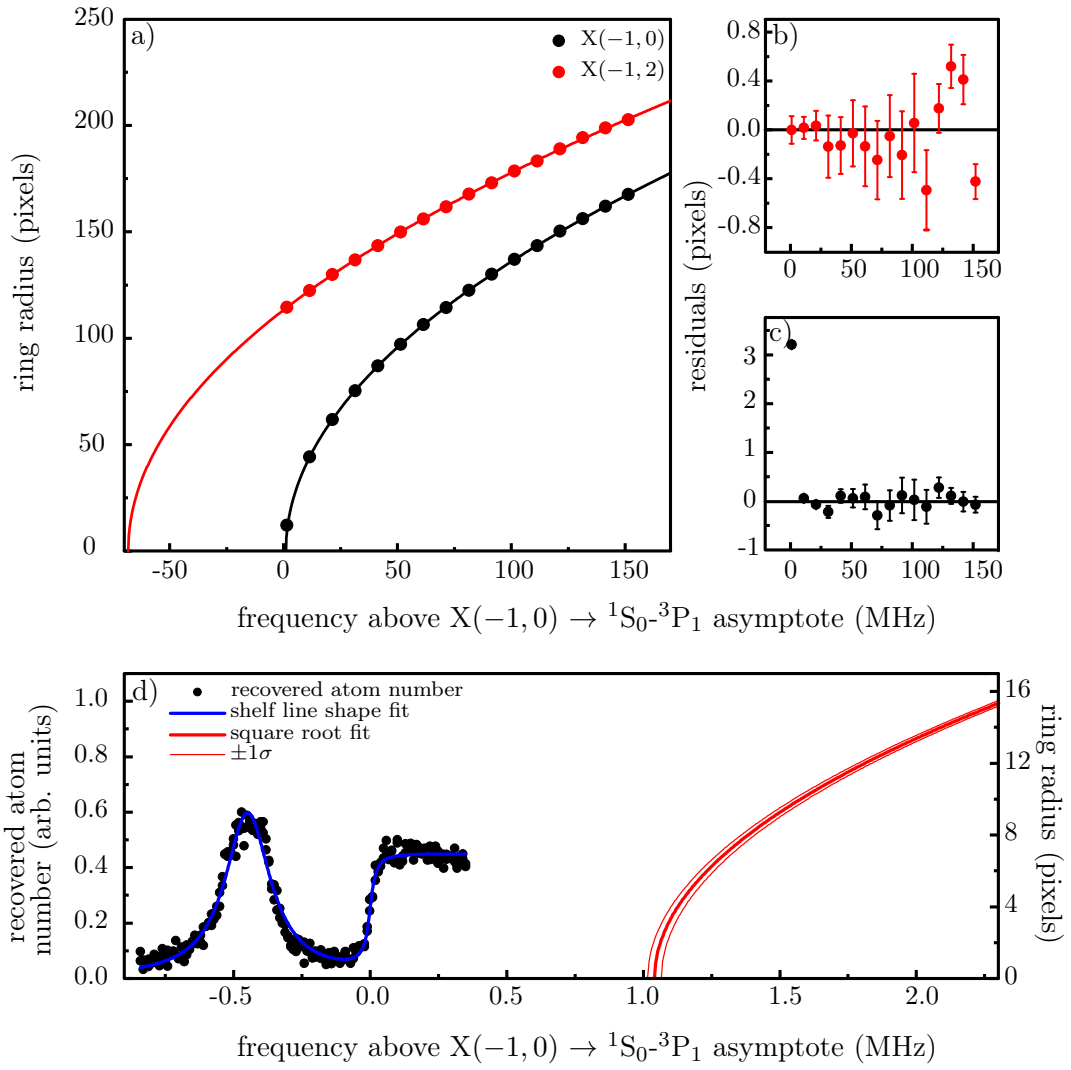

Figure 4.4: In a), the radius of the two signal rings is plotted against the frequency above the ^{1}S$_0$-^{3}P$_1$ asymptote when dissociating from X$(-1, 0)$. b) and c) show the residuals, while in d) the shelf line on the left side and a zoomed in version of the X$(-1, 0)$ plot in a) is illustrated. The effect of the depth of the lattice becomes visible, as the dissociation fragments can only be seen after 1.04(2) MHz and not right above at the dissociation threshold.

Chapter 5

1-photon Photodissociation

In this chapter, first a basic theoretical background of 1-photon photodissociation is provided. In particular, the way the angular distribution can be characterized by an anisotropy parameter β is discussed. In the first experiment described in this chapter, we are able to obtain a preliminary value for the height of the barrier of the $(1)1_u$ state potential by measuring the anisotropy parameters for different PD energies. The intention of the second experiment is to investigate the angular distribution of a 1-photon PD $(1)1_g(-1,1) \rightarrow {}^1\mathrm{S}_0$-${}^1\mathrm{S}_0$ shelf. This is particularly interesting, because the selection rules do not allow E1 transitions, meaning any observed PD signal must be necessarily of the M1 or E2 character (neglecting even higher order transitions due to their much lower signal strength). As far as we know, this has not been explored before. While we are unable to clearly resolve the angular distribution of the photofragments, future measurements are possibly able to improve the efficiency of this process. This experiment propounds a direction of further research with this experimental system and theorists are currently working on a model to describe the processes. In addition to this proof-of-concept, a way to measure the frequency of the ${}^1\mathrm{S}_0$-${}^1\mathrm{S}_0$ asymptote by assessing the radii of the signal ring like in Chapter 4 is discussed.

In this chapter, the notations 1_u, 0_u^+, 1_g and 0_g^+ will refer to the $(1)1_u$, $(1)0_u^+$, $(1)1_g$ and $(1)0_g^+$ potentials, respectively.

5.1 Theoretical Background

A well established formula for the angular distribution of photofragments of a 1-photon PD process can be found in literature [48–50]:

$$I(\theta) = I_0[1 + \beta P_2(\cos\theta)] \tag{5.1}$$

where $I(\theta)$ is the intensity, here corresponding to the density of Strontium atoms $A(\theta)$ in the resulting images, at the angle θ between the polarization axis of the dissociating laser and the direction of the fragments. I_0 is a coefficient, $P_2(x) = 0.5(3x^2 - 1)$ is the second order Legendre polynomial and β is the anisotropy parameter which is $\beta = 2$ for purely parallel and $\beta = -1$ for purely perpendicular transitions. This equation is an approximation and is only valid when the axial recoil approximation holds. That is, when the dissociation occurs significantly faster than the internal motions of the molecule so that the PD fragments are ejected along the direction of the internuclear axis at the time of the photon absorption.

It is possible to describe β in Eq. 5.1 with [51]

$$\beta = \beta_0 P_2(\cos\gamma) \tag{5.2}$$

where β_0 is either 2 or -1 and γ is the angle between the direction of the fragments when the axial recoil approximation holds and the actual direction. γ can be approximately calculated using the following formula:

$$\gamma = \int_{R_0}^{\infty} \frac{\mathbf{J}\mathrm{d}R}{\mathbf{p}(R)R^2} \tag{5.3}$$

where $\mathbf{J} = [J(J+1)]^{1/2}\hbar$, $\mathbf{p}(R) = (2\mu[E - V(R)] - \mathbf{J}^2/R^2)^{1/2}$ is the momentum of the dissociation which depends on the dissociation energy E and the potential of the molecule $V(R)$ and R is the internuclear separation. Most of the experiments in this thesis are conducted from the X$(-1, 0)$ where $\mathbf{J} = 0$ and the axial recoil approximation holds. We assume that this is also valid for higher energies in experiments using intermediate states like 2-photon PD.

By symmetry considerations, the transition dipole moment μ of diatomic molecules must lie either parallel or perpendicular to the internuclear axis (Fig. 5.1). Therefore, when we assume linear polarization of the dissociating laser, only parallel or perpendicular transitions are possible if the axial recoil approximation holds. From Eq. 5.1 we know that for a parallel transition, the distribution is $\cos^2\theta$, for a perpendicular transition is $\sin^2\theta$. In the experiments we measured β and received information about the type of transition contributing to the signal we observed. In some experiments we detected a mix of the two distributions. This indicated, that not only one potential of a certain manifold is accessed but at least two dissociation channels contribute.

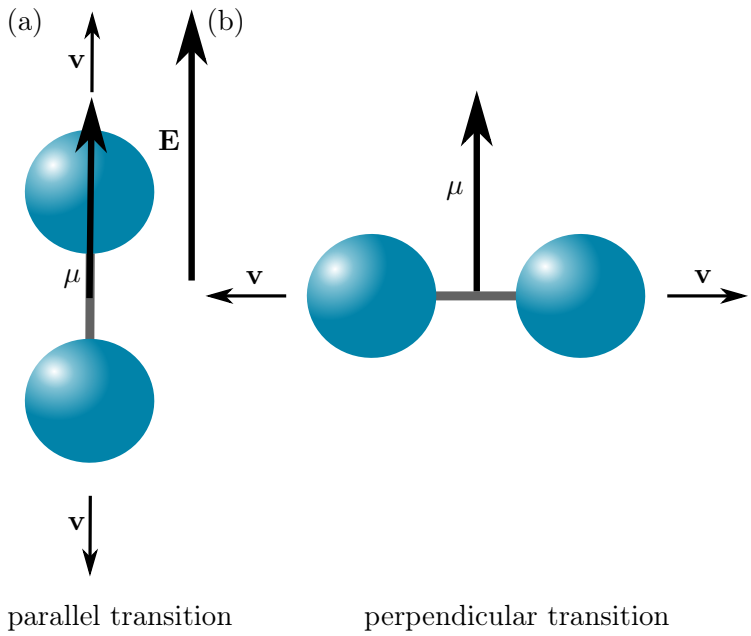

Figure 5.1: The transition dipole moment μ. When photodissociating, it is parallel to the electic field of the probe light. Thus, when μ is on the internuclear axis, the atoms fly apart parallel to **E** and when μ is perpendicular to the internuclear axis, they fly apart perpendicular to **E**.

5.2 Preliminary Barrier Height of $(1)1_u$ Potential Using $X(-1,0) \rightarrow {}^1S_0$-${}^3P_1$ Transition

In Chap. 2, it was shown that the 1_u potential of the ${}^3P_1$-${}^1S_0$ manifold has a barrier, whereas the 0_u potential has almost no barrier due to the sign before the C_3 term in its long range potential (further discussion here [52]). The goal of this experiment is to determine the height of this barrier experimentally for the angular momentum of the exited state with J'= 1. We did so by investigating how the angular distribution of the PD from the $X(-1,0)$ ground state to the 0_u^+ and 1_u potentials of the ${}^3P_1$-${}^1S_0$ manifold changes with frequency detuning of the probe laser. Since the transition to the 0_u^+ and 1_u potentials are parallel ($\beta = 2$) and perpendicular ($\beta = -1$), respectively, we can measure the contribution of these transitions to the signal depending on the energy above the shelf. For low energies, the signal of the parallel $X(-1,0) \rightarrow 0_u^+$ transition dominates since the potential has almost no potential barrier. For higher energies the signal from the 1_u potential becomes more present and by using a toy model, it is possible to obtain a preliminary value for the barrier height. A more accurate model to describe the expected change of β is currently being developed by a collaborating theory group.

Description of Measurement

The potentials and the excitation paths involved in this process are schemed in Fig. 5.2. First, as in all the other experiments in this thesis, the $X(-1,0)$ and $X(-1,2)$ ground states were prepared using PA (not shown in scheme for clarity). The probe laser (dark red probe arrow) excited the $X(-1,0)$ population to frequencies above the $^1S_0$-$^3P_1$ asymptote. The tuning of the probe laser to dissociate the $X(-1,0)$ state with a binding energy of 136.64(1) MHz caused a incidental dissociation signal of the $X(-1,2)$ population (light red probe arrow), which we were not interested in. In Chap. 4 it was discussed, that the difference in binding energy of 70.1 MHz between the two states is reflected in the larger radius of the signal ring. On the right side of Fig. 5.2, an example image for a frequency detuning of 60 MHz into the shelf with labels for the two rings is shown. For processing the data and evaluating the β values, not only the pBasex inversion method but also the horizontal integration method was used here. The horizontal integration method is highly dependent on the quality of the signal and works best with only one ring present. Therefore, we depleted the $X(-1,2)$ population before taking data with this method. We used a second laser to pump the $X(-1,2)$ population back to the 1084 MHz state (blue depletion arrow). From there, as in the PA process, the population decays mainly into $X(-1,0)$ and back to the $X(-1,2)$. With a long enough depletion, it was possible to eliminate the whole $X(-1,2)$ population. This also led to an slight increase in $X(-1,0)$ signal, whereas some of the population was lost to other transitions. A comparison of the measurement with and without the depletion of the $X(-1,2)$ population which clearly reveals the advantage when there is no $X(-1,2)$ ring present is made in the Chap. 7 in Fig. 7.4.

The start of the shelf was determined after taking the data. In total, four data sets were taken. For each of the two analysis methods, one set scanned over a frequency from 0 MHz to 30 MHz above the shelf in steps of 2 MHz - 4 MHz and one scanned from 0 MHz to 150 MHz in steps of 10 MHz. Splitting the measurement into a low detuning and a high detuning data set was convenient since larger expansion times could be applied to the low detuning set with the signal still being inside the image. This led to a better resolution for the low detuning images, which was especially important since the transition region from a parallel to perpendicular dissociation pattern occurred at low frequency detuning. The settings for the four data sets are presented in Tab. 5.1

Results, Modeling & Discussion

The result for the β parameters is presented in Fig. 5.3. To generate error bars for the pBasex inversion method, the images were analyzed several times with different centers within a square of a few pixels around the center calculated by the software. Addition-

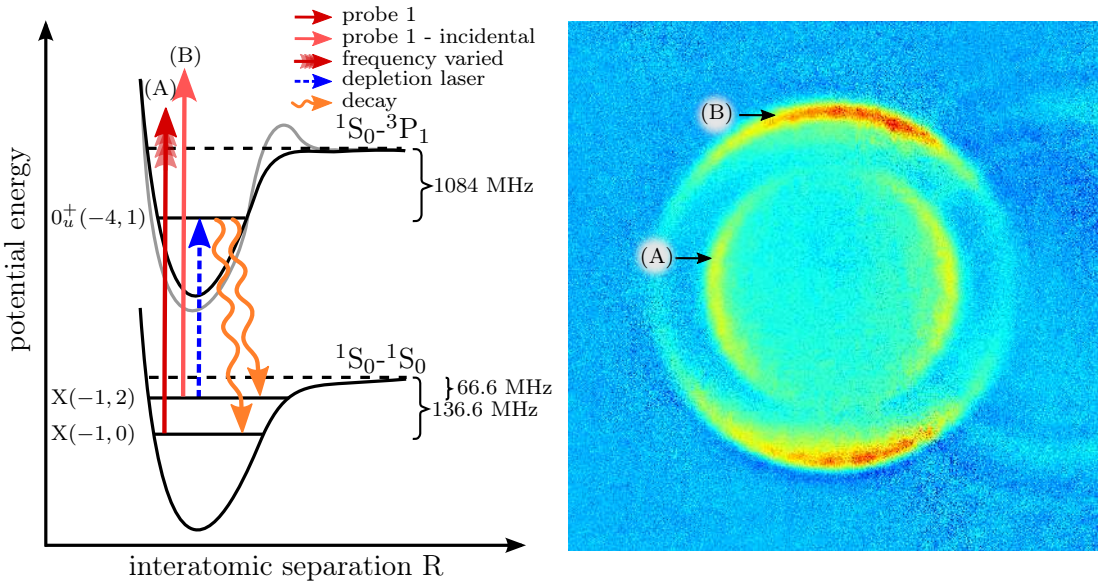

Figure 5.2: Signal (A) caused by PD from the X$(-1,0)$ ground state with a binding energy of about 136.6 is the signal we are interested in. Another signal (B) occurs due to the incidental PD from the X$(-1,2)$ ground state with a binding energy of about 66.6 MHz. In order to remove the X$(-1,2)$ signal we are not interested in, it is possible to deplete the X$(-1,2)$ population with another laser (dotted blue). This leads to a decay to the initial ground states. When depleting long enough, one can remove signal (B) almost completely. The image on the right shows both signals.

Method	probe pulse time $[\mu s]$	expansion time $[\mu s]$
pBasex inversion (low detuning)	20	800
pBasex inversion (high detuing)	10	450
horizontal integration (low detuning)	20	600
horizontal integration (high detuning)	10	450

Table 5.1: Probe pule and expansion times applied for the measurements.

ally, different options of symmetrization of the image were selected. This has been done the same way in papers like [53] where pBasexL was used. The error of the horizontal integration is given by the fit. As visible in the plot, there is a difference between the two techniques in the β value for the same frequency. We assume the horizontal integration method to be more accurate. The pBasex inversion is highly dependent on the background noise which could cause the difference. With our background reduction in several steps, described in Chap. 7, we were able to increase the signal-to-noise ratio significantly. Nevertheless, our setup is not background free since effects like photon shot noise, optical perturbations or hardware restrictions of the camera always play a role in absorption imaging. In contrast, velocity map imaging experiments like [53], where the pBasex algorithm is usually applied, have a low background noise since a signal is only recorded once an ion hits the detector screen.

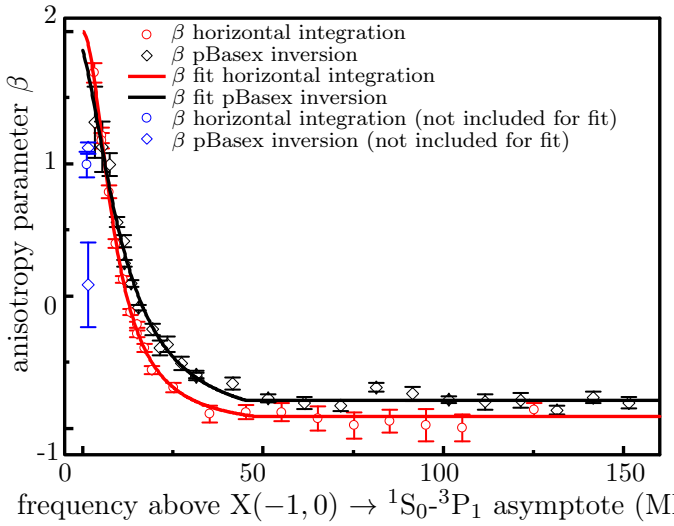

Figure 5.3: Plot of the anisotropy parameter β vs. the frequency above the $^1S_0$-$^3P_1$ shelf when photodissociating from X$(-1,0)$. We analyzed the images with the pBasex inversion and the horizontal integration. The fits result in a preliminary barrier height of $\epsilon_{B,inv} = 47.7(3.4)$ and $\epsilon_{B,int} = 47.9(7.9)$.

The symmetry of the ground state X$(-1,0)$ is g (even). Therefore, E1 transitions to the 1_u and 0_u^+ are allowed and dominate the signal. We have detected M1 and E2 transitions to 1_g, but not to 0_g^+. Depending on the orientation of the dipole transition moment of the molecule, which is either parallel or perpendicular to the molecular axis, X$(-1,0) \rightarrow 0_u^+$ transitions or X$(-1,0) \rightarrow 1_u$ transitions occur, respectively.

As can be seen in the plot, β is close to 2 for small frequencies above the shelf. With increasing frequency, the value of β decreases and finally asymptotically approaches a value slightly larger than -1, since there is always some contribution of the 0_u^+ potential for high frequencies. Consequently, we could measure when the 1_u potential was fully accessed, which was when the dissociation energy ϵ is equal or higher than the potential barrier ϵ_B. The 0_u^+ channel is expected to be nearly independent of the frequency of the dissociating light. In contrast, we assume that for detuning very little above, the asymptote no transitions to the 1_u potential occurred. This changed with increasing the energy of the fragments due to the shape of the barrier and the signal of the 1_u potential became stronger. This is in accordance with an increasing overall signal strength with higher frequencies we could observe. The barrier height also depends on the total angular momentum of the exited state J' as it becomes obvious in Eq. 2.3. A preliminary toy model for this process can be presented and was used to determine a rough barrier height, while a more sophisticated model is currently being worked out by theorists. Following the discussion above and taking [54] into account, we expect the 1_u potential contributes to the signal with

$$\omega(\epsilon) = R \times \begin{cases} (\epsilon/\epsilon_B)^P & \text{for } 0 \leqq \epsilon < \epsilon_B, \\ 1 & \text{for } \epsilon \geqq \epsilon_B. \end{cases} \tag{5.4}$$

where P is a fit parameter and R, the relative strength of 1_u compared to 0_u to the PD spectra. The anisotropy parameter can then be described with

$$\beta_{tot} = \frac{\beta_{0_u^+} + \omega(\epsilon)\beta_{1_u}}{1 + \omega(\epsilon)} \tag{5.5}$$

where $\beta_{0_u^+} = 2$ and $\beta_{1_u} = -1$. The fit of the data shown in Fig. 5.3 results in a barrier height of $\epsilon_{B,inv} = 47.7(3.4)$ MHz using the pBasex inversion method and $\epsilon_{B,int} = 47.9(7.9)$ MHz using the horizontal integration technique. In contrast to [54] P is a free parameter which results in $P_{inv} = 1.93(0.26)$ and $P_{int} = 2.06(0.17)$. This is a preliminary result based on the toy model, which explains the large discrepancy to the calculated value in Chap. 2 of $\epsilon_B \approx 24$ MHz. The next step is to apply a more accurate theoretical model and also an more careful measurement might be possible.

There are several reasons why β does not reach the value 2 in our measurement. Most likely is that since the signal is closer to the center for small frequencies it is thereby closer to the noise accumulation of the pBasex algorithm. Additionally, for very small detuning the atoms are just able to escape the lattice, but their ballistic motion is likely still affected by it. For larger detuning the kinetic energy is significantly higher and the potential of the lattice can be neglected. For these reasons, the first three points were not included in the fit. These values are at very small energies above the asymptote. We consider the ability to access these small energies already as an accomplishment by itself, which is made possible by working in the ultracold regime. Any influence of the breakdown of the axial recoil approximation on the data can be excluded since, following Sec. 5.1, there is no such effect for molecules with initial states with J=0.

5.3 Angular Distribution of M1 / E2 Transitions to $^1S_0$-$^1S_0$ Continuum and Determination of Asymptote

The main goal of this experiment is to show that we are able to detect molecular M1 and E2 PD transitions. To our knowledge, these PD transitions have not been observed in a controlled way yet. E2 and M1 transitions are weaker than E1 transitions and therefore, produce only a small signal which is usually not accessible due to the domination of the E1 signal. In case of a 1-photon PD from the $1_g(-1,1)$ to the $^1S_0$-$^1S_0$ shelf, M1

or E2 transitions are allowed since the excited 1_g state and the $^1S_0$-$^1S_0$ are both g (even) states. On the contrary, E1 transitions are here forbidden which enables us to investigate the M1 and E2 transitions.

Description of Measurement

The relevant transitions for this experiment are schemed in Fig. 5.4. The dissociation we are interested in is the one from the $1_g(-1,1)$ state of the $^1S_0$-$^3P_1$ manifold down to the $^1S_0$-$^1S_0$ shelf (dark blue probe 2 arrow) which created signal (A). This bound 1_g state has a binding energy of about 19 MHz. Before being able to perform this 1-photon dissociation, the molecule had to be excited to the 1_g state first. For populating the 1_g state from the $X(-1,0)$ state probe laser 1 was used (dark red probe 1 arrow). This laser also created a incidental ring of the $X(-1,2) \rightarrow {}^1S_0$-$^3P_1$ shelf transition (lower light red probe 1 arrow). The corresponding ring in Fig. 5.4 is the ring in the middle with the strongest signal (B). The outer third ring was created by a 2-photon process of probe laser 1 to the $^3P_1$-$^3P_1$ shelf (two light red probe 1 arrows and signal (C)). A fourth signal (D) was caused by the spontaneous decay of the $1_g(-1,1)$ state.

As one can picture from Fig. 5.4, lower frequencies of the probe 2 result in a higher energy of the atoms above the shelf, since the PD is driven from a higher to a lower state. In this experiment, data for frequency detuning above the shelf from 5 MHz to 20 MHz in steps of 5 MHz were taken. The four processed images are shown in Fig. 5.5. We determined the radii of the relevant signal (A) the same way as in Chap. 4 and as further described in Chap. 7 using the PES data from pBasexL. For this experiment the magnetic field was set to zero.

Results, Modeling & Discussion

When qualitatively looking at the four images, no drastic change of the angular distribution could be seen. Unfortunately, the signal due to M1 and E2 transitions is very weak. A group of theorists are currently working on modeling the occurring processes and we are performing more measurements. This experiment is very promising and could be the first controlled E2 PD.

It is also possible to present a new way to measure the frequency of the $^1S_0$-$^1S_0$ asymptote by assessing the radii of the signal rings and extrapolating the shelf start like we did for the measurement of the lattice trap depth in Chap. 4. The radii of the relevant rings (A) are plotted in Fig. 5.6 on the left side. The same fit function as in Chap. 4 was used to obtain a value for the shelf start at $-154.36(34)$ MHz in respect to the well known frequency of the $^1S_0$-$^3P_1$ asymptote. This reference was enabled with a trace

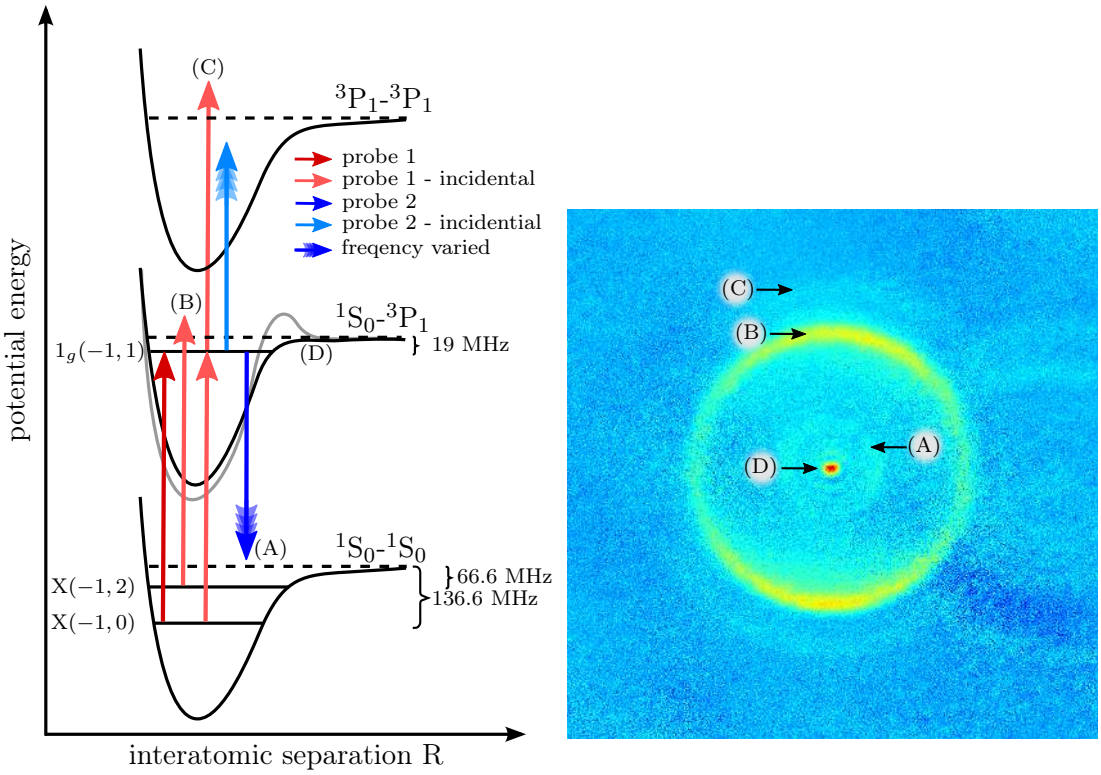

Figure 5.4: Signal (A) is caused by probe 2 performing PD from the $1_g(-1,1)$ state with a binding energy of about 19 MHz to the $^1S_0$-$^1S_0$ shelf. To first populate the $1_g(-1,1)$ state, probe 1 is used. Probe 1 also causes the incidental signals (B) and (C) by 1- and 2-photon PD from the X$(-1,2)$ state. Signal (D) is the decay of the $1_g(-1,1)$ state. For higher frequency detuning of probe 2, another signal caused by probe 2 can occur (not shown on the right).

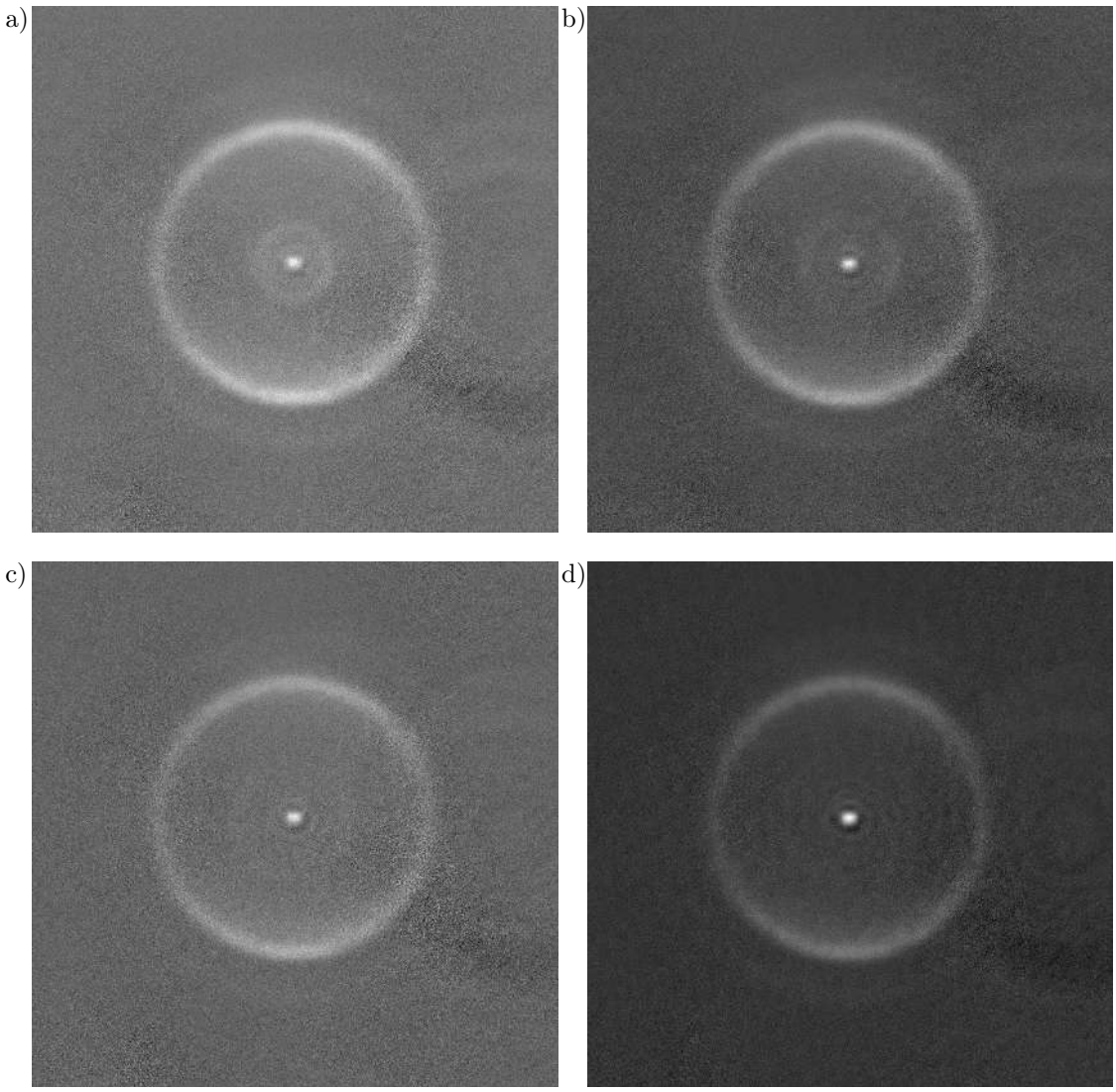

Figure 5.5: Processed images (no false colors) of the detuning above the $^1S_0$-$^1S_0$ asymptote from 5 MHz to 20 MHz in steps of 5 MHz. It is visible that the radius of the inner ring (Signal (A)) increases with higher frequencies into the shelf.

of the PD from the X$(-1,0)$ state to the ^{1}S$_0$-^{3}P$_1$ shelf taken after the measurement. In Fig. 5.6 the shelf trace with the 400 kHz state is plotted on the right side and the abscissa was set so the shelf start is at zero.

It is possible to receive an expected frequency detuning for the ^{1}S$_0$-^{1}S$_0$ shelf start by performing a quick calculation and by knowing the binding energies of the states involved. To support the explanation of the calculation, Fig. 5.7 will help. The reference asymptote ^{1}S$_0$-^{3}P$_1$ was determined by PD from the X$(-1,0)$ state. Hence, additionally to the frequency of the intercombination line, the laser has to overcome additionally the binding energy (arrow (2)). A laser connecting the ^{1}S$_0$-^{3}P$_1$ asymptote with the ^{1}S$_0$-^{1}S$_0$ asymptote (arrow (3)) has to have a relative detuning to the reference of $-136.64(1)$ MHz. Considering, that the PD laser (arrow (1)) connects the $1_g(-1,1)$ state to the ^{1}S$_0$-^{1}S$_0$ shelf, the frequency has to be smaller than (3) about the binding energy of 19.0420(38) [55]. This yields a value of $-136.64(1) - 19.0420(38) = -155.68(2)$ MHz. Taking the lattice trap depth of about 1 MHz into account, we expect the ^{1}S$_0$-^{1}S$_0$ asymptote to be at $-156.68(2)$ MHz.

The discrepancy between the expected value and the measured value of more than 2 MHz could be caused by several effects. First, since the main goal was to show only that this PD is possible, we only took four data points for that measurement. The stated error bars obtained from the Gaussian fits of the PES data to receive the radius might increase when using different centers in the image for the pBasex inversion. It has to be mentioned that they are almost certainly underestimated. Additionally, the already discussed probe light shifts and lattice effects, which we both have to further investigate, could influence the result.

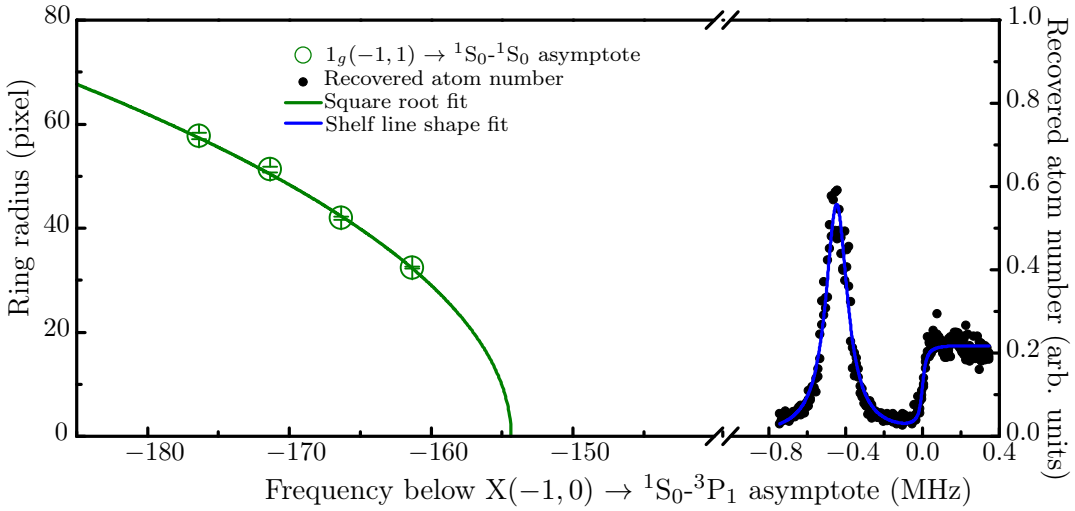

Figure 5.6: The PD from the initial state $X(-1,0)$ to the $^1S_0$-$^3P_1$ shelf serves as a well known reference, determined with a shelf lineshape fit plotted on the right side. On the left side, the radii of the rings of interest (signal (A)) are plotted against and fittet with a square root fit. R= 0 is then the shelf start of the $^1S_0$-$^1S_0$ with respect to the frequency of the $^1S_0$-$^3P_1$ asymptote.

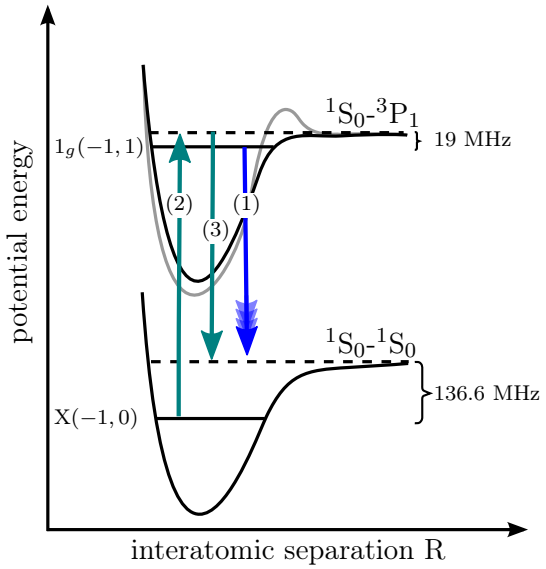

Figure 5.7: The goal of the experiment is the determination of the frequency of the $^1S_0$-$^1S_0$ asymptote by PD from the $1_g(-1,1)$ state (arrow (1)). The PD from the $X(-1,0)$ state to the $^1S_0$-$^3P_1$ asymptote (arrow (2)) is set as a reference. Arrow (1) is about the binding energy of 136.6 MHz shorter than (2). This would lead to the frequency of arrow (3). Additionally, (1) is another 19 MHz shorter, since it starts from the $1_g(-1,1)$ state.

Chapter 6

2-photon Photodissociation

Not only is it possible to conduct PD using one photon but we are also able to perform 2-photon PD. 2-photon PD is fundamentally different from PD via the $1_g(-1,1)$ state discussed in Sec. 5.3, which also used two photons. With 2-photon PD, the molecule may not even be in the intermediate state during the transition and the second photon can be absorbed immediately, whereas in Sec. 5.3 the molecule remained in the intermediate state for several μs before the dissociation. Thus, we speak of a 2-photon transition instead of two times a 1-photon transition. Having a second photon included in the PD process changes the nature of the angular distribution and two anisotropy parameter β_2 and β_4 may be needed. Additionally, some other effects like the characteristics of the intermediate state start to play a role. This will be described in the first part of this chapter. After that, two near-resonant 2-photon PD experiments will be discussed. The intermediate state was the $0_u^+(-2,1)$ with a binding energy of 23.9684(50) MHz [19] and the final state was the continuum above the $^3P_1$-$^3P_1$ asymptote. When applying a magnetic field of about 2 Gauss, the energies of the magnetic sublevels $m = -J, ..., 0, ..., J$ of the intermediate state experience a shift of about several hundred kHz due to the Zeeman effect which made it possible to individually access them by detuning the probe laser. Therefore, in the following the notation of the states will include the magnetic sublevels when necessary, e.g., $0_u^+(-2,1,m')$ or $X(-1,2,m)$ with $m' = \pm 1, 0$ and $m = \pm 2, \pm 1, 0$.

In the first experiment, PD from the $X(-1,0,0)$ ground state, which only has a $m = 0$ sublevel was performed. In order to obtain only a signal from 2-photon PD via the $m' = 0$ sublevel of $0_u^+(-2,1,m')$ intermediate state and to have no influence of other sublevels, we polarized the lattice and the probe vertically, thus parallel to the applied magnetic field. By that, we drove only π-transitions with $\Delta m = 0$ (see Chap. 2). The goal was to investigate the angular distribution for PD with frequencies higher than the $^3P_1$-$^3P_1$ asymptote measuring the anisotropy parameters. For low frequencies,

a perpendicular pattern can be detected which transforms to be parallel for higher frequencies. Compared to the 1-photon PD to the $^1S_0$-$^3P_1$ manifold in Chap. 5, the main difference was that the transition region showed a clover leaf pattern instead of a continuous circle. A clover leaf patter can only occur in PD with at least two photons involved. As for 1-photon PD, the change of the angular distribution provides information about the structure of the final manifold. While analysis was relatively simple for the $^1S_0$-$^3P_1$ manifold, the $^3P_1$-$^3P_1$ manifold is very complex. In [56], the dimer Hg_2 is described to have 6 potentials. This we can also assume for Sr_2, since the structure is similar and they both have two valence electrons. We want to study this manifold, since it is not very well understood yet. A more thorough theoretical model would significantly help the work started with this thesis.

Starting from the initial states $X(-1, 2, m)$ with $m = 0, \pm 1$ in the second experiment enabled us to approach the three magnetic sublevels of the intermediate state $0_u^+(-2, 1, m')$ with $m' = 0, \pm 1$ when we again only drive π-transitions. This made it possible to chose each sublevel in the intermediate individually when photodissociating. Different angular distribution pattern were detected for $m = \pm 1$ and $m = 0$. This process is highly complex and an exhaustive explanation is hard to provide yet, but it is possible to say that the experiment proves that the initial angular momentum is reflected in the final photofragment distribution. Further work on this will be necessary. Nevertheless, we give proof-of-concept that it is possible to perform PD via magnetic sublevels of the intermediate state in a controlled way.

6.1 Theoretical Background

The formula to describe the angular distribution of a 2-photon PD when the axial recoil approximation holds and cylindrical symmetry can be assumed is similar to the one for 1-photon PD and is well known from literature [57, 58]. Since one more photon contributes to the process, not only the second order but also the fourth order Legendre polynomial plays a role. The 1-photon PD formula 5.1 is extended and becomes

$$I(\theta)_{2ph} = I_0(1 + \beta_2 P_2(cos\theta) + \beta_4 P_4(cos\theta)). \tag{6.1}$$

where I_0 is a coefficient, P_2 and P_4 are the 2nd and 4th order Legendre polynomials, shortened for reading convenience, with their corresponding anisotropy parameters β_2 and β_4. In the experiment, $I(\theta)_{2ph}$ depends on the angular distribution $A(\theta)$, which is the measured density of Strontium atoms at the angle θ. Tab. 6.1 gives an overview of the resulting distributions for the possible consecutively transitions of parallel ($\|$)

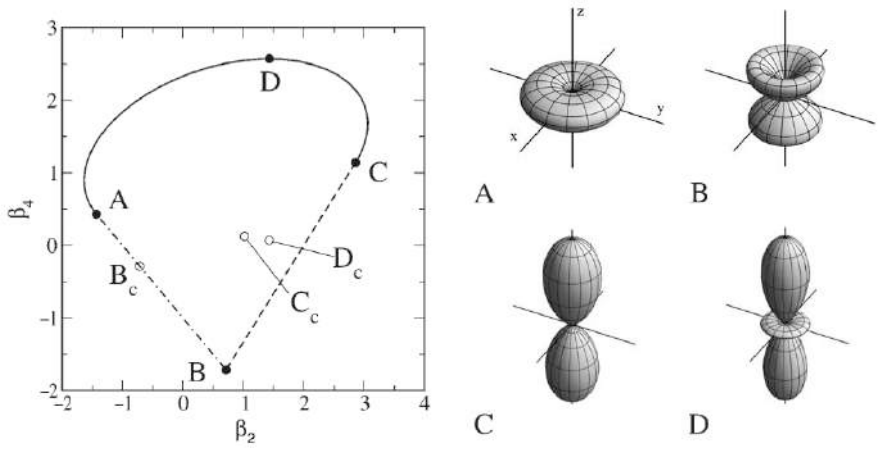

Figure 6.1: The area of possible combinations of β_2 and β_4 on the left side. Labels A-D refer to the shape of the orbitals depicted on the right side, labels B_c-D_c to points explained in [59], were plot and orbitals are from. Note that the plot was edited and that the abscissa was corrected to be β_2.

and perpendicular ($\perp$) when the axial recoil approximation holds and a dominating intermediate state is expected [49].

Type of consecutively transitions	$I(\theta)_{2ph}/I_0$
$(\parallel, \parallel)$	$\cos^4\theta$
$(\parallel, \perp)$	$\cos^2\theta \sin^2\theta$
$(\perp, \parallel)$	$\cos^2\theta \sin^2\theta$
$(\perp, \perp)$	$\cos^4\theta$

Table 6.1: Types of possible consecutively transitions and the resulting angular distributions assuming axial recoil approximation and a dominating intermediate state.

Since the intensity can never be negative, well documents limits for β_2 and β_4 apply [59]. The possible values for the two parameters are restricted, by definition, to the area in the plot on the left of Fig. 6.1. The right side of Fig. 6.1 shows the angular distribution at the indicated points A-D. In [56], 4 even (g) and 2 odd (u) potentials in the $^3P_1$-$^3P_1$ manifold are stated. Hence, mixing of several dissociation channels can be expected.

Eq. 6.1 and Tab. 6.1 are valid when the time the molecule is in the intermediate state is short in comparison to the rotation of the intermediate state [60–62]. We will assume an immediate absorption of the second photon takes place here. This might not always be exactly the case and a deeper insight into the topic will be required in order to analyze the more quantitatively.

In previous measurements, PD has been used to measure the rovibrational wave functions [63, 64]. Theoretically, this would also be possible with our setup. We could 2-photon PD to a dominant repulsive potential in the continuum above the $^3P_1$-$^3P_1$

and perform a rovibrational wave function measurement of potentials in the intermediate $^1S_0$-$^3P_1$ manifold, This implies that multiple channels would be accessed at the same time. We would expect to detect two main rings separated by their distinguishable angular distributions, while each ring consists of several sub-rings depending on the number of nodes of the wavefunction. However, the restrictions in our setup like optical resolution and background noise would make this measurement very difficult and maybe not feasible.

6.2 Investigation of $^3P_1$-$^3P_1$ Continuum with Transitions from X$(-1, 0)$ Ground State

Description of Measurement

A scheme with the relevant transitions as well as an example image with the signals is given in Fig. 6.2. To conduct the 2-photon transition we were interested in, the first probe laser excited molecules from the X$(-1, 0, 0)$ state to the $0_u^+(-2, 1, 0)$ intermediate state which has a binding energy of about 24 MHz using only π-transitions (dark red probe 1 arrow). The second probe laser subsequently dissociated the molecules to the $^3P_1$-$^3P_1$ (dark blue probe 2 arrow). The signal is represented by ring (A). To take various data points the frequency of probe 2 was detuned. Due to the frequencies of the two lasers, several incidental signals emerged. Three excitation paths resulted in additional rings in the image. Signal (B), originating from 1-photon PD of the X$(-1, 2)$ state, is already well know to the reader of this thesis since it occurred in both of the 1-photon experiments (light red probe 1 arrow). A 2-photon PD from the X$(-1, 0)$ state to the $^3P_1$-$^3P_1$ shelf caused signal (C) (two consecutive light red probe 1 arrows). Additionally, probe 2 created a fourth ring (D) from the PD of X$(-1, 2)$ molecules, which appeared once the laser was detuned to higher frequencies (light blue probe 2 arrow). This was the case when the atoms of the signal of interest had an energy corresponding to 42.4 MHz. In order to verify this complicated structure, it is possible to compare the radii obtained with the PES data of pBasexL with the expected radii calculated using the applied frequencies.

As clearly noticeable in the processed image, it is difficult to distinguish between the signals. Fortunately, it was possible to utilize a little variation of the imaging process to remove the X$(-1, 2)$ ring, which facilitated the analysis significantly. Usually, when we process the images as described in Chap. 7, an averaged background image is subtracted from an averaged image with signal to increase the signal-to-noise ratio. Here, instead of subtracting a background image without any signal, we subtracted an image containing only signal (B) from the X$(-1, 2)$ state and signal (C) from the

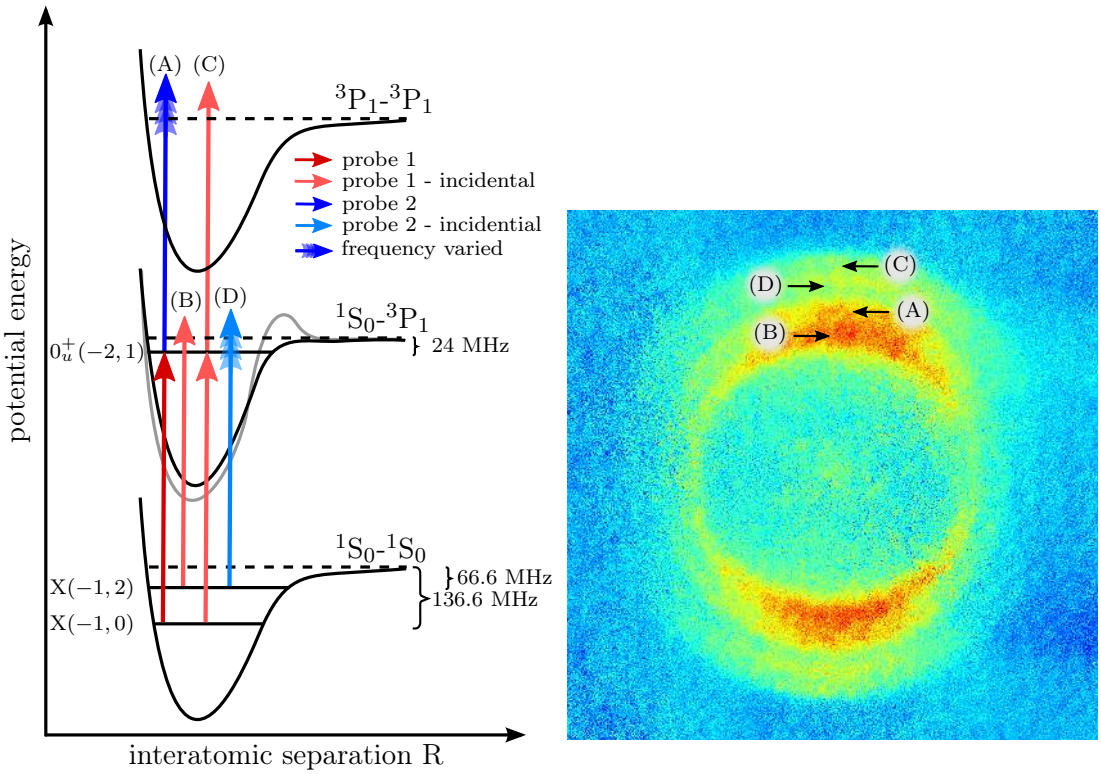

Figure 6.2: Signal (A) is caused by a combination of probe 1 and 2 performing 2-photon PD from $X(-1,0)$ to the $^3P_1$-$^3P_1$ shelf. Probe 1 creates the incidental signals (B) by 1-photon PD from $X(-1,2)$ and (C) by 2-photon PD from $X(-1,0)$ at a fixed frequency. Signal (D) is the result from probe 2 and changes radius as the signal of interest (A) does.

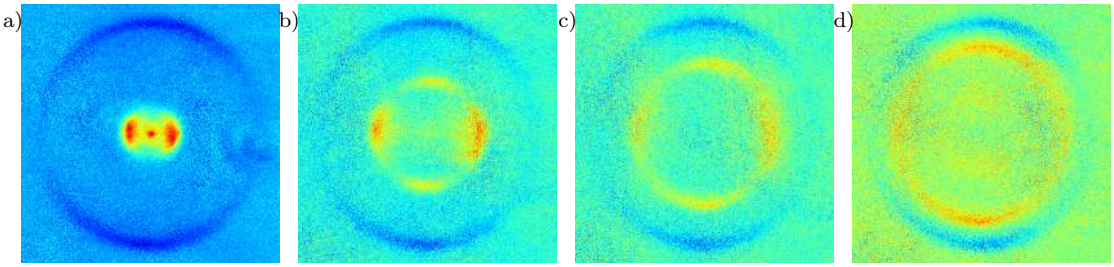

Figure 6.3: Images a)-d) show the processed images with false color with a frequency detuning of 5 MHz, 21 MHz, 37 MHz and 55 MHz above the $^3P_1$-$^3P_1$ asymptote. Performing background subtraction further explained in the text, it was possible to be left with only one incidental signal of the outer ring, here blue, and the signal of interest. A change of the angular distribution from perpendicular to a parallel via a clover leaf pattern can be seen. In d), some of the signal (D) becomes visible in the center.

2-photon PD caused by probe 1. This enabled us to remove signal (B) completely and decrease signal (C). It was conducted by detuning probe 2 to a completely off resonance frequency, so no signals (A) and (D) were created. It is important to notice, that the frequency of probe 1 was not changed, hence the intensity of the signal from $X(-1, 2)$ remained the same. As a consequence, subtracting this image from the image with all the rings fully eliminated the $X(-1, 2)$ signal (B). The difference can be seen when comparing the image on the right of Fig. 6.2 and the images in Fig. 6.3, especially image (d). Unfortunately, it was not possible to get rid the 2-photon PD signal of probe 1 that straightforward. When we detuned probe 2, we interrupted its PD from the intermediate state. Without this excitation, more population was available for the PD of the second leg of probe 1. This resulted in a stronger signal (C) and when we then subtracted the images, the final image showed an dark ring as signal (C) (as can be seen in Fig. 6.3). Subtracting an image with higher intensity at this location than in the initial image causes low values and hence a blue color in the false color image here. Nevertheless, this alternation improved the image enough to make analysis feasible. In this experiment, we took data for frequencies from about 3 MHz - 55 MHz detuning above the $^3P_1$-$^3P_1$ asymptote in steps of 2 MHz. The four example images in Fig. 6.3 show the results for a detuning of 5 MHz, 21 MHz, 37 MHz and 55 MHz into the shelf. We evaluated the images with pBasexL to obtain the β parameters. Since this was a 2-photon process, we used Eq. 6.1 to describe the distribution. Data for a higher frequency detuning than 55 MHz was not trivial to obtain, since for such frequencies the signal of the 2-photon $X(-1, 0) \rightarrow {}^1S_0$-$^3P_1$, which was not deductible, and the additional signal (D) from probe 2 were too close to the relevant signal. We took two more data points at higher detuning at about 87 MHz and about 110 MHz to determine the tendency. As in the other experiments already described, a trace of the $^3P_1$-$^3P_1$ shelf was taken to relate the frequencies to a known frequency of an asymptote.

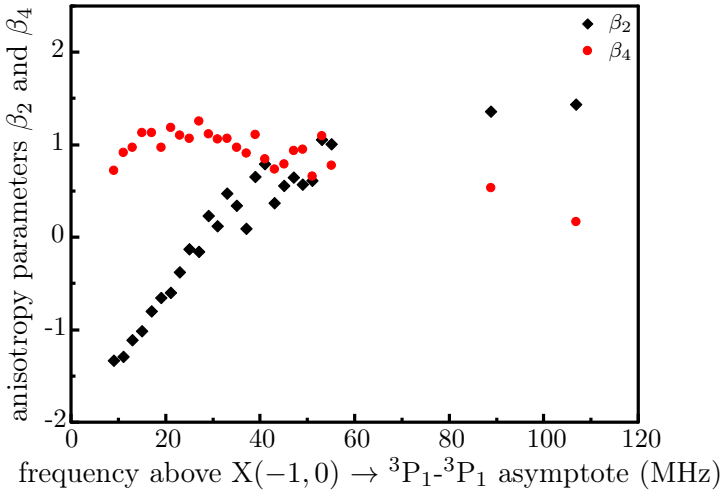

Figure 6.4: Anisotropy parameters β_2 and β_4 depending on the frequency above the $^3P_1$-$^3P_1$ asymptote. The change of β_2 from below -1 to 2 is caused by alternating contributions of the transitions to the various potentials of the $^3P_1$-$^3P_1$ manifold accessed in this measurement. β_4 expresses the convolution with an additional component resulting from the 2-photon case.

Results & Discussion

In contrast to the angular distribution of the 1-photon PD from the $X(-1,0)$ ground state, having a full circle in the crossover phase from parallel to perpendicular, here the shape of a clover leaf could be observed. This is due to the dynamics of 2-photon dissociation with the possible transitions $(\parallel,\parallel)$, $(\parallel,\perp)$, $(\perp,\parallel)$ and $(\perp,\perp)$ previously described in Tab. 6.1. The results for β_2 and β_4 are plotted in Fig. 6.4.

For a better intuitive understanding of the result, Fig. 6.5 illustrates the change of the two β parameters with increasing frequency detuning in a 3D plot. The two parameters can be in the light blue area, determined in [59] and also presented in Fig. 6.1. Additionally, the 3D angular distributions at the points A-D are illustrated. The first transition from the initial $X(-1,0)$ state to the intermediate $0_u^+(-2,1)$ state is parallel. In Fig. 6.5 one clearly can see a change of the angular distribution from a $\sin^2\cos^2$ distribution to a $\cos^4$ distribution. Therefore, following Tab. 6.1, the second transition is first mostly perpendicular and then changes to be parallel. With an E1 dipole transition, only the 4 *gerade* potentials of the $^3P_1$-$^3P_1$ manifold can be reached. Those are two 0_g^+, a 1_g and a 2_g states [56]. The change from perpendicular to parallel indicates, that we see a change in dominance of the dissociation channels, similar to the effect already discussed in Chap. **??**. This and the further change in convolution of angular pattern like illustrated at point D are rather complex and further theoretical models to support understanding the processes would significantly help, although are not available yet. By performing this experiment, we showed that it is possible to obtain information about potentials of the $^3P_1$-$^3P_1$ manifold.

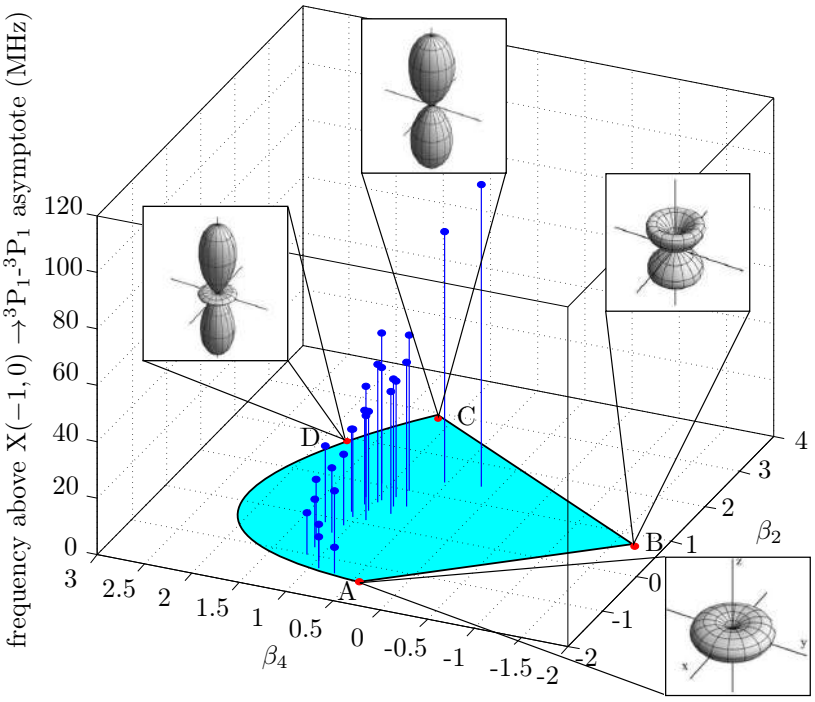

Figure 6.5: Plot of the results for β_2 and β_4 depending on the frequency above the $^3P_1$-$^3P_1$ asymptote. This is a combination of the information in Figs. 6.1 and 6.4. The area in light blue represents the possible values for β_2 and β_4. The shape of the orbitals at the points A-D are illustrated. Orbitals from [59].

6.3 Investigation of $^3\mathrm{P}_1$-$^3\mathrm{P}_1$ Continuum with Transitions from $\mathrm{X}(-1,2,m)$ Ground States with $m = 0, \pm 1$

Description of Measurement

With our setup it is possible to access dissociation paths with a chosen set of magnetic sublevels. We addressed the magnetic sublevel by applying a magnetic field of $B \approx 2$G. The intermediate state $0_u^+(-2,1,m')$ then split into its three sublevels $m' = -1, 0, 1$ with an energy difference of a few hundred kHz. Fig. 6.6 shows the transition scheme with magnification of the important states on the right side. In contrast to the transition schemes in the previous chapters, the red and blue PD paths represent two different measurements and were not applied at the same time. In the figure, the measurement from the $\mathrm{X}(-1,2,m)$ states with $m = 0, \pm 1$ is drawn with an dark blue arrow. The dotted arrow on the right indicates, that only one of the transitions is applied a time. Since the different sublevels of the intermediate state had an energy difference, they could be addressed by detuning the probe laser. Again, we only employed π-transitions to have more control and limit the number of involved sublevels to one. The plot above the PD path on the top right illustrates the different detuning applied to approach the sublevels. We took images for the $m = -1$ and $m = 0$ sublevel. The sublevel $m = +1$ has the same distribution as $m = -1$, which we determined in preliminary measurements in the preparation for this one. With the second schemed transition from the $\mathrm{X}(-1,0,0)$ state (dark red arrow) we were able to compare the result to a measurement where only one magnetic sublevel can be addressed with π-transitions. This measurement was equal to the previous 2-photon PD experiment. For simplicity, only the arrow representing the relevant transition for the main signal (A_1) and the main incidental signal (B) are drawn, while the other transitions can be found illustrated above in Fig. 6.2. Decay of the intermediate state caused signal (C).

Results & Discussion

The center image of Fig. 6.6 shows the angular distributions of PD from $\mathrm{X}(-1,2,m)$ with $m = -1$ and the image on the right with $m = 0$. A significant difference in the angular pattern can be detected, so we conclude that the angular distribution depends, besides others, on the initial state of the molecule.

This measurement has the potential for being used for the investigation of the continuum above the $^3\mathrm{P}_1$-$^3\mathrm{P}_1$ asymptote. Furthermore, insights in the influence of the initial, intermediate and final states on the angular distribution can be achieved. Since many variables are involved, careful further measurements and a thorough analysis with

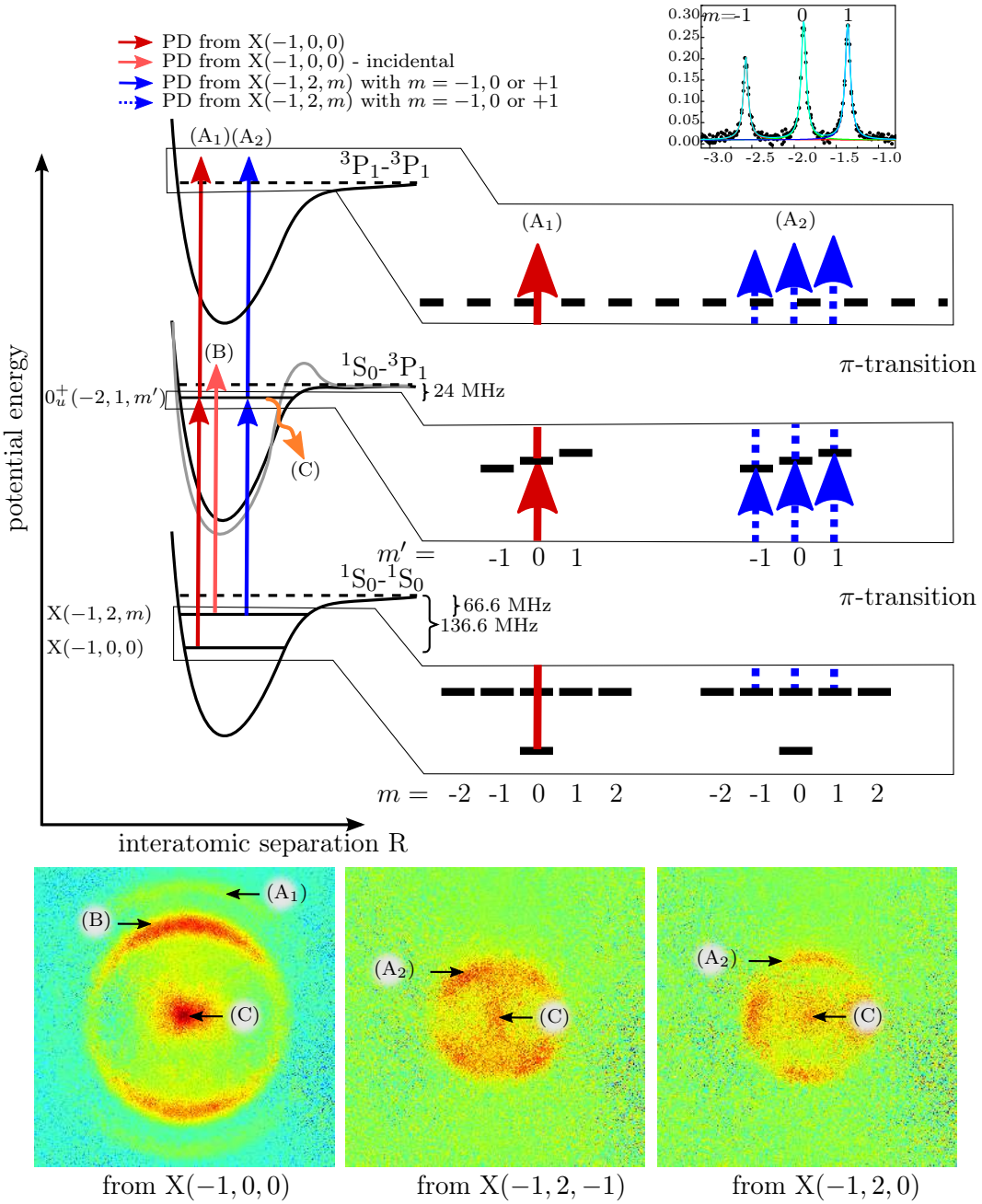

Figure 6.6: Top part: The red and blue arrows represent two different measurements and were not applied at the same time. The blue arrows in the closer view on the right are dotted to clarify, that they are not applied at the same time but PD from X$(-1, 2, m)$ with either $m = -1$, $m = 0$ or $m = +1$is performed. This causes signal (A_2). Signal (A_1) is created with PD from X$(-1, 0)$. (A_1) only has one possible transition path to be created. The three different paths for (A_2) can be controlled applying different frequencies of the PD laser (upper right corner). Bottom part: Resulting processed images. Incidental signals (B) and (C) are caused by the probe laser and by decay of the $0_u^+(-1, 2)$ state.

support of a theoretical model have to be conducted. Comparison with the angular distributions when photodissociating from X$(-1, 0, 0)$ (e.g., on the left of Fig. 6.6) will also help with that.

Chapter 7

Data Processing Details

For data analysis two different approaches were pursued, depending on the experiment. For both methods, offline processing of the images was necessary, carried out by two Matlab programs (ImageProcessor and NormalizeImgsWithBgd). The code for the Matlab programs is provided in App. (A). Then, the prepared images were either evaluated by a software called pBasexL [53] and a Matlab program (GetBetaWithngularSum) for the pBasex inversion method or by another Matlab program (Analyze) and Origin to fit the data and receive β for the horizontal integration method. Having these two independent methods is useful to verify the results.

7.1 Improvement of Image Quality

In the course of each experiment, data points for various probe laser frequencies were taken in order to investigate the energy dependence of the angular distribution. Since the signal is very low in these experiments, an offline processed image had to be created for each data point to increase the signal-to-noise ratio. To do so, a number of images (usually 100) containing information about the optical density of the atoms cloud were taken and averaged. Additionally, after every image, a background image without atoms was recorded. This resulted in a total of 100+100 images. For each of these 200 images, the camera took two shots which will, from now on, be referred to as 'raw image with atoms' $I_{raw,a}$ and 'raw background image' $I_{raw,b}$. With these two raw images, the image showing the optical density could be calculated applying the absorption imaging technique discussed in Chap. 3. Then, the 100 averaged background images were subtracted from the 100 images with atoms. In the course of this thesis this is named absorption/subtraction technique. The process of improving the data quality is pictured in Fig. 7.1 and is now explained in more detail.

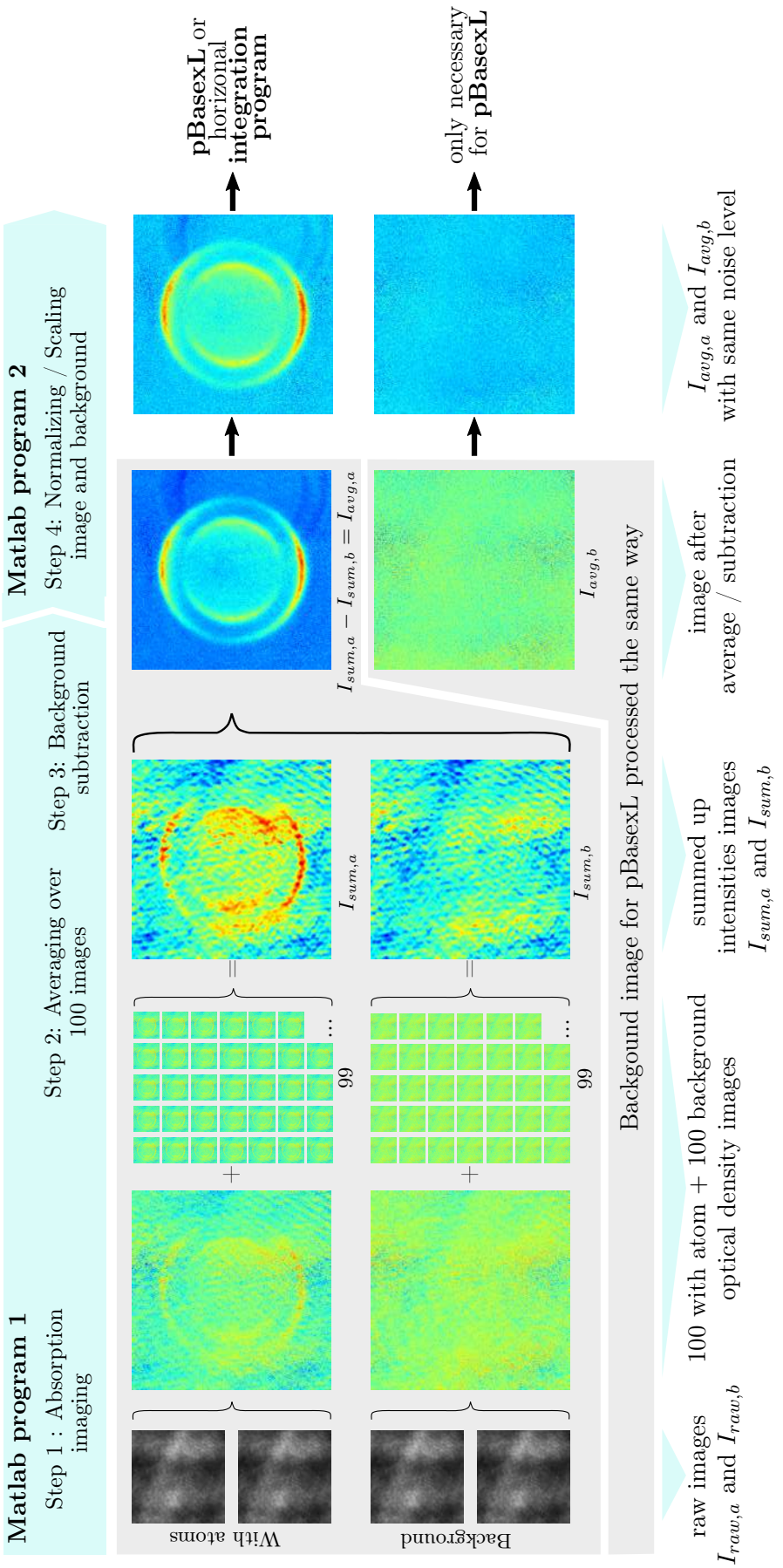

Figure 7.1: Please view sideways. Process to increase signal-to-noise ratio. We start with raw images (left) and receive averaged and background subtracted images (right). For further details of the steps refer to text.

Step 1 A first raw image $I_{raw,a}$ is taken with atoms in the chamber and a second raw image $I_{raw,b}$ of the background is shot a few μs afterwards. Between the two shots, a powerful pulse of the 461 nm light clears the atoms away. The Matlab program first calculates the optical density for each pixel by applying the Beer-Lambert law $A = \ln \frac{I_{raw,b}}{I_{raw,a}}$. This is calculated for each pixel separately. Taking the natural log results in negative numbers for some pixels. That is, because the light intensity from one to the other image can vary and in regions without signal the second image can be darker than in the first image for some pixels. To output the images as a *.png*-file with data type uint8, the image has to be rescaled to a range from 0 to 255 later.

Step 2 & 3 The resulting image with the optical density is one of 200 images, 100 taken with atoms in the chamber and 100 without. Then averaging/subtraction is applied. The two sets of 100 images are summed up separately to give the atoms image $I_{sum,a}$ and the background image $I_{sum,b}$. In the next step, the summed up background image is subtracted from the summed up atom image $I_{sum,a} - I_{sum,b} = I_{avg,a}$. This way, a significant reduction of static background can be achieved as it visible after Step 3 in Fig. 7.1. To improve the further analysis with pBasexL, another set of 200 images is taken and processed, this time without atoms in any of the images. This results, after processing, in a background image, which is used for analysis with pBasexL. Any background noise in the processed images also causes a background signal in the output images of pBasexL. By applying pBasexL also on the processed background images, it is possible to later subtract that background signal. The program saves the resulting images in the *.m*-file format with each pixel being an entry of a matrix of size $m \times n$, where m is the number of vertical pixels and n the number of horizontal pixels of the image.

Step 4 A second Matlab program imports the *.m*-file of each averaged atoms image $I_{avg,a}$ and averaged background image $I_{avg,b}$ of each data point (each frequency), normalizes and rescales them so that the lowest pixel value of any image is 0 and the highest value 255. This is necessary to meet the requirements of the input files for pBasexL of data type uint8. The two normalized images are saved in the *.png*-file format for further processing. App. A contains the code for 1-photon PD. For 2-photon PD, slight changes in the code were necessary.

7.2 Abel Inversion with pBasexL

In order to receive information about the energy and angular distributions of the dissociation products it is necessary to reconstruct their three dimensional distribution,

also called Newton's sphere, from the two dimensional projection onto the plane of the detector, here the CCD camera. To do so, various techniques have been proposed and used, most of them employing a inverse Abel transformation. A comparison can be found in [65] and [66], another new approach is described in [67]. For this thesis, the pBasex algorithm (polar basis set expansion) of Garcia et al. [68] is used. The advantage of this technique over most others is a fast computation time and the concentration of noise in the center instead of, e.g., in a central line as with the Basex technique. pBasex can always be utilized when the PD process has cylindrical symmetry around the quantization axis. Here, this is the case as already discussed earlier. For the analysis in this thesis, a version called pBasexL is used. The original algorithm of Garcia et al. was ported to a Windows compatible program by Luka Pravica from the University of Western Australia [69] in 2010.

As elaborated in Chap. 5, the angular distribution of an photodissociation process can be described using Legendre polynomials, $P_l(\cos\theta)$. Additionally, pBasexL assumes a Gaussian radial energy distribution $e^{-(x-x_0)^2/\sigma}$. The set of basis functions which describe the original distribution of the photodissociation products then is

$$f_{kl}(R,\theta) = e^{\frac{-(R-R_k)^2}{\sigma}} P_l(\cos\theta) \tag{7.1}$$

with R being the radius, R_k the center of the kth Gaussian, σ the width of the Gaussian function, P_l the Legendre polynomial lth order and θ the angle in respect to the polarization axis of the dissociating electric field, here the probe laser. To now reconstruct the original distribution, which is the center slice of the Newton's sphere, one has to sum over k and l:

$$F(R,\theta) = \sum_{k=0}^{k=k_{max}} \sum_{l=0}^{l=l_{max}} c_{kl} f_{kl}(R,\theta) \tag{7.2}$$

The coefficient c_{kl} has to be determined in order to reconstruct the image. This can be achieved by determining the formula representing the distribution of the 2D camera plane projection. If there exists cylindrical symmetry and the kinetic energy of the particle is neglectable in comparison to the electromagnetic field of the laser, it is possible to apply the Abel transformation [70] and by doing this relate the original distribution $F(R,\theta)$ to the 2D projection $P(R',\theta')$:

$$P(R',\theta') = 2\int_{|x|}^{\infty} \frac{rF(R,\theta)}{\sqrt{r^2-x^2}} dr \tag{7.3}$$

with

$$x = R' \sin\theta'$$
$$r = R \sin\theta$$

Now, it is possible to establish an analog equation for the projection as Eq. 7.2:

$$P(R', \theta') = \sum_k \sum_l c_{kl} g_{kl}(R', \theta') \tag{7.4}$$

where g_{kl} are the basis functions which can be obtained by combining Eqs. 7.1, 7.2 and 7.3:

$$g_{kl}(R', \theta') = 2 \int_{|x|}^{\infty} \frac{r f_{kl}(R, \theta)}{\sqrt{r^2 - x^2}} dr \tag{7.5}$$

Since the projection of the distribution is available in form of the taken images, the basis set $f_{kl}(R, \theta)$ in Eq. 7.2 can be constructed. Knowing l, which depends on the number of photons involved, and k, which is dependent on the dimensions of the image and can be preset, it is possible to obtain the basis set $f_{kl}(R, \theta)$ without knowing the original angular distribution $F(R, \theta)$. Now, $g_{kl}(R', \theta')$ can be computed. In fact, with having $g_{kl}(R', \theta')$, one can now receive the coefficients c_{kl} of Eq. 7.4 which ultimately leads to the original distribution $F(R, \theta)$ via Eq. 7.2. The image of the projected Newton's sphere taken is not continuous but quantized by the pixels. The pBasex algorithm takes this quantization into account and rewrites $P(R', \theta')$ as

$$P_{ij} = \sum_k \sum_l c_{kl} g_{ij,kl}. \tag{7.6}$$

Here i and j are pixels in a polar coordinate system. The algorithm converts the original cartesian coordinate system using reverse transformation and bicubic interpolation. Eq. 7.6 can also be expressed as

$$\mathbf{P} = \mathbf{GC}, \tag{7.7}$$

where $\mathbf{P}$ and $\mathbf{C}$ are vectors with the length $i \times j$ and $\mathbf{G}$ is a matrix with every row contains the dependencies of one pixel (fixed i,j) and every column containing the abel transformation of one of the l basis functions (fixed k,l). $\mathbf{G}$ is computed by numerical integrating Eq. 7.5. To receive $\mathbf{C}$, Eq. 7.7 has to be rearranged to

$$\mathbf{G^{-1}P = C} \tag{7.8}$$

G is inverted using the singular value decomposition method (SVD). Once **G** is calculated, which can take several hours computation time depending on the machine and the order of the Legendre polynomials, it is saved to the hard drive and can always be used for the calculation of **C** for images with the same l_{max} and the same number of applied Gaussians k_{max}. Here it is $l_{max} = 2n$, where n is the number of photons involved in the process. For linearly polarized light, only the even terms of l have to be taken into account. k_{max} is chosen to be 128 in all our analysis. The width of the Gaussian function σ in Eq. 7.5 is with $\sigma = \sqrt{2}$ the width of two pixel.

In order to calculate the slice through the Newton sphere from the *.png* images of the measurement, first, one image was imported into the main program. The center then has to be determined and symmetrization options are selected. The choice of the center and the symmetrization is crucial for the results, since pBasex will divide the image into four quadrants and add them up after mirroring. The stated error in Chap. 5 is inferred by choosing various centers and options of symmetrizations of the image. In order to invert a data set with data taken at many different frequencies, it is helpful to use an additional little program for larger batches also provided by Luca Pravica. The output of pBasexL, when using the batch program, are two *.dat*-files. One contains the PES (potential energy surface) data and preliminary β values for the different radii and one contains the pBasex output image. The larger the radius, the higher the energy of the fragments are, which is the information the PES data contains. The PES data is obtained by integration over a full circle for every radius. With this data, the radii of the signal rings can be determined. Every pixel of the output image is multiplied by R^2, where R is the radius of the pixel in polar coordinates. This R^2 scaling is applied in order to serve as a visual aid, so that rings comprised of the same number of atoms will appear at the same brightness.

7.3 Determination of β-Values

As mentioned earlier, two possibilities of obtaining the β values were employed. One works with the inverted output images of pBasexL, the other handles directly the processed images and horizontally integrated the pixel lines of the image.

pBasex Inversion (On-axis Imaging)

After the calculation of the original distribution images of the dissociation products with pBasexL, another Matlab program evaluates these images to receive the β value. The process is illustrated in Fig. 7.2.

Step 6 & 7 Experiments in this thesis, where the analysis is performed with the pBasex algorithm usually have two signal rings. To determinate for which ring β should be calculated and to determine the center radius of this ring, the PES data in the output file of pBasexL is first divided by R^2 and then plotted. Through calculations using the applied frequencies and the binding energies the signal we are interested in is determined and can be chosen in the program. Gaussians are fitted to the peaks to find the center radius r_c of the signal ring. Additionally, the FWHM is obtained which defines the width of a analysis ring with radius r_c around the center.

Step 8 Further, this ring is divided into 24 sectors of $\Delta\theta = 15°$, starting at $\theta = 0$. As earlier, θ is defined with respect to the direction of the polarization vector of the dissociation laser. The program sums up the intensities of the pixels within each sector and plots the result against θ. This process is applied to both - the image with the atoms and the corresponding background. When applying pBasexL on the background, the output resembles the offset of intensity in each sector due to the background in the pBasexL output with atoms. Hence, subtracting the background intensity of the corresponding sector of the image with atoms decreased the error due to background noise significantly.

Step 9 Using Eq. 5.1, namely $I(\theta) = I_0[1 + \beta P_2(\cos\theta)]$, where $I(\theta)$ is the intensity at a given θ, I_0 a scaling factor and P_2 the second order Legendre polynomial, the data is fitted and finally the value for β can be read out.

A data set contains processed images of various frequencies. For each frequency the β value has to be calculated separately. Eventually, β is plotted against the frequency to illustrate if there is any change of the angular distribution with changing frequency.

Horizontal Integration (Side Imaging)

In order to verify the results we use another method to determine the β-values. The values obtained with this technique only differ slightly from the values received with the on-axis technique and are mostly within the error (see Chap. 5).

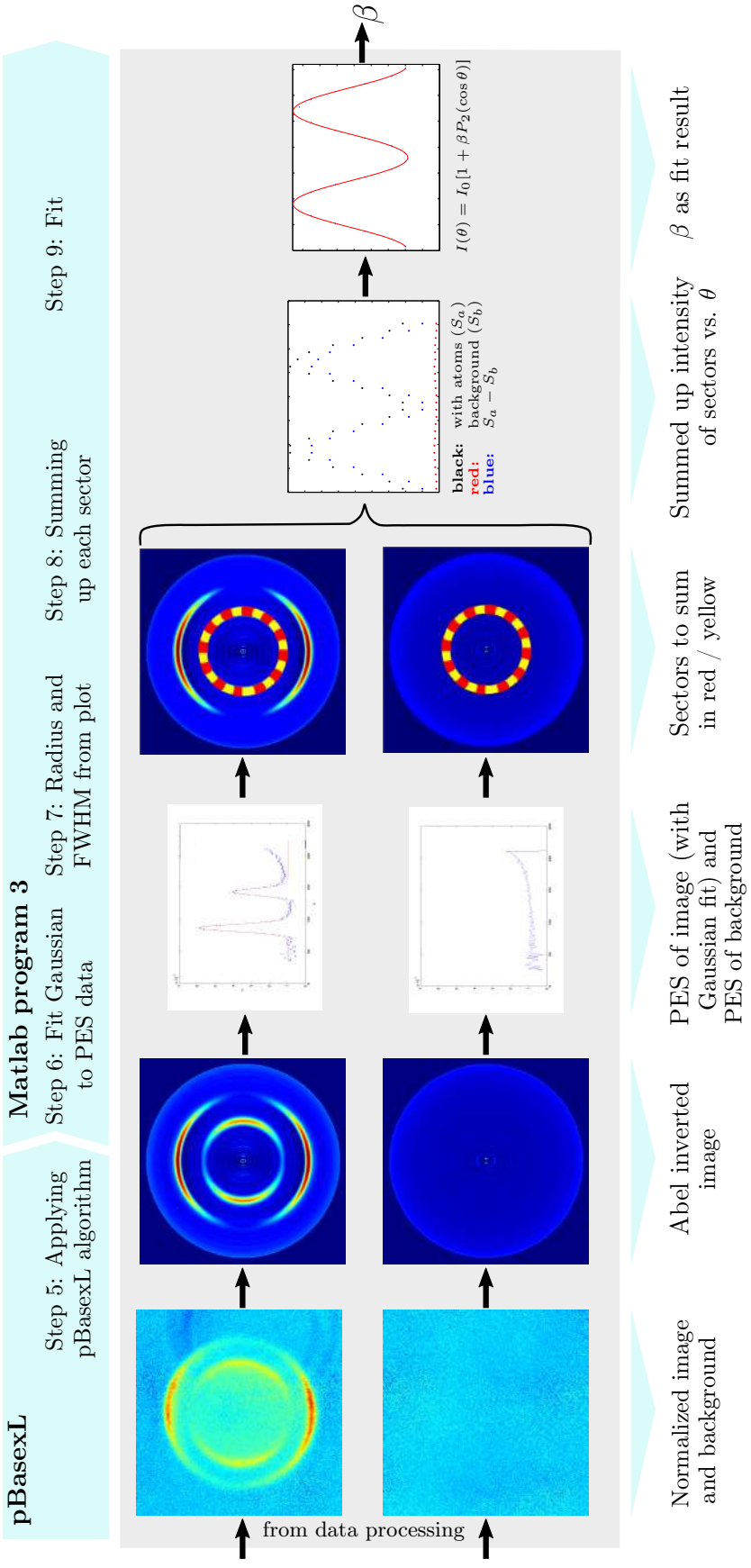

Figure 7.2: Please view sideways. Process to receive β with pBasex inversion method. For details explanation of the steps refer to text.

The pBasex inversion and the horizontal integration methods both rely on the analysis of averaged, background-subtracted images described in Fig. 7.1. While the pBasex inversion method only makes sense with axial imaging, the horizontal integration method can be used with both. Due to imaging artifacts, which more often occur in the on-axis system, the symmetry of the signal can sometimes be off. Therefore, we usually use this method with side imaging which is less sensitive to beam alignment. A Matlab program imports the processed side images, sums up the intensities of the pixels in every line. The output is then fitted in Origin. Fig. 7.3 shows the idea this method is based on. It can be applied to the on-axis and side images so it will here first be explained on the basis of the on-axis imaging and then transferred to the side imaging.

When dissociated with linearly polarized light using a 1-photon process, the angular distribution of the atoms flying apart is cylindrical symmetric. All dissociated atoms flying apart with the same angle θ in respect to the polarization axis of the dissociating photons (z-axis in the previously introduced coordinate system in Chap. 3), are located in one plane of the sphere's shell. This leads to the circle shown red in (a). When projected to the plane of camera, the circle is represented by a line on where the intensity of each pixel is the integration along the axis of view, the x-axis (b). On each image the absorption imaging technique is applied as described before. As a consequence, the intensity of each pixel is proportional to the number of atoms (Image of dissociation cloud in (c)). Hence, summing up over each pixel line of the processed image yields a number relative to the number of atoms with the same angular distribution θ. This can be seen in plot (d) on the example of the red dot which represents the integration over the red line in the plot. As already mentioned, we use the side imaging for the integration method. When doing so, one line in the images taken from the side contains the same information as the integrated signal represented in one pixel of the on-axis image. One pixel in the side imaging is the same as the line we used to integrate over in the on-axis image. Hence, both times the intensities of the same plane parallel to the x- and y-axes are integrated and the two approaches give the same result. (e) shows an example side image and (f) the result when summing up each row of pixels. Despite some minor patterns due to the optics in the beam paths, the plots for on-axis and side imaging contain the same information. Except, the side plot is more symmetric which is superior for the fit later.

So far, the data processing has been described based on images showing two rings (Figs. 7.1, 7.2 and 7.3). These were caused by 1-photon dissociation from the $X(-1,0)$ and $X(-1,2)$ ground states to the $^1S_0$-$^3P_1$ shelf. In the first experiment in Chap. 5 we were not interested in the ring of the $X(-1,2)$ transition. This second ring did not trouble the analysis with the pBasex algorithm, but in the integration method a fit would be

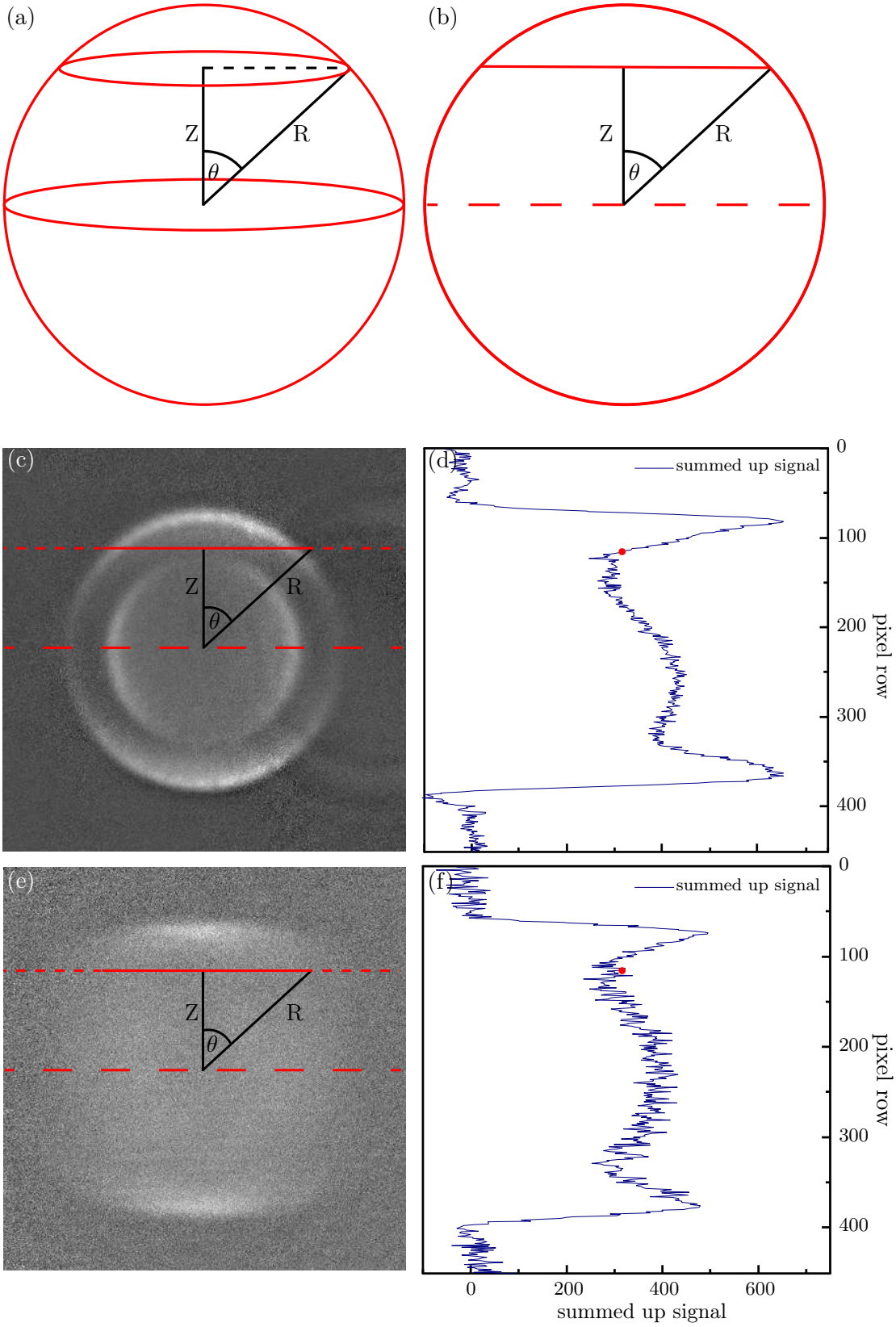

Figure 7.3: (a) Newton's sphere after PD. Atoms located on the red ring fly apart with same angle θ. (b) 2D projection on camera screen. Ring appears as a line. (c) Image from axial camera. Atoms on solid line have same θ. (d) Sum over each pixel line. Red line represented with red dot. (e) Same possible with side camera. (f) More symmetry in signal since side imaging less sensitive to beam alignment.

more accurate if there was no interfering second ring. Fortunately, it is possible to deplete this ring. This was done in the 1-photon experiment where the data analysis was also performed with the integration method.

The advantage of a signal with only one ring is shown in Fig. 7.4. The background of the outer ring in (b) could be completely removed and only the signal of interest remained present (d). By fitting, it is possible to obtain the anisotropy parameter β. The fit function can be derived with the following approach. As just described, the 1D signal is by integration of the planes

$$S(z) = \iint n(x, y, z)\mathrm{d}x\mathrm{d}y \tag{7.9}$$

where n can be described as an product of radial and angular distribution,

$$n(x, y, z) = R(x, y, z)A(x, y, z). \tag{7.10}$$

As derived earlier, the angular distribution is described by $A \propto 1 + \beta[3\cos^2(\theta) - 1]/2$, whereas here $\cos\theta = (z - z_0)/R$ with $(z - z_0)$ being the distance on the z axis of the ring from the center, previously in Fig. 7.3 labeled Z. One then obtains

$$S(z) = \frac{N_{tot}}{2R} \times \begin{cases} 1 + \beta[3(z - z_0)^2/R_0^2 - 1]/2 & \text{for} (z - z_0)^2 \leq R_0^2 \\ 0 & \text{for} (z - z_0)^2 > R_0^2. \end{cases} \tag{7.11}$$

Here, $S(z)$ is normalized so $\int S(z)\mathrm{d}z = N_{tot}$. Different to the Gaussian radial energy distribution assumed in pBasexL, here we use a slightly different approach. We assume the radial distribution as a delta function with the distance R from the center (x_0, y_0, z_0). This is convolved with a Gaussian weight $G(\delta, \sigma) = e^{-\delta^2/(2\sigma^2)}/\sqrt{2\pi\sigma^2}$ due to optical resolution blurring of the image. When looking at the 1D signal of atoms trapped in the lattice (Fig. 7.5), which should be a point source when the width of the lattice is smaller than the optical resolution, the signal has a Gaussian distribution. Hence, we think that there is a significant effect from the limitation in optical resolution which dominates over the effect of the radial distribution of the atoms. When convolving the signal with the Gaussian weight, we receive the fit function

$$S'(z, \sigma) = \int G(\delta, \sigma)S(z + \delta)\mathrm{d}\delta. \tag{7.12}$$

The two approaches, the Gaussian radial distribution on the one hand and the delta function type radial distribution with a Gaussian weight due to optical resolution limi-

tation on the other, are mathematically different but yield very similar results. Furthermore, the blurring from a not infinitesimal probe laser ($10 - 20\mu$s) is small compared to the time we let the rings expand ($450 - 800\mu$s) and thus is neglected here.

The parameters σ and z_0 can be determined first using a Gaussian fit on the 1D signal of the lattice shown in Fig. 7.5, which leaves only R and β as free parameter. Notice, that it is easier to construct a fit, if the signal of only one ring is present.

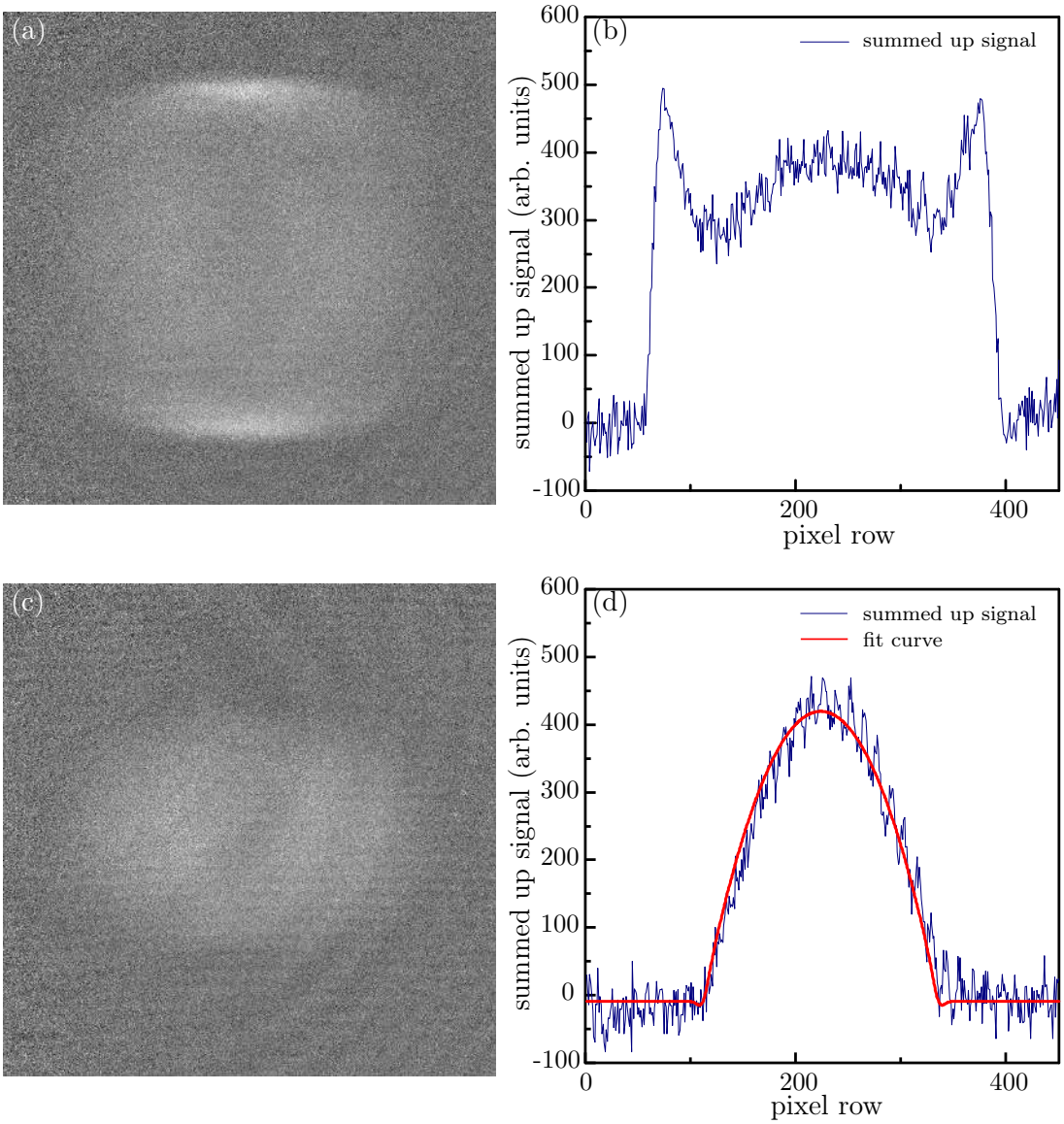

Figure 7.4: Side image of PD (a) without and (c) with pump laser to remove signal of second ring. The advantage is visible in (b) vs. (d). The analysis is significantly improved without the additional signal.

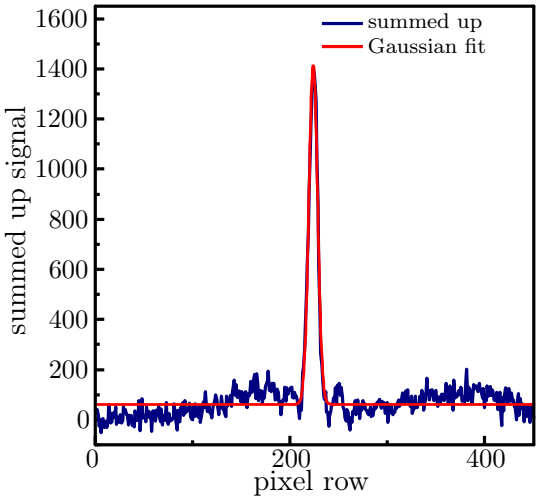

Figure 7.5: Plot of the summed up signal of the lattice without PD of an image from the side. The lattice should be a point source. However, the signal has a Gaussian distribution, which we expect to result from the limited optical resolution. This blurring is included in the fit function of the horizontal integration technique.

Chapter 8

Conclusion

This thesis illustrates the successful photodissociation (PD) of molecules at ultracold temperatures in an optical lattice and demonstrates the advantages of this technique. The complete control over the quantum numbers and the ability to photodissociate so close to the threshold with a high resolution is new. This sets the base for further experiments, which are currently pursued, but is also supposed to act as an inspiration for other research groups.

In this work, we discussed the influence of the lattice on the PD dynamics and presented a way to measure the lattice trap depth using PD. To demonstrate the possibility of the technique to probe the structure of potentials just above the dissociation threshold, a preliminary measurement of the potential barrier height of the $(1)1_u$ potential was performed. This concludes the first step to obtain final results for the lattice trap depth and the potential barrier. The control over the quantum states enabled us to conduct a measurement, where only M1 and E2 PD transitions were allowed and no E1 occurred. This is perhaps the first controlled E2 PD ever. In order to predict angular distributions and pursue further measurements, the knowledge of the transition strengths and expected anisotropy parameters will be important. The two conducted 2-photon PD measurements serve as a proof-of-concept of the possibility to investigate the unbound states and the shape of the potentials of even higher excited manifolds. In one of the measurements, we accessed the magnetic sublevels. Especially, the effect of the initial and the intermediate levels on the dynamics of the PD could lead to promising results in the future. Besides the measurements, the main part of the work for this thesis includes the installation of the new imaging setup and the development of the data processing. To further elaborate the experiments initiated by this thesis, more theoretical work and careful measurements will be required. All these opportunities and more are currently being pursued by the research group. Hereby, high attention is payed particularly to the M1/E2 experiment.

Based on the promising possibilities shown, we expect this technique to be also applicable to other experimental systems working with ultracold molecules and an optical lattice. Possible applications can be detecting molecules, measuring the precise binding energies, probing molecular interactions just above the dissociation, possible production of ultracold fragments (for example for the BaH experiment of our research group) and more.

Appendices

Appendix A

Matlab Code

A.1 ImageProcessor

```
function [] = ImageProcessorF(dirNameRaw, dirNameCorrect, No)
%%%%%% ImageProcessor final version %%%%%%%

%%%% dirNameRaw:        directory where raw images are stored, ...
    ususually called
%%%%                    "Raw"
%%%% dirNameCorrect:    directory where images for amplitude ...
    correction are
%%%%                    stored, usually called "Correction"
%%%% No:                Number of measurement/Name/Frequency ...
    detuning, the
%%%%                    output files will start with whatever is
%%%%                    written here, usually Date_frequency ...
    detuning_other
%%%%                    imformation required(e.g. which measurement, ...
    if background etc.)
%%%%
%%%% ImageProcessorV12 reads the raw images and creates a not normalized
%%%% image in the file format .m which then can be read in with the ...
    program
%%%% "normalizeImgsWithBgd.m" in order to scale it to the background ...
    (which
%%%% is necessary for pBasexL). It also creates .png s of the processed
%%%% image in b/w and color

%%%% First, the program reads in the raw and correction image, ...
    calculates
```

```
%%%% the optical density and multipies it by the correction factor. ...
    It then
%%%% adds up all images with atoms and all images without atoms ...
    seperately and then
%%%% substract the images without atoms (background) from the images ...
    with
%%%% atoms. Finally it saves the image as a matrix in a .m file and ...
    shows a
%%%% scaled version on the screen.

dirDataRaw = dir(dirNameRaw);                          % Get the data ...
    for the current directory
dirIndexRaw = [dirDataRaw.isdir];                      % Find the ...
    index for directories to exclude them from the file list
fileListRaw = {dirDataRaw(~dirIndexRaw).name};


dirDataCorrect = dir(dirNameCorrect);                        % Get ...
    the data for the current directory
dirIndexCorrect = [dirDataCorrect.isdir];                    % Find ...
    the index for directories to exclude them from the file list
fileListCorrect = {dirDataCorrect(~dirIndexCorrect).name};

% show length of both lists, necessary for problem solving when ...
    there are
% not the same since the program will not run then
length(fileListRaw)
length(fileListCorrect)

if length(fileListRaw) == length(fileListCorrect)
    % setting size of image matrix, if this size changed or was not ...
        right
    % in the first place, the matrix size has to be adjusted. The ...
        supposed
    % to be size will be shown as SIZE above the error message in ...
        the Matlab
    % Command Window
    imgAbsorptionSumWO = zeros(450,450);
    imgAbsorptionSumW = zeros(450,450);
    i=1;
    z=1;
    while i < length(fileListRaw)
        % read in images as matrix
        fileImgAtomsRaw = fileListRaw(1,i);
        fileImgBeamRaw = fileListRaw(1,i+1);
        fileImgAtomsCorrect = fileListCorrect(1,i);
        fileImgBeamCorrect = fileListCorrect(1,i+1);

```

```
56          imgAtoms = getImage(fileImgAtomsRaw,dirNameRaw);
57          imgBeam = getImage(fileImgBeamRaw, dirNameRaw);
58          imgAtomsCorrect = getImage(fileImgAtomsCorrect,dirNameCorrect);
59          imgBeamCorrect = getImage(fileImgBeamCorrect, dirNameCorrect);
60          SIZE=size(imgAtoms)
61
62          % Every first image is a background image ...
                (imgAbsorptionSumWO, WO stands for "with out"), every ...
                second a image
63          % with atoms (imgAbsorptionSumW, W stands for "with")
64          if mod(z,2)
65              correctFact = correctAmplitude(imgAtomsCorrect, ...
                    imgBeamCorrect);
66              imgBeam = imgBeam * correctFact;
67              imgAbsorption = log(imgBeam ./ imgAtoms);
68              imgAbsorptionSumWO = imgAbsorptionSumWO + imgAbsorption;
69          else
70              correctFact = correctAmplitude(imgAtomsCorrect, ...
                    imgBeamCorrect);
71              imgBeam = imgBeam * correctFact;
72              imgAbsorption = log(imgBeam ./ imgAtoms);
73              imgAbsorptionSumW = imgAbsorptionSumW + imgAbsorption;
74          end
75          % z makes sure background and with atoms images are processed
76          % in the right order, i makes sure the right pairs of 3 of ...
                the raw images
77          % are read in
78          z = z+1;
79          i = i+(3);
80      end
81      % substraction image with atoms - background image
82      imgAbsorptionSub = imgAbsorptionSumW - imgAbsorptionSumWO;
83      % scaling to show in Matlab window
84      imgAbsorptionSubOut = (imgAbsorptionSub - ...
            min(imgAbsorptionSub(:))) / range(imgAbsorptionSub(:));
85      % saving in .m file
86      dlmwrite([No,'_notNormalized.m'],imgAbsorptionSub)
87      % show b/w and color images
88      figure(1)
89      imshow(imgAbsorptionSubOut)
90      figure(2)
91      imshow(imgAbsorptionSubOut)
92      colormap jet
93      % save b/w and color images
94      imwrite(imgAbsorptionSubOut,[No,'.png'],'png')
95      imwrite(imgAbsorptionSubOut*255,jet,[No,'_color.png'],'png')
96
```

```
97      % pops out normalied matrices of image and background seperately ...
            for debugging if necessary
98      imgAbsorptionSumWOut = (imgAbsorptionSumW - ...
            min(imgAbsorptionSumW(:))) / range(imgAbsorptionSumW(:));
99      imgAbsorptionSumWOOut = (imgAbsorptionSumWO - ...
            min(imgAbsorptionSumWO(:))) / range(imgAbsorptionSumWO(:));
100
101 else
102     fprintf('\n Raw and Correction file lists do not have same ...
            length!\n')
103 end
104 end
105
106
107 %% included functions: getImage, correctAmplitude
108
109
110 function [image] = getImage(filename,dirName)
111 %% This function imports the image
112
113     path = strcat(dirName,'/',filename);
114     path = path{1,1};
115     image = importdata(path);
116     image = rgb2gray(image);
117     image = double(image);
118 end
119
120 function [correctFact] = correctAmplitude(imgAtomsCorrect, ...
        imgBeamCorrect)
121 %% Correction of Amplitude
122
123 % This program is used prevent variations of the amplitude from ...
        image to
124 % image
125
126 imgAtomsCorrect = imgAtomsCorrect(:);
127 imgBeamCorrect = imgBeamCorrect(:);
128
129 imgAtomsCorrectSum = 0;
130 imgBeamCorrectSum = 0;
131 i = 1;
132 while i <= length(imgAtomsCorrect)
133     imgAtomsCorrectSum = imgAtomsCorrectSum + imgAtomsCorrect(i);
134     imgBeamCorrectSum = imgBeamCorrectSum + imgBeamCorrect(i);
135
136     i = i+1;
137 end
138 correctFact = imgAtomsCorrectSum / imgBeamCorrectSum;
```

```
139 end
```

A.2 NormalizeImgsWithBgd

```
1  function [] = NormalizeImgsWithBgdF( dirName, dirName_Bgd )
2  %%%%%% NormalizeImgWithBgd final version %%%%%%%
3
4  %%%% dirName:        directory where images to normalize to ...
       background are
5  %%%% dirName_Bgd:    directory where the one background image is
6  %%%%
7  %%%% NormalizeImgsWithBgdF reads scales the image and the background ...
       image
8  %%%% so that the minimum and maximum value of any pixel of both ...
       images are
9  %%%% 0 and 255. This is necessary for the additonal background ...
       subtraction
10 %%%% after pBasexL. The normalized .png-files are output in the folders
11 %%%% 'img and background normalized' (for pBasexL) and 'img and ...
       background
12 %%%% normalized_color' (false color, not to use in pBasexL and just for
13 %%%% better control)
14
15 dirData = dir(dirName);                        % Get the data for the ...
       current directory
16 dirIndex = [dirData.isdir];                     % Find the index for ...
       directories to exclude them from the file list
17 fileList = {dirData(~dirIndex).name};
18
19 bgd = importdata([dirName_Bgd,'/','background_img_notNormalized.m']);
20
21 k=1;
22 for i = 1:length(fileList)
23     split = regexp(fileList(i),'_','split');
24     split = split{1,1};
25     path = strcat(dirName,'/',fileList(i));
26     path = path{1,1};
27     img = importdata(path);
28
29     ma = max([img(:);bgd(:)])
30     mi = min([img(:);bgd(:)])
31
32     img_ = (img-mi)./(-mi+ma);
33     bgd_ = (bgd-mi)./(-mi+ma);
34
```

```
35      figure(1)
36      imshow(bgd_)
37      colormap jet
38      figure(2)
39      imshow(img_)
40      colormap jet
41
42      if ~exist('img and background normalized','dir')
43          mkdir('img and background normalized');
44      end
45
46      if ~exist('img and background normalized_color','dir')
47          mkdir('img and background normalized_color');
48      end
49
50
51      imwrite(img_,['img and background ...
            normalized/',split{1,1},'_i.png'],'png')
52      imwrite(bgd_,['img and background ...
            normalized/',split{1,1},'_b.png'],'png')
53
54      imwrite(img_*255,jet,['img and background ...
            normalized_color/',split{1,1},'_i_c.png'],'png')
55      imwrite(bgd_*255,jet,['img and background ...
            normalized_color/',split{1,1},'_b_c.png'],'png')
56
57  end
58
59  end
```

A.3 GetBetaWithAngularSum

```
1   function [betaVsFreq] = GetBetaWithAngularSumF(dirName, x0, y0, ...
        stepsize)
2
3   %%%%%% GetBetaWithAngularSum final version (based on V4) %%%%%%%
4
5   %%%% dirNameRaw:        directory where .dat-files of image ...
        (..._i_....dat) and
6   %%%%                    background (..._b_....dat) of each frequency ...
        are located
7   %%%% x0, y0:            coordinates of the center. Always check if ...
        it is really the
8   %%%%                    center (you can see that once the sectors ...
        are drawn in the image. When
```

```
%%%%                    applying an angle in pBasexL, center can ...
    change drastically from
%%%%                    setting in pBasexL
%%%% stepsize:          angle of sector which is summed up to one ...
    point for
%%%%                    the fit. usually it is 15 (degree)
%%%%
%%%% GetBetaWithAngularSum reads the PES and image files from image and
%%%% background and outputs the beta values. This is for 1-photon PD.


%%% get and prepare data
dirData = dir(dirName);                      % Get the data for the ...
    current directory
dirIndex = [dirData.isdir];                    % Find the index for ...
    directories to exclude them from the file list
fileList = {dirData(~dirIndex).name};

d2r=pi/180;
n=1;
for i = 1:length(fileList)
    split = regexp(fileList(i),'_','split');
    split = split{1,1};
    if isempty(regexp(split{1,length(split)},'im.dat','once')) == 0 ...
          && isempty(regexp(split{1,length(split)-1},'inv','once')) ...
        == 0 && isempty(regexp(split{1,2},'i','once')) == 0
        path = strcat(dirName,'/',fileList(i));
        path = path{1,1};
        freq_str = split{1,1}

        % load data
        img = importdata(path);
        bgd = importdata([dirName,'/',freq_str,'_b_inv_im.dat']);
        pes = importdata([dirName,'/',freq_str,'_i_inv_pes_ang.dat']);

        % normalize pBasexL images to go from 0 to 1
        img_ = (img - min(img(:))) / range(img(:));
        bgd_ = (bgd - min(bgd(:))) / range(bgd(:));

        figure(1)
        imshow(img_)
        colormap jet
        % save pBasexL image
        if ~exist([dirName,'_pBasexL Images'],'dir')
                mkdir([dirName,'_pBasexL Images']);
        end
        % multiplication with 255 necessary to get colormap right
```

```
50          imwrite(img_*255,jet,[dirName,'_pBasexL ...
                Images/',freq_str,'.png'],'png')
51
52  %%% Here r, r_max and r_min obtained with PES and FWHM!!
53          for i=1:length(pes)
54              if pes(i,1)~=0
55                  pes(i,2)=pes(i,2)/pes(i,1)^2;
56              end
57          end
58
59          % get radius of max of ring and sigma from gauss fit
60          [r, sig] = radiusCalc(pes)
61
62          % get radius r
63          FWHM = 2*sqrt(2*log(2)*sig)
64          % define r_min and r_max and hence also the width of summing ...
                sector
65          r_min = r - FWHM/2
66          r_max = r + FWHM/2
67
68  %%% summing of the circle sectors
69
70          % define out matrix, view image where sectors will be ...
                plotted on
71
72          zz=1;
73          color=['r','y'];
74          marker=['o','x'];
75          for k=1:2
76              out = zeros(360/stepsize,2);
77              if k == 1
78                  I = img;
79                  I_ = img_;
80                  z=1;
81              elseif k == 2
82                  I = bgd;
83                  I_ = bgd_;
84                  z=1;
85              end
86              % set up function for sector parts and mesh grid to be ...
                    able to apply function
87              [x, y] = meshgrid(1:size(I,1));
88              f =@(x0,y0,r_max,r_min,theta1,theta2) ...
89                  (x-x0).^2+(y-y0).^2<=r_max^2 & ...
90                  (x-x0).^2+(y-y0).^2>=r_min^2 & ...
91                  atan2(y-y0,x-x0)>=theta1 & ...
92                  atan2(y-y0,x-x0)<=theta2;
93              figure(3+k)
```

```
94              imshow(I_)
95              hold on
96              for l=-180:stepsize:179
97                  theta1 =  d2r * l;
98                  theta2 =  d2r * (l+stepsize);
99                  A = f(x0,y0,r_max,r_min,theta1,theta2);
100
101                 % define sector part
102                 [yy,xx]=find(A);
103
104                 % plot sector parts for to get a better picture ...
                        what's happening
105                 plot(xx,yy,'LineStyle','none','Color',...
106                     color(1,zz),'Marker',marker(1,zz))
107
108                 % sum up all values in sector part
109                 sumSec = sum(I(A));
110
111                 % save in out Matrix; angle defined as the center ...
                        angle of the
112                 % sector
113                 out(z,1) = l+stepsize/2;
114                 out(z,2) = sumSec;
115                 z=z+1;
116
117                 % zz used for alternating marker color and style
118                 if zz == 1
119                     zz=2;
120                 elseif zz == 2
121                     zz=1;
122                 end
123             end
124             hold off
125
126             % change angles of out from range [-180 180] to [0 360]
127             for m = 1:length(out(:,1))
128                 if out(m,1)>=-90 && out(m,1)<=180
129                     out(m,1) = out(m,1)+90;
130                 elseif out(m,1)>=-180 && out(m,1)<-90
131                     out(m,1) = out(m,1)+450;
132                 end
133             end
134             out = sortrows(out,1);
135             if k == 1
136                 img_out = out;
137             elseif k == 2
138                 bgd_out = out;
139             end
```

```
140         end
141         % substract background values from image values
142         comb_out = img_out;
143         comb_out(:,2) = img_out(:,2) - bgd_out(:,2);
144 
145         % plot and save plots of all together
146         figure(6)
147         plot(img_out(:,1),img_out(:,2),'LineStyle','none',...
148             'Marker','.','MarkerSize',13,'Color','k')
149         hold on
150         plot(bgd_out(:,1),bgd_out(:,2),'LineStyle','none',...
151             'Marker','.','MarkerSize',13,'Color','r')
152         plot(comb_out(:,1),comb_out(:,2),'LineStyle','none',...
153             'Marker','.','MarkerSize',13,'Color','b')
154 
155         if ~exist('SumVsTh_combined','dir')
156             mkdir('SumVsTh_combined');
157         end
158         h_fig = gcf;
159         print(h_fig,['SumVsTh_combined/',freq_str,'.eps'],'-depsc')
160         print(h_fig,['SumVsTh_combined/',freq_str,'.png'],'-dpng')
161         hold off
162 
163 
164 %%% fit and get beta vs. frquency
165         [ beta ] = BetaFit(comb_out(:,1), comb_out(:,2), split{1,1});
166         freq = str2double(freq_str);
167         betaVsFreq(n,1) = beta;
168         betaVsFreq(n,2) = freq
169         n=n+1;
170     end
171 end
172 betaVsFreq = sortrows(betaVsFreq,2);
173 
174 % plot and save betaVsFreq
175 plotBetaVsFreq(betaVsFreq(:,2), betaVsFreq(:,1))
176 dlmwrite([dirName,'betaVsFreq_withSubstr.m'],betaVsFreq)
177 end
178 
179 %% included functions: BetaFit, plotBetaVsFreq, radiusCalc
180 
181 function [ beta ] = BetaFit( xData, yData, Name )
182 
183 % (created 2015-01-23)
184 
185 % Set up fittype and options.
186 
187 % for 1-photon PD turn on this fit function
```

```
188 ft = fittype( '(1+b*((3*cos(x*pi/180)^2-1)/2))*a',...
189     'independent', 'x','dependent', 'y' );
190
191 opts = fitoptions( ft );
192 opts.Display = 'Off';
193 opts.Lower = [-Inf -Inf];
194 opts.StartPoint = [0.959492426392903 0.655740699156587];
195 opts.Upper = [Inf Inf];
196
197 % Fit model to data.
198 [fitresult] = fit( xData, yData, ft, opts );
199
200 % Plot fit with data.
201 figure(6);
202 h = plot( fitresult, xData, yData );
203 legend( h, 'sector sum vs. \theta', ...
204     '(1+\beta*((3*cos(\theta*pi/180)^2-1)/2))*a', 'Location', ...
          'NorthEast');
205
206 % Label axes & title
207 xlabel( '\theta' );
208 ylabel( 'sector sum' );
209 title('sector sum vs. \theta')
210
211 % properties
212 alw = 1;       % AxesLineWidth
213 lfsz = 16;     % x&y label fontsize
214 tfsz = 18;     % title fontsize
215 afsz = 13;     % axis fontsize
216 msz = 8;       % MarkerSize
217
218 % set properties
219 set(gca, 'FontSize', afsz, 'LineWidth', alw);
220 set(get(gca,'xlabel'),'FontSize', lfsz, 'FontWeight','normal');
221 set(get(gca,'ylabel'),'FontSize', lfsz, 'FontWeight','normal');
222 set(get(gca,'title'),'FontSize', tfsz, 'FontWeight','Bold');
223 get(gcf,'PaperSize');
224 set(gcf, 'PaperPositionMode', 'auto');
225 set(h, 'Markersize', msz)
226 axis([0 360 0 Inf])
227 h_fig = gcf;
228
229 % save
230 if ~exist('fit plots','dir')
231     mkdir('fit plots');
232 end
233 print(h_fig, ['fit plots/',Name,'_SumVsTh_fit.eps'], '-depsc')
234 print(h_fig, ['fit plots/',Name,'_SumVsTh_fit.png'], '-dpng')
```

```
235
236 % get beta
237 coeffs=coeffvalues(fitresult);
238 beta = coeffs(1,2);
239 end
240
241 function [] = plotBetaVsFreq( xData, yData)
242
243 %plot beta vs. freq det
244 figure(7)
245 h = plot(xData, yData);
246
247 % label axis and title
248 ylabel('\beta')
249 xlabel('frequency detuning')
250 title('\beta vs. recovery laser frequency detuning')
251
252 %properties
253 alw = 1;        % AxesLineWidth
254 lfsz = 16;      % x&y label fontsize
255 tfsz = 18;      % title fontsize
256 afsz = 13;      % axis fontsize
257 msz = 13;        % MarkerSize
258
259 % set properties
260 set(gca, 'FontSize', afsz, 'LineWidth', alw);
261 set(get(gca,'xlabel'),'FontSize', lfsz, 'FontWeight','normal');
262 set(get(gca,'ylabel'),'FontSize', lfsz, 'FontWeight','normal');
263 set(get(gca,'title'),'FontSize', tfsz, 'FontWeight','Bold');
264 set(h, 'Markersize', msz)
265 axis([-1 (max(xData(:))+1) -1 2])
266
267 set(gca,'XTick',0:20:max(xData(:)))
268 set(gca,'YTick',-1:0.5:2)
269 get(gcf,'PaperSize');
270
271 set(gcf, 'PaperPositionMode', 'auto');
272 end
273
274 function [r, sig] = radiusCalc(pes)
275
276 NvsR = pes;
277
278 numPeaks=input('How many peaks? (1 or 2)');
279
280 if numPeaks==1
281
282     figure(2)
```

```
283     plot(NvsR(:,1),NvsR(:,2));
284     % cut off noise in center
285     disp(...
286         'Starting radius?(Start to cut off bad points/noise in ...
                center?)');
287     startPoint=ginput(1)
288     startPoint = floor(startPoint);
289
290     figure(3)
291     plot(NvsR(startPoint:length(NvsR),1),NvsR(startPoint:length(NvsR),2));
292     disp('Best guess for peak location?')
293     peakX = ginput(1)
294
295
296     % fit and plot
297     f=fit(NvsR(startPoint:length(NvsR),1),...
298         NvsR(startPoint:length(NvsR),2),'a0+a1*exp(-((x-b1)/c1)^2)'...
299         , 'StartPoint', [0,0.001,peakX(1,1),10]);
300     plot(f,NvsR(startPoint:length(NvsR),1),...
301         NvsR(startPoint:length(NvsR),2));
302
303     % coeffs
304     CoeffValues=coeffvalues(f);
305     ConfIntValues=confint(f);
306
307     % getting radius and sigma
308     r = CoeffValues(1,3);
309     sig = CoeffValues(1,4);
310
311 else
312     figure(2)
313     plot(NvsR(:,1),NvsR(:,2));
314
315     % cut off noise in center
316     disp('Starting radius?(Start to cut off bad points/noise in ...
            center?)');
317     startPoint = ginput(1)
318     startPoint = floor(startPoint);
319
320     figure(3)
321     plot(NvsR(startPoint:length(NvsR),1),...
322         NvsR(startPoint:length(NvsR),2));
323     disp('Best guess for peak locations?')
324     [peakX, peakY] = ginput(2);
325     peakX
326
327     % fit and plot
328     f=fit(NvsR(startPoint:length(NvsR),1),NvsR...
```

```
329         (startPoint:length(NvsR),2),...
330         'a0+a1*exp(-((x-b1)/c1)^2)+a2*exp(-((x-b2)/c2)^2)'...
331         ,'StartPoint', [0,0.001,0.001,peakX(1,1),peakX(2,1),10,10]...
332         ,'Robust','LAR');
333     plot(f,NvsR(startPoint:length(NvsR),1),...
334         NvsR(startPoint:length(NvsR),2));
335
336     %coeffs
337     CoeffValues=coeffvalues(f)
338     ConfIntValues=confint(f)
339
340     r = CoeffValues(1,4);
341     sig = CoeffValues(1,6);
342
343     Error1 = (ConfIntValues(2,4)-ConfIntValues(1,4))/2
344
345 end
346 end
```

A.4 Analyze

```
1  function [] = AnalyzeF(dataFile, No)
2
3  %%%%%% Analyze final version (based on V4) %%%%%%%
4
5  %%%% dataFile:  directory where .dat-files of image (..._i_....dat) and
6  %%%%            background (..._b_....dat) of each frequency are located
7  %%%% No:        Name, usually date and frequency detuning (e.g.
8  %%%%            2015-02-10_90) how .txt and .png files will be saved
9  %%%%
10 %%%%
11 %%%% Analyze reads in the not normalized image with atoms of side ...
       imaging
12 %%%% (the input files usually have the ending _notNormalized.m), ...
       sums up
13 %%%% the pixel values of each line and plots them. The output files are
14 %%%% one .png with the plot and one .txt with the data for further
15 %%%% analysis in origin, having the line number in the first column
16 %%%% and the summed up pixel values in the second column
17
18 img_in = importdata(dataFile);
19
20 % rotate image if an angle is necessary for symmetry, insert angle ...
       as a
21 % number in "angle"
```

```
22 img_rot=img_in;
23 %img_rot = imrotate(img_in,angle);
24
25 % Sums up Bands of x
26 for n=1:length(img_rot(:,1))
27     sum = 0;
28     xLine = img_rot(n,:);
29     for m=1:length(xLine)
30         sum = sum + xLine(1,m);
31     end
32     outM(n,1) = n;
33     outM(n,2) = sum;
34 end
35
36  % Show bw Image
37 img_out=(img_rot-min(img_rot(:)))./range(img_rot(:));
38 close all
39 figure(1)
40 imshow(img_out);
41 hold on
42
43 %save sumVsx to .txt
44 dlmwrite([No,'_sumVSx.txt'],outM)
45
46 % plot sumVsx
47 figure(2)
48 plot(outM(:,1),outM(:,2))
49 title...
50  ('Vertical distribution of photodissociation fragments of J=0 ...
       molecules')
51 ylabel('y = r*cos(theta)')
52 xlabel('Horizontal signal sum (arb.)')
53 set(gca,'YDir','normal')
54 axis([-Inf Inf -Inf Inf])
55
56 % save plots of sumVSx
57 print(gcf, [No,'_sumVSx'], '-dpng');
58
59 end
```

Bibliography

[1] Lincoln D. Carr, David DeMille, Roman V. Krems, and Jun Ye. Cold and ultracold molecules: Science, technology and applications. *New Journal of Physics*, 11(5):055049, 2009.

[2] Reinhard Schinke. *Photodissociation Dynamics: Spectroscopy and Fragmentation of Small Polyatomic Molecules*. Cambridge Univeristy Press, Cambridge, 1993.

[3] Albert J. R. Heck and David W. Chandler. Imaging Techniques for the Study of Chemical Reaction Dynamics. *Annual Review of Physical Chemistry*, 46(1):335–372, 1995.

[4] Claire Vallance. 'Molecular photography': Velocity-map imaging of chemical events. *Philosophical Tranactions Royal Society A*, 362(1825):2591–2609, 2004.

[5] Michael N. R. Ashfold, Hendrik N. Nahler, Andrew J. Orr-Ewing, Olivier P. J. Vieuxmaire, Rachel L. Toomes, Theofanis N. Kitsopoulos, Ivan Anton Garcia, Dmitri A. Chestakov, Shiou-Min Wu, and David H. Parker. Imaging the dynamics of gas phase reactions. *Physical chemistry chemical physics*, 8:26–53, 2006.

[6] J. N. Louris, J. S. Brodbelt, and R. G. Cooks. Photodissociation in a quadrupole ion trap mass spectrometer using a fiber optic interface. *International Journal of Mass Spectrometry and Ion Processes*, 75(3):345–352, 1987.

[7] Richard N. Zare and Paul Dagdigian. Tunable Laser Fluorescence Method for Prduct State Analysis, 1974.

[8] S. C. Yang, A. Freedman, M. Kawasaki, and R. Bersohn. Energy distribution of the fragments produced by photodissociation of CS2 at 193 nm. *Journal of Chemical Physics*, 72(7):4058, 1980.

[9] James L. Stephenson, Matthew M. Booth, Joseph a. Shalosky, John R. Eyler, and Richard A. Yost. Infrared multiple photon dissociation in the quadrupole ion trap via a multipass optical arrangement. *Journal of the American Society for Mass Spectrometry*, 5(10):886–893, 1994.

[10] Simon Stellmer. *Degenerate quantum gases of strontium.* PhD thesis, University of Insbruck, 2013.

[11] Shinya Kato, Rekishu Yamazaki, Kosuke Shibata, Ryuta Yamamoto, Hirotaka Yamada, and Yoshiro Takahashi. Observation of long-lived van der waals olecules in an optical lattice. *Physical Review A*, 86:043411, Oct 2012.

[12] P. W. Atkins and R. W. Friedman. *Molecular Quantum Mechanics.* Oxford University Press, 2010.

[13] Simon Stellmer and Florian Schreck. Reservoir spectroscopy of 5s5p $^3P_2$–5snd $^3D_{1,2,3}$ transitions in strontium. *Physical Review A*, 90:1–14, 2014.

[14] Wojciech Skomorowski, Robert Moszynski, and Christiane P. Koch. Formation of deeply bound ultracold Sr_2 molecules by photoassociation near the $^1S+^3P_1$ intercombination line. *Physical Review A*, 85:1–10, 2012.

[15] J. M. Brown and A. Carrington. *Rotational Spectroscopy of Diatomic Molecules.* Cambridge Univeristy Press, 2003.

[16] Juris Ulmanis, Johannes Deiglmayr, Marc Repp, Roland Wester, and Matthias Weidemüller. Ultracold molecules formed by photoassociation: Heteronuclear dimers, inelastic collisions, and interactions with ultrashort laser pulses. *Chemical Reviews*, 112:4890–4927, 2012.

[17] D. Budker, D. F. Kimball, and D. P. DeMille. *Atomic physics: An exploration through problems and solutions.* Oxford University Press, 2008.

[18] Wojciech Skomorowski, Filip Pawlowski, Christiane P. Koch, and Robert Moszynski. Rovibrational dynamics of the strontium molecule in the $A^1\Sigma_u^+$, $c^3\Pi_u$, and $a^3\Sigma_u^+$ manifold from state-of-the-art *ab initio* calculations. *The Journal of Chemical Physics*, 136(2012):194306, 2012.

[19] T. Zelevinsky, M. M. Boyd, A. D. Ludlow, T. Ido, J. Ye, R. Ciurylo, P. Naidon, and P. S. Julienne. Narrow line photoassociation in an optical lattice. *Physical Review Letters*, 96:1–4, 2006.

[20] Mateusz Borkowski, Piotr Morzynski, Roman Ciury?o, Paul S Julienne, Mi Yan, Brian J DeSalvo, and T C Killian. Mass scaling and nonadiabatic effects in photoassociation spectroscopy of ultracold strontium atoms. *Physical Review A*, 032713(90):1–14, 2014.

[21] M. Auzinsh, D. Budker, and S. Rochester. *Optically Polarized Atoms: Understanding Light-atom Interactions.* OUP Oxford, 2010.

[22] B. H. Mcguyer, M. McDonald, G. Z. Iwata, W. Skomorowski, R. Moszynski, and

T. Zelevinsky. Control of optical transitions with magnetic fields in weakly bound molecules. *arXiv:1503.05946v1*, pages 1–8, 2015.

[23] Christopher Butler Osborn. *The Physics of Ultracold Sr_2 Molecules : Optical Production and Precision Measurement*. PhD thesis, Columbia University, 2013.

[24] G. Reinaudi, C. B. Osborn, K. Bega, and T. Zelevinsky. Dynamically configurable and optimizable zeeman slower using permanent magnets and servomotors. *JOSA B*, 29(4):729–733, 2012.

[25] Karen Liu and Michael G. Littman. Novel geometry for single-mode scanning of tunable lasers. *Opt. Lett.*, 6(3):117–118, Mar 1981.

[26] J. N. Walpole. Semiconductor amplifiers and lasers with tapered gain regions. *Optical and quantum electronics*, 28(6):623–645, 1996.

[27] Rodolphe Le Targat, J-J Zondy, and Pierre Lemonde. 75%-efficiency blue generation from an intracavity ppktp frequency doubler. *Optics Communications*, 247(4):471–481, 2005.

[28] A. Hemmerich, D. H. McIntyre, C Zimmermann, and T. W. Hänsch. Second-harmonic generation and optical stabilization of a diode laser in an external ring resonator. *Optics letters*, 15(7):372–374, 1990.

[29] Daryl W. Preston. Doppler-free saturated absorption: Laser spectroscopy. *American Journal of Physics*, 64(11):1432–1436, 1996.

[30] K. B. MacAdam, A. Steinbach, and C. Wieman. A narrow-band tunable diode laser system with grating feedback, and a saturated absorption spectrometer for Cs and Rb. *American Journal of Physics*, 60:1098–1098, 1992.

[31] C. Wieman and T. W. Hänsch. Doppler-free laser polarization spectroscopy. *Physical Review Letters*, 36(20):1170, 1976.

[32] The National Institute of Standards and Technology (NIST) database. http://www.nist.gov/pml/data, January 2015.

[33] R. W. P. Drever, John L. Hall, F. V. Kowalski, J. Hough, G. M. Ford, A. J. Munley, and H. Ward. Laser phase and frequency stabilization using an optical resonator. *Applied Physics B*, 31(2):97–105, 1983.

[34] Eric D. Black. An introduction to Pound–Drever–Hall laser frequency stabilization. *American Journal of Physics*, 69(1):79–87, 2001.

[35] Tetsuya Ido and Hidetoshi Katori. Recoil-free spectroscopy of neutral Sr atoms in the Lamb-Dicke regime. *Physical review letters*, 91(5):053001, 2003.

[36] Andrew D. Ludlow. *The Strontium Optical Lattice Clock: Optical Spectroscopy with Sub-Hertz Accuracy.* PhD thesis, University of Colorado at Boulder, 2008.

[37] G. Reinaudi, T. Lahaye, Z. Wang, and D. Guéry-Odelin. Strong saturation absorption imaging of dense clouds of ultracold atoms. *Optics letters*, 32(21):3143–3145, 2007.

[38] IDS Imaging Development Systems GmbH. Ids homepage, https://en.ids-imaging.com, Feb. 2015.

[39] Navitar, Inc. Navitar homepage, January 2015.

[40] B. H. Mcguyer, C. B. Osborn, M. McDonald, G. Reinaudi, W. Skomorowski, R. Moszynski, and T. Zelevinsky. Nonadiabatic effects in ultracold molecules via anomalous linear and quadratic zeeman shifts. *Physical Review Letters*, 111:1–5, 2013.

[41] B. H. McGuyer, M. McDonald, G. Z. Iwata, M. G. Tarallo, W. Skomorowski, R. Moszynski, and T. Zelevinsky. Precise study of asymptotic physics with subradiant ultracold molecules. *Nature Physics*, 11:32–36, 2015.

[42] B. H. McGuyer, M. McDonald, G. Z. Iwata, M. G. Tarallo, A. T. Grier, F. Apfelbeck, and T. Zelevinsky. High-precision spectroscopy of ultracold molecules in an optical lattice. *arXiv:1501.01236v1*, pages 1–12, 2015.

[43] John L. Bohn and P. S. Julienne. Semianalytic theory of laser-assisted resonant cold collisions. *Phys. Rev. A*, 60:414–425, Jul 1999.

[44] Kevin M. Jones, Eite Tiesinga, Paul D. Lett, and Paul S. Julienne. Ultracold photoassociation spectroscopy: Long-range molecules and atomic scattering. *Reviews of Modern Physics*, 78:483–535, 2006.

[45] G. Reinaudi, C. B. Osborn, M. McDonald, S. Kotochigova, and T. Zelevinsky. Optical production of stable ultracold $^{88}Sr_2$ molecules. *Physical Review Letters*, 109:1–5, 2012.

[46] Y. N. Martinez De Escobar, P. G. Mickelson, P. Pellegrini, S. B. Nagel, a. Traverso, M. Yan, R. Côté, and T. C. Killian. Two-photon photoassociative spectroscopy of ultracold ^{88}Sr. *Physical Review A*, 78(6):1–8, 2008.

[47] M. McDonald, B. H. McGuyer, G. Z. Iwata, and T. Zelevinsky. Thermometry via light shifts in optical lattices. *Physical Review Letters*, 114:023001, Jan 2015.

[48] Richard N. Zare. *Angular Momentum - Understanding Spacial Aspects in Chemistry and Physics.* Wiley-VCH Verlag GmbH & Co. KGaA, Weinheim, 1988.

[49] Richard N. Zare. Photoejection Dynamics 1. *Mol Photochem.*, 4(1):1–37, 1972.

[50] Richard N. Zare and Dudley R. Herschbach. Doppler line shape of atomic fluorescence excited by molecular photodissociation. *Proceedings of the IEEE*, 51:365–374, 1963.

[51] Eckart Wrede, Eloy R. Wouters, Marco Beckert, Richard N. Dixon, and Michael N R Ashfold. Quasiclassical and quantum mechanical modeling of the breakdown of the axial recoil approximation observed in the near threshold photolysis of IBr and Br_2. *Journal of Chemical Physics*, 116(2002):6064–6071, 2002.

[52] G. W. King and J. H. van Vleck. Dipole-dipole resonance forces. *Physical Review*, 55:1165–1172, Jun 1939.

[53] P. O'Keeffe, P. Bolognesi, R. Richter, A. Moise, E. Ovcharenko, L. Pravica, R. Sergo, L. Stebel, G. Cautero, and L. Avaldi. Photoelectron imaging in pump-probe experiments combining synchrotron and laser radiation. *Journal of Physics: Conference Series*, 235:012006, 2010.

[54] Goulven Quéméner and John L. Bohn. Strong dependence of ultracold chemical rates on electric dipole moments. *Physical Review A*, 81:1–9, 2010.

[55] B. H. McGuyer, M. McDonald, G. Z. Iwata, M. G. Tarallo, W. Skomorowski, R. Moszynski, and T. Zelevinsky. Precise study of asymptotic physics with subradiant ultracold molecules. *Nature Physics*, 11:32–36, 2014.

[56] James S. Cohen and Andrei Derevianko. Long-range forces between two excited mercury atoms and associative ionization. *Physical Review A*, 76:012706, Jul 2007.

[57] Sergei Manzhos, Constantin Romanescu, Hans Peter Loock, and Jonathan G. Underwood. Two-photon state selection and angular momentum polarization probed by velocity map imaging: Application to H atom photofragment angular distributions from the photodissociation of two-photon state selected HCl and HBr. *Journal of Chemical Physics*, 121(2004):11802–11809, 2004.

[58] T. Peter Rakitzis, P. C. Samartzis, R. L. Toomes, and Theofanis N. Kitsopoulos. Measurement of Br photofragment orientation and alignment from HBr photodissociation: Production of highly spin-polarized hydrogen atoms. *Journal of Chemical Physics*, 121:7222–7227, 2004.

[59] M. S. Child. Limits on the asymmetry parameters for two- and three-photon photofragmentation. *Physical Chemistry Chemical Physics*, 2(4):6169–6173, 2008.

[60] Richard N. Dixon. Recoil anisotropy following multiphoton dissociation via near-resonant intermediate states. *Journal of Chemical Physics*, 122(2005):0–13, 2005.

[61] S. Yang and W. T. III Hill. Proton angular distribution following multiphoton dissociative ionization of H_2. *Physical Review A*, 51(3):2301–2307, 1995.

[62] Seung E Choi and Richard B Bernstein. Theory of oriented symmetric-top molecule beams: Precession, degree of orientation, and photofragmentation of rotationally state-selected molecules. *The Journal of Chemical Physics*, 85(1):150–161, 1986.

[63] W. Koot, P. H P Post, W. J. van der Zande, and J. Los. Experimental wavefunctions for some selected excited states of H_2. *Zeitschrift fuer Physik D Atoms, Molecules and Clusters*, 10:233–245, 1988.

[64] L. Ph. Schmidt, T. Jahnke, a. Czasch, M. Schöffler, H. Schmidt-Böcking, and R. Dörner. Spatial Imaging of the H_2^+ Vibrational Wave Function at the Quantum Limit. *Physical Review Letters*, 108(7):2–5, 2012.

[65] Benjamin J Whitaker, David H Parker, and E Andr. *Velocity map imaging : Applications in molecular dynamics and experimental aspects*. Cambrdge Univeristy Press, 2003.

[66] M. N. R. Ashfold and D. H. Parker. Imaging molecular dynamics. *Physical chemistry chemical physics*, 16:381–2, 2014.

[67] Bernhard Dick. Inverting ion images without Abel inversion: Maximum entropy reconstruction of velocity maps. *Physical chemistry chemical physics*, 16:570–80, 2014.

[68] Gustavo A. Garcia, Laurent Nahon, and Ivan Powis. Two-dimensional charged particle image inversion using a polar basis function expansion. *Review of Scientific Instruments*, 75(2004):4989–4996, 2004.

[69] P. OKeeffe, P. Bolognesi, M. Coreno, a. Moise, R. Richter, G. Cautero, L. Stebel, R. Sergo, L. Pravica, Y. Ovcharenko, and L. Avaldi. A photoelectron velocity map imaging spectrometer for experiments combining synchrotron and laser radiations. *Review of Scientific Instruments*, 82, 2011.

[70] Ronald N Bracewell. *The Fourier transform and its application*. McGraw-Hill, 1978.

Acknowledgements

First of all, I would like to thank Prof. Dr. Theodor W. Hänsch for being my supervisor at Ludwig-Maximilians University Munich for this thesis and for his consent to evaluate it. I am very grateful to my supervisor at Columbia University, Prof. Dr. Tanya Zelevinsky for the opportunity to work in her research group and for giving me this exciting project. Special thanks goes to Mickey McDonald and Dr. Bart McGuyer. Without them, this thesis would not have been possible. Mickey has an incredible passion and excitement about the experiment, which made even the longest measurements being a good time. Bart's deep knowledge on the experimental and theoretical side, is very impressive and he was always willing to share it. I would like to thank Geoffrey Iwata and Dr. Marco Tarallo, for letting me work with you on the BaH-experiment at the beginning of my stay. Even if it turned out that my thesis covers another topic, I learned a lot from you and loved to work with you. Thanks to Dr. Andrew Grier for all the discussions we had and the help you provided. Thanks to Fabian Sörensen, Katérina Verteletsky, Damon Daw and Coleman Rainey for great discussions, the support and the laughs. Now, many many thanks again to the whole research group for all the fun and good times we had, weather while working in the lab, in discussions, at lunch breaks at Appletree or at any of the other various occasions. The atmosphere in Tanya's group is incredibly great, which is also to a big part thanks to her. For Mrs. Gschwendtner's support and her very helpful and fast replies, whenever I needed some help or had questions, I would like to say thank you.

A very special thanks goes to my parents. Throughout my life, they have always supported me and without their help, my stay in New York City would have not been possible. Also thanks to my sister for being there and for making my life brighter. Thanks to my grandmas, who are always there for us kids.

Erklärung:

Hiermit erkläre ich, die vorliegende Arbeit selbständig verfasst zu haben und keine anderen als die in der Arbeit angegebenen Quellen und Hilfsmittel benutzt zu haben.

Florian Apfelbeck

München, den 05. August 2015